Experimental and theoretical adsorption studies in tuneable organic-inorganic materials

Claudia Prosenjak

PhD

The University of Edinburgh
Institute for Materials and Processes

2009

Declaration

The work presented in this thesis was carried out in the School of Engineering at the University of Edinburgh. It is the original work of the author except where acknowledged in the text. This thesis was composed by the author and has not been submitted for any other degree or professional qualification.

Claudia Prosenjak

Abstract

Adsorption processes are widely used for the storage and separation of gases in many industrial and environmental applications. The performance of the process depends strongly on the adsorbent and its interaction with the gases. Therefore, the idea of tailoring the adsorbent to the application by adapting the pore size and/or the chemical composition is very attractive.

This work focuses on two groups of customizable hybrid materials: Firstly, in crystalline metal-organic frameworks (MOFs) the chemical and structural properties can be modified by changing the metal-oxide corner or the organic linker. Secondly, periodic mesoporous silica materials can be prepared with different pore sizes and geometries depending on the surfactant and its concentration and additionally modified with organic surface groups.

The adsorption behaviour of the materials can be predicted by molecular simulation and thus the influence of modifications can be studied without the need of synthesising the material. For MOFs, the coordinates of the atoms can be obtained from XRD measurements. The quality of the predicted adsorption results was investigated for pure gas (methane, ethane, propane, nitrogen and carbon dioxide) and gas mixture (methane – carbon dioxide) adsorption on the metal-organic framework CuBTC. The comparison showed a good agreement between experimental and simulated results especially at low pressures.

In order to create atomistic models for the mesoporous silica structures that are amorphous on the atomistic level, two existing simulation methods to model MCM-41-type materials were combined: micellar structures from coarse grained simulations that capture the phase separation in the surfactant/silica/solvent mixtures were used as input in kinetic Monte Carlo simulation that created the pore model on the atomistic level. The model created with this new methodology showed similar adsorption behaviour compared with a model created only with the kMC method using an ideal geometrical structure as micelle.

The influence of modifications of the MOF structures (exchange of metal, linker length/composition and catenation) was investigated by Grand Canonical Monte Carlo simulations for hydrogen adsorption at low temperature and temperature controlled desorption. The peaks in the desorption spectra could be related to steps in the adsorption isotherms at 20 K.

Acknowledgments

I am very grateful to Nigel Seaton and Tina Düren for their supervision, advice and guidance. Thank you for all the encouragement and support you gave me.

This thesis would not have been possible without the many collaborators, providing me with samples, analysis data and ideas. I would like to thank Bo Xiao from the University of St. Andrews and Franck Millange from the Institut Lavoisier, Université de Versailles-St-Quentin-en-Yvelines for providing and analysing samples of CuBTC; Sandine Bourelly and Philip Llewellyn from MADIREL, Université de Provence, CNRS Marseille for the measurement of the heat of adsorption; Karen Wilson from the University of York for the synthesis, modification and analysis of MCM-41 samples; Lyndsey Richie, Stuart Miller, Maria Castro and Paul Wright at the University of St. Andrews for helping me with XRD spectra, nitrogen isotherms, CHN analysis, introducing me to SEM measurements and very valuable discussions.

I am grateful to Alessandro Patti and Flor Siperstein for making the work on our joined project such a positive experience and to the Molecular Simulation group at the University Rovira i Virgili in Tarragona who made me feel very welcome during my stays there. I would like to thank Jiří Čejka who gave me the opportunity to visit his research group at the J. Heyrovský Institute of Physical Chemistry in Prague, Justyna Pawlesa and Arnošt Zukal who took the time to introduce me to XRD analysis and the experimental synthesis of mesoporous silica materials.

My thanks to the Adsorption group for the support I received and the friendships I found, to Christian Schumacher who introduced me to his simulation programs, Maria Victoria Navarro for getting me acquainted with the adsorption rig, and Carmelo Herdes for proof-reading my thesis.

I would like to thank everyone involved in the Marie Curie Research Training Network INDENS for the interesting project meetings, valuable discussions and insight in other research fields and I am grateful for the financial support provided through the Marie Curie Scholarship (MRTN-CT-2004-005503).

Last but not least I would like to thank my parents and my sister for all their support.

Table of Contents

1 Introduction

Gas adsorption is a widely used technology with many applications: separation and purification of gas mixtures (e.g. purification of feed streams, separation within process streams, and recovery of gases from exhaust streams) or gas storage (e.g. natural gas and hydrogen). The fields of applications are continuously extending due to the development of new materials and the investigation of materials for new applications. The porous material used in the adsorption process, the adsorbent, is of high importance for the process since its interactions with the fluid determine whether the required selectivity or capacity could be achieved. The selectivity and capacity of the whole process depend on further design and operation parameters that lie outside the scope of this thesis.

In the development of an adsorption process, computer simulations are used on very different scales: from simulations of a whole plant down to simulations at the molecular level. They offer *a priori* information about the process helping its optimization. Parameters in the simulations can often be changed more easily than in the "real world" and their individual effect on the whole process can be studied systematically. In this thesis, simulations at the molecular level are used to investigate gas adsorption studying in particular the interaction of the fluid molecules with the surface of the adsorbent.

In simulations, the adsorption of pure gases and gas mixtures can be studied under various conditions without the need for the sometimes expensive and time consuming experiments (especially for mixtures) and even hypothetical materials can be investigated that have not yet been synthesised. Furthermore, molecular simulations offer first and reliable access to information that require high experimental effort or can not be obtained experimentally at all, such as, for example, the location and energy levels of the adsorbed molecules or the contribution of a specific interaction (e.g. dispersive or electrostatic) to the overall adsorption.

In order for the simulations to have predictive power, the use of accurate molecular models, for the fluids, the materials and the resulting interactions, is essential. This means that the model of the adsorbent should capture the important characteristics of the real material. Two different families of materials are investigated in this thesis: metal-organic frameworks and mesoporous silica materials. Metal-organic frameworks are porous crystalline materials and the location of the framework atoms can experimentally be obtained, whereas for the

mesoporous silica materials, that are amorphous on the atomistic scale, the development of a model is one area of continuing research.

Therefore, one objective of this research is to apply both experimental and molecular simulation techniques to a specific metal-organic-framework material, combining both to provide molecular-level insights into the observed behaviour. For the mesoporous silica, as mentioned, the development of the model for the framework is not straightforward and a new method for obtaining atomistic models for these materials is developed.

For both families of materials investigated, simulations are a very valuable tool for analysing the adsorption properties. Metal-organic frameworks consist of metal corner units connected by organic linkers. Thousands of these materials have been reported and, even though only a few of them are stable upon solvent removal, and thus provide the porous network necessary for the adsorption (Rowsell and Yaghi (2004)), the opportunities for applications are very numerous. Simulations can help to screen these materials for given applications and by providing further insight, also might give guidelines for further research and predict advantageous materials, thus offering input for the synthesis of suitable materials. The mesoporous silica materials are non-crystalline but have a regular arrangement of pores with a narrow pore size distribution. The synthesis provides the opportunity to change many parameters. The materials can be synthesised with different geometries and in a wide range of pore diameters. Furthermore, the pore surface can be chemically modified by introducing for example organic groups (surface functionalization). Again, simulations can help to tune the adsorbent properties to match the desired application.

Another objective of this thesis is to investigate the effect of modifications of the metal-organic frameworks and the mesoporous materials. Changes in the metal and the linker as well as the interlinking of structures are influencing the adsorption properties of metal-organic frameworks and are studied in this thesis to understand the interactions between the frameworks and the fluids better. As an example, the adsorption and desorption of hydrogen was chosen. The interest in hydrogen storage is high since it provides the possibility to store and transport energy. Another gas for which the adsorption is of high interest is carbon dioxide. Removal of carbon dioxide from exhaust gases to reduce the emissions or from biogases for upgrading is environmentally and economically interesting. For the mesoporous silica materials, the effect of organic surface groups on the adsorption of carbon dioxide is therefore investigated.

1.1 Outline of the thesis

In Chapter 2, the two classes of materials investigated in this thesis, metal-organic frameworks and the mesoporous silica materials are introduced. The specific materials studied in this thesis are presented in detail.

In Chapter 3, the experimental methods used and the theoretical background for the simulations are presented. The pure gas (except for nitrogen at 77 K) and gas mixture isotherms were obtained with a high pressure volumetric adsorption rig; in this section the equipment is described and its operating procedure given. The molecular simulation method for the simulation of adsorption and its theoretical background is presented and the models for the molecular interactions are introduced. Furthermore, the characterisation methods used for the synthesised as well as the model materials are presented.

In Chapter 4, the adsorption results of pure gases and gas mixtures for the metal-organic framework, CuBTC, are presented, and experimental and simulated results are compared. The gases used in the single component adsorption were methane, ethane, propane, carbon dioxide and nitrogen. For all gases, experimental and simulated isotherms are presented. For the gas mixtures, experimental results for an equimolar carbon dioxide - methane mixture are given and compared to simulations. Additionally, the influence of the composition on the selectivity is studied by simulations for varying concentrations in the bulk phase for three different mixtures: carbon dioxide – methane, ethane – methane and ethane – carbon dioxide.

Chapter 5 focuses on the adsorption and desorption of hydrogen. The adsorption at 77 K on four different metal-organic frameworks: CuBTC, IRMOF-1, MIL-53-Al and IRMOF-8 is compared with experimental results by Panella *et al.* (2008). Experimental thermal desorption spectra presented in the same paper are compared with simulated desorption spectra. The desorption from further metal-organic frameworks is investigated by simulation to study the influence of changes in the framework on the desorption spectra. Furthermore, the desorption spectra are related to simulated adsorption isotherms at 20 K.

In Chapter 6, a new method of obtaining atomistic models for mesoporous silica materials is presented. The approach combines two existing methods that simulate the synthesis of mesoporous silica materials at different levels of detail. Moreover, the influence of organic surface groups on the adsorption of carbon dioxide is studied. The influence of halo-phenyl surface groups on the adsorption is investigated by simulations where the type and number

of halo atoms is varied. The simulated selectivity for the adsorption of an equimolar methane- carbon dioxide mixture comparing one halo- and two amino surface groups is given.

A summary of the work and the results obtained together with possible future developments concludes this thesis in Chapter 7.

1.2 Publication and presentations

"Modeling the synthesis of periodic mesoporos silicas", C. Prosenjak, A. Patti, F.R. Siperstein and N.A. Seaton, *Studies in Surface Science and Catalysis*, 2007, 170 B, 1652-1659.

The results have been presented at the following conferences and meetings:

C. Prosenjak, C. Schumacher, N.A. Seaton
"*Simulation of the synthesis and adsorption behaviour of MCM-41"*, poster presentation, CCP5 Annual Meeting 2005: Computational techniques and applications for materials modelling, 30 August- 2 September 2005, Keele, UK

C. Prosenjak, A. Patti, F. Siperstein and N.A. Seaton
"*Modelling the Synthesis of Mesoporous Silica"*, oral presentation
BZA Annual meeting, 30 July – 04 August 2006, Ambleside, UK

J. Pawlesa, A. Zukal, C. Prosenjak, N.A. Seaton and J. Čejka
"Adsorption Studies Using Micro and Mesoporous Materials", poster presentation
BZA Annual meeting, 30 July – 04 August 2006, Ambleside, UK

C. Schumacher, C. Prosenjak and N. A. Seaton
"Modelling of the synthesis of periodic mesoporous silicas by kinetic Monte Carlo simulation", oral presentation
CECAM Workshop Computational aspects of building blocks, nucleation, and synthesis of porous materials, 29 -31 August 2006, Lyon, France

C. Prosenjak and N. A. Seaton
"Design of functionalised MCM-41 for adsorption of CO_2", oral presentation
AIChE Annual Meeting, 12 -17 November 2006, San Francisco, USA

C. Prosenjak, A. Patti, F. R. Siperstein and N. A. Seaton
"Modeling the Synthesis of Periodic Mesoporous Silicas", oral presentation
AIChE Annual Meeting, 12 – 17 November 2006, San Francisco, USA

C. Prosenjak and N. A. Seaton
"Monte-Carlo-based design of a hybrid organic/inorganic adsorbent for the removal of CO_2", poster presentation
Fundamentals of Adsorption, 20 – 25 May 2007, Giardini Naxos, Italy

C. Prosenjak, A. Patti, F. R. Siperstein and N. A. Seaton
"Modeling the synthesis of periodic mesoporous silicas", oral presentation
International Zeolite Conference, 12 – 17 August 2007, Beijing, China

C. Prosenjak, P. Lozano-Casal, D. Fairen, G. Festa and T. Düren
"Molecular simulations: a valuable tool to support adsorption experiments in metal-organic frameworks (MOFs)", oral presentation
8th International Symposium on the Characterisation of Porous Solids, 10 – 13 June 2008, Edinburgh, UK

C. Ferreiro, C. Prosenjak, A. Patti, F. R. Siperstein, T. Düren, N. A. Seaton,
"Models of Surface roughness in pure and post-synthesis modified MCM-41 materials", poster presentation
8th International Symposium on the Characterisation of Porous Solids, 10 – 13 June 2008, Edinburgh, UK

C. Prosenjak, P. Lozano-Casal, T. Düren,
"Adsorption and beyond: using molecular simulation to understand adsorption in metal-organic frameworks", poster presentation
1st International Conference on Metal - Organic Frameworks and Open Framework Compounds, 8 – 10 October 2008, Augsburg, Germany

2 Materials

Porous materials provide the high surface area and strong solid-fluid interactions needed in adsorption applications. These materials are also important for many other applications, e.g. catalysis. The pore size plays an essential role in adsorption since it influences the force on the molecules exerted by the wall and also the accessibility of the pore. Porous materials are categorised according to their pore size following the International Union of Pure and Applied Chemistry (IUPAC):

- Microporous materials with a pore size below 2 nm
- Mesoporous materials with a pore size between 2 and 50 nm
- Macroporous materials with a pore size larger than 50 nm

Micropores are not much larger than the adsorbate molecules, which interact with the pore wall even in the centre of the pore. Some micropores can provide a steric hindrance if the molecules are larger than the pore size. The molecules are thus excluded from these pores and molecular sieving occurs. In mesopores, the interaction of the surface with the molecules is weaker but can still provide a high adsorption. In macropores the surface area does not have a big influence on the adsorption.

In this thesis, inorganic and hybrid organic-inorganic materials are considered. Inorganic materials have a good thermal stability and are widely used. Zeolites are the most important inorganic materials for adsorption and catalysis. Zeolites are composed of TO_4 tetrahedra, where the central 4-coordinated T atom represents silicon or aluminium. The zeolites are crystalline materials, providing known framework structures and narrow pore size distributions. These microporous materials are often used as molecular sieves. Around 200 zeolites have been identified and over 40 are occurring naturally. The tetrahedral units restrict the pore sizes that can be obtained by the rings that they form. In this thesis, another family of crystalline materials is investigated, the metal-organic frameworks. Metal-organic frameworks are composed of a wider range of atoms, containing an inorganic and an organic part and thus providing a wider range of surface chemistries and pore sizes.

Another commonly used inorganic adsorbent is silica gel which is a highly porous form of silica. It has a wide pore size distribution and the structure is fully disordered in contrast to the fully ordered crystalline materials. It is widely used as a desiccant. The mesoporous silica materials studied in this thesis are amorphous on the atomistic level as the silica gel but provide a regular arrangement of pores with a narrow pore size distribution.

The metal-organic frameworks as well as the mesoporous silica materials are very attractive for many applications due to the possibility of adapting properties of the material such as the pore size and/or the chemical composition to the application. Metal-organic frameworks can be tuned by changing the metal corner unit or the organic linker of the material. For mesoporous silica materials, the pore size and shape is influenced by the type and concentration of surfactant used as well as the synthesis temperature and time. Furthermore, the material can be modified with organic surface groups.

2.1 Metal-organic frameworks

Porous metal-organic frameworks (MOFs) combine organic and inorganic groups consisting of metal or metal oxide clusters linked by organic ligands as schematically shown in Figure 2-1. The wide choice of metals and ligands offers countless possibilities to design and functionalize the material.

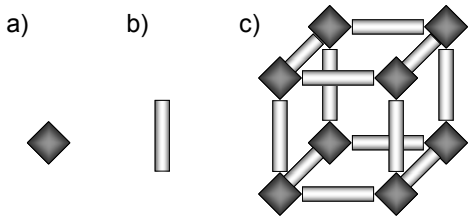

Figure 2-1 Schematic representation of a) the metal (-oxide) corner, b) the organic linker and c) a metal-organic framework.

In a MOF, the corner determines the connectivity and the linker the pore size and surface area. The crystallinity of the material provides an ordered structure with know properties. The large number of possible combinations leads to a high variation in pore sizes, surface areas, pore volumes and chemical properties. Rowsell and Yaghi (2004) reported in their review that more than 13,000 crystalline metal-containing compounds were catalogued in the Cambridge Structure database. Only a few of these are stable upon solvent removal, providing a porous structure. Other reviews, e.g. by Kitagawa *et al.* (2004), Rao and Gelb (2004), discuss the possibilities of combining inorganic and organic moieties in detail.

MOF materials are usually obtained by precipitation and crystallisation. At low temperatures, the crystal growth can be controlled by diffusion. For synthesis at temperatures above 100 °C solvothermal synthesis is used. The most commonly used solvent is water but other solvents are also widely used e.g. alcohol, dialkyl formamides and pyridine. The

synthesis is very sensitive to the conditions such as starting metallic salt, solvents and especially the temperature has a high impact and can lead to different structures. (Férey (2008))

Researchers are constantly looking for ways to improve the synthesis in order to have a fast and reliable way to produce a large amount of high quality MOFs and below are some new routes of synthesis that have been developed:

- A mixture of non-miscible solvents can be used for the hydrothermal synthesis where single crystals form at the interface. (Forster *et al.* (2002)).
- Electrochemical synthesis has been successfully used for the synthesis of CuBTC and other MOFs by researchers at BASF (Müller *et al.* (2006)).
- Microwave synthesis can reduce the crystallisation time considerably. (Kitagawa *et al.* (1995), Ni and Masel (2006), Bae *et al.* (2008)).

MOFs have drawn attention as materials for gas storage after Rosi *et al.* (2003) published hydrogen uptakes of up to 4.5 wt % at 77 K and 0.8 bar and 1.0 wt % at room temperature and 20 atm in MOF-5. These values are promising compared to other materials (see Chapter 5) even though the uptake is far from the goals set for 2010 by the U.S. Department of Energy (DOE) of 6.0 wt % and 45 kg H_2/m^3 at near ambient conditions (Department of Energy (2005)). The results at room temperature were confirmed by Pan *et al.* (2004) but contradicted by Panella and Hirscher (2005) who measured only an uptake of 0.2 wt % for up to 67 bar. The values at 77 K could not be reproduced: Rowsell *et al.* (2004) measured 1.32 wt % at 1 bar and Panella *et al.* (Panella and Hirscher (2005), Panella *et al.* (2006)) 1.6 wt % at 1 bar and 4.7 wt % at 50 bar.

The adsorption performance of MOFs depends on the synthesis and activation methods. The activation is a step that follows the synthesis where the template or the solvent is removed to obtain a solid with accessible pores. Hafizovic *et al.* (2007) investigated the strong differences in the surface area for MOF-5 as reported in the literature which varies between 700 and 3400 m^2/g. By following two reported synthesis strategies they found in the sample with the low surface area a phase containing $Zn(OH)_2$ clusters in the pores and a phase with interpenetration of the network. Furthermore, a change in the symmetry in the material from cubic to trigonal was observed. Guest molecules and interpenetration can also explain differences between experimental and simulated adsorption results on MOF materials. In simulations, as in Chapter 4 and 5, an ideal structure representing a single phase that is guest

free and usually non-interpenetrated (unless stated as in Chapter 5) is assumed. Figure 2-2 taken from Liu *et al.* (2007a) summarises experimental low pressure hydrogen adsorption results at 77 K on CuBTC available in the literature showing the strong influence of the synthesis and activation procedures on the adsorption performance. The synthesis and activation are important factors, but experimental hydrogen adsorption measurements are also very sensitive to impurities and leaks. Furthermore, for a material to become interesting for industrial applications, the performance has to be reproducible at a large scale.

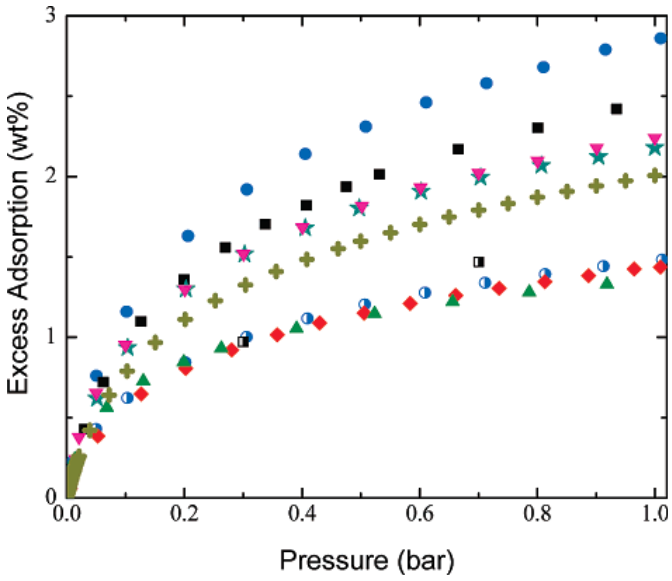

Figure 2-2 Comparison of experimental hydrogen adsorption isotherms for CuBTC at 77 K and low pressure, 0 < P < 1 bar. Different symbols represent data from different publications. Figure taken from Liu *et al.* (2007a). Reproduced by permission of the Royal Society of Chemistry.

The properties of MOFs such as high surface area and tuneable chemistry make them interesting materials not only for hydrogen storage but also for the storage of other gases such as methane (Düren *et al.* (2004)) or carbon dioxide (Babarao and Jiang (2008)), separation and purification applications (Müller *et al.* (2006)) as well as catalysis (Kitagawa *et al.* (2004)). The first MOF materials are industrially available under the trade name of BASOLITE® and Müller *et al.* (2006) review the applications from an industrial perspective. One limitation to the application of MOFs is their thermal stability as only very few materials are stable above 350-400 °C.

The crystalline structure of the MOF materials allows for a determination of the location of the framework atoms by experimental methods. The structural data for reported MOFs can

be obtained for example from the Cambridge Structural Database (CSD). The MOFs considered in this work are presented in more detail in the following sections.

2.1.1 CuBTC

In this thesis, the main focus for the MOF materials is on CuBTC (copper benzene-1,3,5-tricarboxylate) which is studied experimentally and by simulations. CuBTC was first reported by Chui *et al.* (1999) as HKUST-1. CuBTC has a Fm3m symmetry and pores of 1.02 nm and 1.2 nm and octahedral side pockets of 0.48 nm which are connected to the larger pores by windows of 0.35 nm (values calculated as described by Gelb and Gubbins (1999)). The accessible porosity is about 0.34 cm^3/g (Chui *et al.* (1999)). Figure 2-3 shows the unit cell of CuBTC.

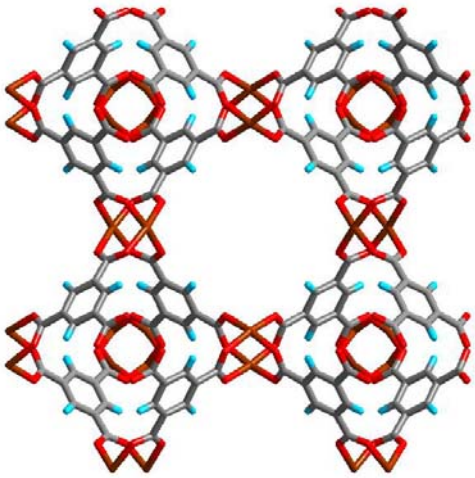

Figure 2-3 CuBTC framework, copper (brown), oxygen (red), carbon (grey) and hydrogen (light blue) atoms.

Experimental adsorption results published for CuBTC concentrate on hydrogen as described in Section 2.1. Argon adsorption at 87 K is an alternative to nitrogen adsorption at 77 K for characterisation and Vishnyakov *et al.* (2003), Krungleviciute *et al.* (2007) and Lee *et al.* (2005) used it for CuBTC. The first to report the adsorption of a range of gases were Wang *et al.* (2002) who measured the isotherms of N_2, CO_2, CO, CH_4, O_2, N_2O, C_2H_4, C_2H_6, *n*-$C_{12}H_{26}$ and H_2O up to 1 bar at 295 K (all on the same sample). Senkovska and Kaskel (2008) measured methane adsorption up to 200 bar at 303 K. Wang *et al.* (2002) measured carbon dioxide up to 20 bar at 298 K in addition to the low pressure data results. The high pressure data was measured on a different sample than the low pressure results in the same work. Millward and Yaghi (2005) also measured carbon dioxide at 298 K up to 42.5 bar, exceeding the amount adsorbed by Wang *et al.* (2002). Different syntheses and activation procedures

were followed leading to the discrepancies. Recently, Chowdhury *et al.* (2009) investigated the influence of different synthesis methods on the adsorption performance of CuBTC. Two CuBTC samples were synthesised, one based on the procedure described by Wang *et al.* (2002) giving a BET surface area of 857 m^2/g, and the other one using the synthesis method given by Liu *et al.* (2007a) resulting in a BET surface area of 1482 m^2/g. Measuring the adsorption of N_2, O_2, Ar, CO_2, C_3H_8 and SF_6 at 295.25 K and 318.15 K, a strong influence of the synthesis on the adsorption performance was found. The high surface area sample showed an increased uptake and a scaling factor was introduced to compare the capacities. The scaling factor changed with loading from around 2.04 at low loading to 2.58 at high loading.

The first simulation studies on this material were for argon adsorption (Vishnyakov *et al.* (2003)), argon diffusion (Skoulidas (2004)) and methane adsorption (Garberoglio *et al.* (2005)). Liu *et al.* (2007a) compared simulated hydrogen isotherms with their experimental data finding the amount adsorbed underpredicted in the simulations. The adsorption of mixtures on CuBTC has been simulated extensively and studies available in the literature are summarised in Table 2-1.

Table 2-1 Mixture adsorption studies on CuBTC (simulations).

Gas 1	Gas 2/ Gas 3	Reference
CO_2	N_2	Yang *et al.* (2007)
CO_2	O_2	Yang *et al.* (2007)
CO_2	O_2/N_2	Yang *et al.* (2007)
CO_2	CH_4	Yang and Zhong (2006a), Yang and Zhong (2006b)
CO_2	CH_4	Martín-Calvo *et al.* (2008)
CO_2	N_2	Martín-Calvo *et al.* (2008)
Simulated natural gas [a)]		Martín-Calvo *et al.* (2008)
CH_4	C_2H_6	Yang and Zhong (2006a)
CO_2	C_2H_6	Yang and Zhong (2006a)
H_2	CH_4	Yang and Zhong (2006b)
H_2	CO_2	Yang and Zhong (2006b)
H_2	CO_2/CH_4	Yang and Zhong (2006b)
H_2	CO	Karra and Walton (2008)
CO	CH_4	Karra and Walton (2008)
CO	N_2	Karra and Walton (2008)
CO_2	CO	Wang *et al.* (2008)
C_2H_4	CO_2	Wang *et al.* (2008)
C_2H_4	C_2H_6	Wang *et al.* (2008)
C_2H_4	C_2H_6	Nicholson and Bhatia (2007)

[a)] simulated natural gas with a composition of
$CH_4 : C_2H_6 : N_2 : CO_2 : C_3H_8 = 95 : 2.0 : 1.5 : 1.0 : 0.5$

2.1.2 IRMOFs

Isoreticular metal-organic frameworks (IRMOFs) were reported by Eddaoudi *et al.* (2002). The IRMOF series is based on MOF-5 (Li *et al.* (1999)), the most widely studied MOF in the literature, which is therefore also named IRMOF-1. The IRMOFs possess a cubic framework structure with Zn_4O clusters as corner units and differ in the linker. The series is an example of how modifications of MOFs with different organic linkers can be achieved in order to tune the pore size, pore volume, surface area and chemical properties.

As an example, the framework of IRMOF-1 is shown in Figure 2-4. The linker in this material is benzenedicarboxylate and it is oriented alternatively to the inside and to the outside of the network. The different orientations of the organic linker lead to the formation of two kinds of pores with distinct diameters, of 14.2 Å and 11 Å, respectively (theoretical values obtained from the largest spheres fitting inside without overlapping with the framework atoms as described by Gelb and Gubbins (1999)).

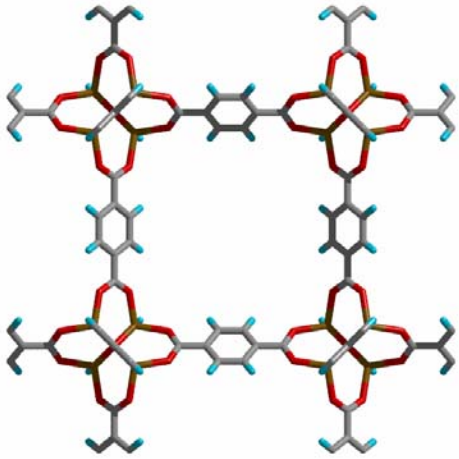

Figure 2-4 IRMOF-1 framework, zinc (brown), oxygen (red), carbon (grey) and hydrogen (light blue) atoms.

In this thesis, IRMOF-1, IRMOF-2, IRMOF-7, IRMOF-8, IRMOF-9, IRMOF-10, IRMOF-13 and IRMOF-14 were studied. The linkers for these materials are shown in Figure 2-5.

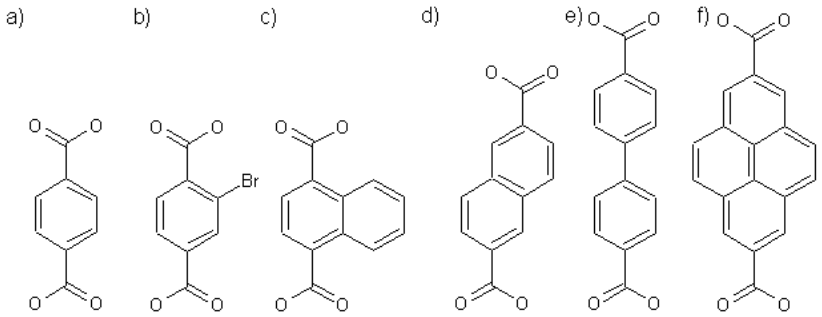

Figure 2-5 Linkers for the IRMOF materials. a) IRMOF-1, b) IRMOF-2, c) IRMOF-7, d) IRMOF-8, e) IRMOF-9, IRMOF-10 and f) IRMOF-13, IRMOF-14.

IRMOF-9 and IRMOF-13 are catenated versions of IRMOF-10 and IRMOF-14, respectively. Catenation, meaning the interlinking of the framework (schematically shown in Figure 2-6) is common for structures with large pores. Catenation reduces the pore size and therefore increases the interaction between the framework and the gas. Furthermore, it increases the density of the sample and reduces the free volume.

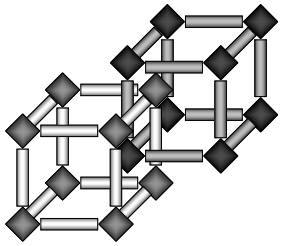

Figure 2-6 Schematic representation of a catenated framework. The structures are in different colours for better visibility.

2.1.3 MIL-53

MIL-53 (Barthelet *et al.* (2001), Serre *et al.* (2002), Loiseau *et al.* (2004)) is a nanoporous metal-benzenedicarboxylate $M(OH)(O_2C\text{-}C_6H_4\text{-}CO_2)$ containing trivalent chromium or aluminium (M). A breathing effect has been observed for certain guest molecules and Figure 2-7 shows the different forms of MIL-53 (Serre *et al.* (2002)). The as-synthesised structure in Figure 2-7 a) contains terephthalic molecules. These are removed upon heating and the framework expands and the one-dimensional channels with dimensions of 8.5 x 8.5 $Å^2$ become accessible (Figure 2-7 b). When cooling the structure again, water molecules are trapped inside the channels and due to their interaction with the framework induce a deformation of the framework leading to a decrease of the cell volume of *ca.* 40 % (Figure 2-7 c). The transition is fully reversible.

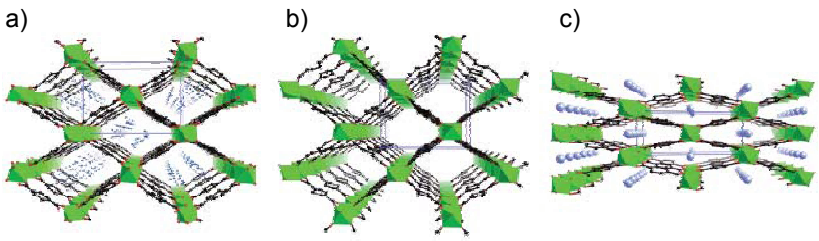

Figure 2-7 The different forms of MIL-53: a) as synthesised; disordered terephthalic acid molecules lie within the pore; b) high temperature; c) room temperature hydrated form. Reproduced with permission from Férey (2008). Copyright 2008 American Chemical Society.

The chromium and aluminium MIL-53 are isostructures. Changing the metal in a framework using the same linker has two effects: the main effect is the change in the crystal density of the sample due to different molecular weights. This has a large effect especially at high pressures and is important for hydrogen adsorption in reaching the gravimetric goals. A second effect is the changed interaction between the metal and the gas. This effect is especially pronounced at low loadings.

2.2 Mesoporous silica materials

The second group of materials investigated is mesoporous silica materials. They have a well defined pore structure with long-range order but are not crystalline on the atomic level as is the case for metal-organic frameworks. In the early 1990s, the family of MCM41S porous solids was presented by researchers of the Mobil Oil Corporation (Beck *et al.* (1992), Kresge *et al.* (1992)) that attracted a lot of interest due to their advantageous properties for adsorption, such as high porosity, high surface area and a narrow and controllable pore size distribution. The family of MCM41S consists of siliceous mesoporous materials with hexagonal (MCM-41), cubic (MCM-48) and lamellar (MCM-50) structures. Parallel to MCM41S, Yanagisawa *et al.* (1990) published the preparation of a mesoporous silica material from layered silicate. Many more mesoporous silica materials with different geometries and properties have been reported since. Reviews e.g. by Selvam *et al.* (2001) and Hoffmann *et al.* (2006) give a good overview over the different materials.

Mesoporous silica materials are produced by hydrothermal synthesis. In this process, a silica source (e.g. TEOS) is added to a surfactant solution. The surfactant molecules form micelles (e.g. spheres or rods) which act as template during the synthesis. The silica monomers polymerise around the surfactant micelles, creating a stable network. The template provides the long range order, the siliceous pore walls themselves are amorphous. In order to create the pores, the surfactant molecules have to be removed which can be done either through

calcination (temperatures of 500 to 600 °C) or solvent extraction (e.g. with hydrochloric acid). Different choices of inorganic precursors, surfactants (cationic, anionic, block-copolymers) and reaction conditions (pH, reaction time, temperature) have resulted in a wide range of materials. The synthesis takes up to several days but this time can be reduced to a few hours by using microwave synthesis (e.g. Wu and Bein (1996)).

The most studied mesoporous silica material is MCM-41 and also the work in this thesis is based on this material. The one-dimensional channels of MCM-41 are arranged in a hexagonal array (Figure 2-8). The pore size can be tuned in the range from 2 to 10 nm by choosing the length of the surfactant. The pore walls are 1 to 2 nm thick and the channels are not interconnected. A material that is similar to MCM-41 is SBA-15 (Zhao *et al.* (1998)) where the channels are also arranged in a hexagonal array. Amphiphilic block copolymers as structure directing agents are used in the synthesis of SBA-15 resulting in larger pore sizes of 5 to 30 nm and thicker pore walls (3 to 6.5 nm) than in MCM-41. Furthermore, connections between the channels exist in the case of SBA-15, whereas they do not in MCM-41.

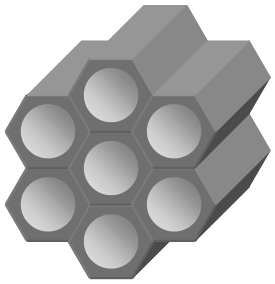

Figure 2-8 Pore arrangement of MCM-41.

SBA-15 belongs to the series of SBA-*n* (*S*anta *Ba*rbara) materials reported by Stucky and co-workers (Zhao *et al.* (1998)). Non-ionic surfactants have been used for the synthesis of mesoporous silica materials before. Pinnavaia and co-workers synthesised a series of mesoporous silica structures named MSU-*n* (*M*ichigan *S*tate *U*niversity, Bagshaw *et al.* (1995)) using neutral surfactants such as primary amines and poly(ethylene oxide)s. Attard *et al.* (1995) developed this method further obtaining hexagonal, cubic and laminar structures with narrow pore size distributions.

2.2.1 Simulations of mesoporous silica materials

Modelling the mesoporous silica materials and simulating their synthesis are very challenging tasks. As indicated above, the mesoporous silica materials provide a long-range

order but are amorphous on the atomistic scale. The number of atoms included in a representative section for modelling the synthesis and the long synthesis time of minutes (aggregation) to hours (calcination), requires simplifications of simulations based on the synthesis or only short stages of the synthesis can be simulated. Here, a short summary is given of how these challenges have been addressed by various researchers.

Depending on whether the interest is in the synthesis mechanism, the ordered phase at equilibrium or in an accurate representation of the pore structure, simulations on different scales are necessary to obtain results with resources and methodologies currently available. Jorge *et al.* (2009) showed that MD simulations are able to describe the early stages of the synthesis using an atomistic model. These simulations gave insights into the mechanism of the early stages of cationic surfactant self-assembly in the presence of anionic silica, showing that the silicates interact strongly with surfactant head groups and promote an increase in micelle size. The multiple charged silica oligomers were found to induce micellar aggregation. The shape transition from the initial spherical micelles to the cylindrical micelles that actually template the synthesis was not observed either because of the short timescale / small scale of the simulation or because of the short length of the surfactant.

In order to study the behaviour of the equilibrium phase, not yet in the reach of the MD approach, lattice Monte Carlo simulations (Siperstein and Gubbins (2003), Patti *et al.* (2007)) can be used. These simulations do not give information about the synthesis mechanism but about the equilibrium phase. The models used are coarse grained, i.e. the inorganic oxide is represented by one or two sites; and the surfactant is represented by a small number of sites. This reduces the complexity in order to make them computationally feasible. The model is able to describe the general behaviour of the system of interest, where the self-assembly of non-ionic surfactants in complex aggregates, the phase separation and the formation of ordered lyotropic liquid crystal phases are observed. An immiscibility gap in the ternary system and the formation of hexagonal (high silica/surfactant ratio) or laminar (low silica/surfactant ratio) structures in the phase with the high surfactant concentration was observed.

For the purpose of adsorption studies in mesoporous silica materials, e.g. in MCM-41, it is not necessarily important to understand the synthesis mechanism, nor which phase is formed, since it is already known that a hexagonal phase is investigated. The aim of the modelling process is to obtain a structure that exhibit similar properties than the experimental sample.

Models have been obtained in various ways: Yun *et al.* (2002) represented MCM-41 by single channels with regular pore walls. By adjusting three parameters (porosity, diameter and potential well depth) good agreement with experimental adsorption data was achieved. The predictive power of the model is limited at low pressures since the surface heterogeneity of the material, which is important for the adsorption in this pressure range, is not captured in these simple models. He and Seaton (2003) obtained a more heterogeneous pore surface by distributing silicon and oxygen atoms randomly around the pore volume. In the adsorption simulations, the dispersive interaction with the framework is limited to the oxygen atoms whereas the electrostatic interactions with silicon and oxygen atoms are accounted for. By fitting the pore size and the charge on the framework atoms to the isotherms at the lowest temperatures, good predictions at higher temperatures were achieved for this model. The agreement was better than for a model with a regular arrangement of the atoms that was used for comparison. Fox and Bates (2005) started their model for the adsorption of hydrocarbons from a perfect periodic crystal with a hexagonal pore shape. The model could be altered to a non-crystalline structure by randomly displacing the atomic positions of the silicon and oxygen atoms by up to 1 Å. This modification affected the adsorption at low pressure as expected.

Feuston and Higgins (1994) used MD simulations of annealing around a cylindrical micellar represented by Lennard-Jones atoms in a closed packed structure to obtain models for MCM-41. The effect of wall thickness and micelle size on the X-ray diffraction pattern was investigated and the best fitting model had walls thicker than 11 Å. Sonwane *et al.* (2005) based their model on this approach. They incorporated bulk heterogeneity by breaking 1-5 % of the randomly selected bulk Si-O bonds and introducing hydroxyl groups in its place. Surface roughness was added by removing atoms from randomly selected spherical areas with diameters of 4-6 Å. With this model good agreement with experimental XRD and WAXS results was obtained.

Coasne *et al.* (2006) carved pores out of a block of silica. Two different pore models were used in this approach: an ideal cylindrical structure and a structure obtained from the simulations of the ordered phase in equilibrium (Siperstein and Gubbins (2003)). The oxygen atoms at the resulting interface were saturated with hydrogen atoms and the surface was randomized and relaxed. The models were compared with experimental data using SANS spectra, adsorption isotherms and isosteric heat curves. The model based on the cylindrical pore model agrees well with the experimental data but did not show an appropriate surface

disorder at the mesoscale. By contrast, the model based on the equilibrium Monte Carlo simulations showed good agreement at the larger length scale but was too rough at the molecular scale.

Schumacher *et al.* (2006b) presented an approach based on a kinetic Monte Carlo method that follows the path of the experimental synthesis. This dynamic simulation models the individual chemical reactions and evolves stochastically in a way which represents, in a statistical sense, the development of the real silica matrix. The degree of polymerisation obtained was lower than in the experimental sample but the adsorption isotherms for nitrogen at 77 K and carbon dioxide and ethane at 263 K showed good agreement. In Chapter 6, a new approach is presented to obtain atomistic models for mesoporous silica materials, that extends this method to a wider range of mesoporous silica materials.

2.2.2 Modification of mesoporous silica materials

Mesoporous silica materials can be modified with functional groups. The material can be functionalised either in-situ or in a post-synthesis step (Hoffmann *et al.* (2006)). In the in-situ approach, the silica source containing the desired modification is used together with the pure silica source, where the ratio determines the degree of functionality. The modification of the silica source can influence the formation of the meso-phase and therefore adjustments of the synthesis procedure might be necessary to obtain the desired formation. The obtained structure is shown schematically in Figure 2-9 b). Some functional groups might be inside the wall and not on the pore surface as desired and are therefore not accessible. The removal of the surfactant has to be done by extraction since the high temperature normally used in calcination would destroy most functional groups.

Grafting the functional groups onto the pore wall of the pure silica material in a post-synthesis step is an alternative to the co-condensation approach to obtain a modified material. The synthesis gives the pure silica material with the template removed by calcination (Figure 2-9 a). Then this material is refluxed with a solution of the functionalised silica species R-Si$(EtO)_3$ that react with the silanol groups of the pore wall (Figure 2-9 c). Modifying the material in this way has the advantage that the synthesis is unchanged and calcination possible. But an even distribution of the functional groups is more difficult to obtain and clusters of surface groups can block access to the pores.

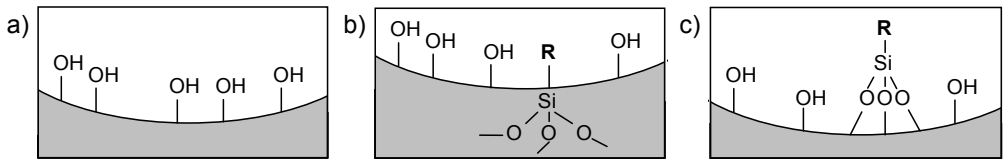

Figure 2-9 Pore surface of the a) unmodified, b) in-situ modified and c) post-synthesis modified material. The pore wall is represented in grey, the functional group as R.

In this thesis, modified mesoporous silicas for the adsorption of carbon dioxide are investigated. This has been studied experimentally by many authors before with a focus on structures modified with amino-surface groups such as monoamines (Huang *et al.* (2001), Hiyoshi *et al.* (2004), Kim *et al.* (2005), Knowles *et al.* (2005)), diamines (Hiyoshi *et al.* (2004), Zheng *et al.* (2005), Knöfel *et al.* (2007)) and triamines (Hiyoshi *et al.* (2004)). Harlick and Sayari (Harlick and Sayari (2006), Harlick and Sayari (2007)) investigated the adsorption of carbon dioxide on MCM-41 grafted with triamine. They found that the post-treatment and grafting conditions had a strong influence on the amount grafted and the carbon dioxide adsorption capacity. The best results were obtained with a pore-expanded MCM-41 material, where the grafting took place under wet conditions with 0.3 $cm^3/g(SiO_2)$ water at 85 °C. A carbon dioxide adsorption capacity of 2.65 mmol/g under dry conditions and 2.94 mmol/g under humid conditions was reached at 25 °C and 1.0 atm for a 5 % carbon dioxide in nitrogen mixture. Furthermore, the sample reached the highest adsorption rate with a maximum of 1.79 mmol/(g·min). The same grafting conditions were used by Serna-Guerrero *et al.* (2008) for aminopropyl modified pore-expanded MCM-41. The material had an even higher capacity for carbon dioxide of 3.67 mmol/g under humid conditions at 25 °C and a 5 % carbon dioxide in nitrogen fed at 1 atm.

Liang *et al.* (2008) and Hicks *et al.* (2008) used a different approach to include surface groups on SBA-15. Instead of grafting the whole surface group, the groups were "grown" on the surface, a method previously used by other researchers (Acosta *et al.* (2004), Reynhardt *et al.* (2004), Reynhardt *et al.* (2005)). Hicks *et al.* (2008) used aziridine which polymerised on the surface creating hyperbranched structures. The resulting material had a reported capacity for carbon dioxide of 3.1 mmol/g at 25 °C for a humid 10 % carbon dioxide in argon feed. Liang *et al.* (2008) modified SBA-15 with melamine based dendrimers. The carbon dioxide adsorption capacity for the functionalized materials increased compared to the unmodified material but not much compared to SBA-15 modified with aminopropyl-surface groups. This is explained by a small change in the number of the most reactive primary amines.

Whereas in all of the previously presented studies the surface groups were covalently bond to the pore surface, Xu *et al.* (Xu *et al.* (2002), Xu *et al.* (2003)) reported a "molecular basket" where polyethyleneimine (PEI) is brought into the pores of MCM-41 though not grafted onto the surface. They found that the adsorption capacity is increased if the temperature is raised from 50 °C to 75 °C e.g. from 44 mg/g to 112 mg/g for a PEI loading of 50 %, making it an interesting material for adsorption at higher temperatures. The higher adsorption capacity was explained by a kinetically controlled adsorption and that not all adsorption sites could be reached at 25 °C after 150 min. The adsorption for the pure MCM-41 is much lower and dropped from 14.3 mg/g at 50 °C to 8.6 mg/g at 75 °C. Xu *et al.* (2005) found that moisture has a positive effect on the adsorption of carbon dioxide with PEI-MCM-41 from a flue gas stream. Hicks *et al.* (2008) studied SBA-15 impregnated with PEI, confirming that the capacity of the material increases with an increase in temperature from 25 °C to 75 °C with an equilibration time of 200 min.

Schumacher *et al.* (Schumacher and Seaton (2005), Schumacher *et al.* (2006a)) were the first to study the adsorption on MCM-41 modified with organic surface groups by simulations. The comparison between their experimental and simulated adsorption results showed good agreement for phenyl and aminopropyl modified MCM-41. They used their developed method to predict the adsorption of pure gases and a flue gas mixture on MCM-41 modified with 20% aminomethyl, 10% aminopropyl and 10% diaminophenyl, finding that diaminophenyl-MCM-41 gives the best selectivity for carbon dioxide from a flue gas mixture with a composition of CO_2:N_2:O_2 = 14:81:5 at 20 °C.

The possibility of changing the chemical properties of the mesoporous silica materials is an important advantage and opens the door for many applications. The material can be modified with surface groups, by depositing functional groups in the pore space or by ion exchange, making them catalytically active. Together with the control over pore size and shape, the material can be tailored to the application in many fields e.g. adsorption, separation, catalysis, nanowire fabrication, sensors or controlled drug release.

3 Adsorption experiments and simulations

In this thesis, the adsorption phenomenon is investigated by experiments and simulations. Adsorption isotherms of single gases and gas mixtures were measured and obtained by simulations. This chapter introduces the experimental setup and explains the procedures for obtaining the isotherms as well as the methods used in the simulations.

3.1 Adsorption experiments

The high-pressure adsorption isotherms were measured using a volumetric adsorption apparatus with the piping and instrumentation diagram given in Figure 3.1. In order to have an accurate pressure reading at low and high pressures, the apparatus is fitted with two Baratron absolute pressure transducers (MKS type 127A) with a two-channel readout/signal conditioner (MKS type PR4000). The reading accuracy is 0.05 % of the usable measurement range (0-1.33 bar and 0-33 bar).

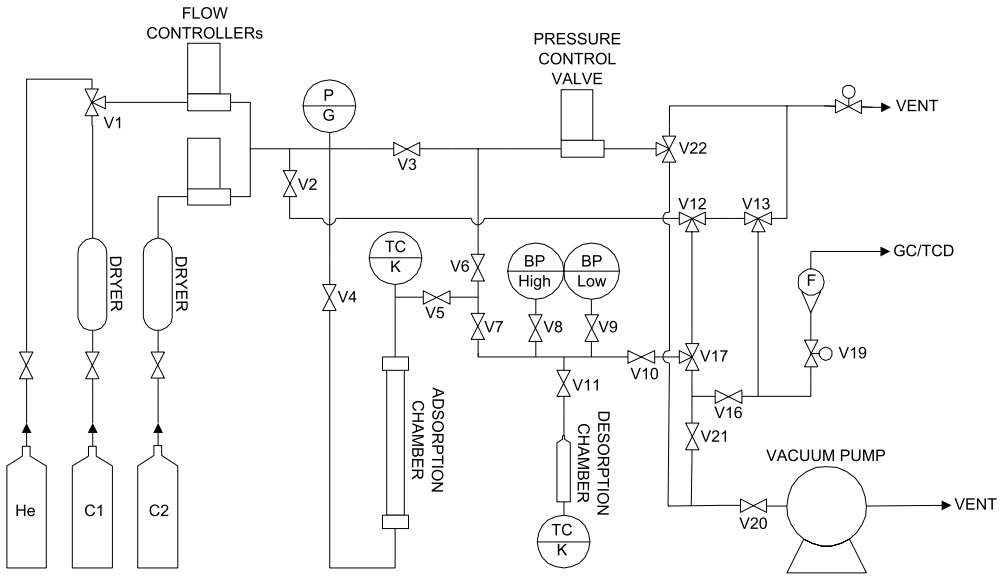

Figure 3.1 Piping and instrumentation of the volumetric adsorption rig.

The adsorption equilibrium isotherms for carbon dioxide, methane, ethane, propane and nitrogen on the metal-organic framework CuBTC were measured at 298 K and up to 25 bar. Furthermore, an isotherm for the equimolar mixture of methane and carbon dioxide was measured on the same sample at 263 K. The amount of sample used was 1.66 g. For the mesoporous silica materials, carbon dioxide isotherms were measured on MCM-41 and pentafluorophenyl-MCM-41 (PFP-MCM-41) at 298 K. The amounts of sample used were

1.65 g and 1.68 g respectively. The adsorptive gases were supplied by BOC with a purity of 99.99 %.

Here, a brief description of the different steps of the volumetric adsorption experiments for single gases and mixtures is given. The sub-procedures for the sample preparation, calibration of the dead volume, and measurement of the adsorption are explained. Further details of the rig and the operating procedure can be found in the paper by Yun *et al.* (2002).

Sample preparation

In a first step, the sample is pelletised to avoid the contamination of the rig with the sample. Then the sample is activated and introduced into the rig as follows: The adsorption chamber is disconnected and cleaned. Then the caps at the top and bottom of the adsorption chamber are filled with inert glass pearls and glass wool to reduce the dead volume. The CuBTC sample is activated in vacuum (Heraeus Vacutherm vacuum oven, nominal vacuum $1 \cdot 10^{-2}$ mbar) for 6 hours at 180 °C. The MCM-41 and PFP-MCM-41 samples are dried in air: MCM-41 for 4 hours at 220 °C and PFP-MCM-41 for 6 hours at 110 °C. The sample is quickly weighted and rapidly transferred to the adsorption chamber which is fitted to the rig. The rig was tested for leaks at high pressures and vacuum. For the high pressure test, helium was introduced into the rig. First, quick checks at 2 bar, 5 bar and 10 bar are used to detect larger leaks. Then, if after equilibration at a pressure of 20 bar there was no noticeable pressure drop (< 1 Pa) for a period of time higher than the time for a single gas pressure point and nor a detectable increase in pressure (< 0.1 Pa) at vacuum conditions, the leak rate was considered to be small enough not to influence the results.

Once the set-up is leak-free, the sample is degassed. The adsorption chamber is heated in a removable oven with radiation heating elements to the degassing temperature (130 ºC for CuBTC, 150 °C for MCM-41, 110 °C for PFP-MCM-41) and the gas is removed by a vacuum pump. The degassing temperature is kept constant for 3 hours while the pressure in the adsorption chamber is as low as 10 Pa. After degassing, the oven is removed and the adsorption chamber isolated. A cooling/heating bath set at the temperature at which the adsorption isotherm will be measured is used to equilibrate the temperature in the adsorption chamber.

Determination of the dead volume by helium calibration

When the temperature is equilibrated, the dead volume of the adsorption chamber V_{dead} is obtained by helium calibration (Talu and Myers (2001)). This volume is needed for the calculation of the amount adsorbed in a volumetric adsorption experiment. The helium calibration is done as follows: The reservoir, consisting of the desorption chamber and the piping between V5 and V10 in Figure 3.1 and with the known volume V_{res}, is evacuated in addition to the adsorption chamber. This reservoir is then filled with helium at a pressure between 0.2 and 0.4 bar. Once the reservoir is thermally equilibrated, the temperature and pressure are recorded. With the temperature, pressure and volume known and assuming ideal gas, the amount of helium in the reservoir is calculated as

$$N_1 = \frac{PV_{res}}{RT} \tag{3.1}$$

where R is the universal gas constant. The helium is expanded into the adsorption chamber by opening valve V5. When the thermal equilibrium is obtained again, the pressure and temperature are read and the amount of helium in the reservoir after the expansion, N_2, is calculated using equation (3.1). The difference N_2-N_1 is the amount of helium in the adsorption chamber. Therefore, with the temperature and pressure known, V_{dead} can be calculated as

$$V_{dead} = (N_1 - N_2)\frac{RT}{P} \tag{3.2}$$

The value for V_{dead} used in further calculations is the average of five measurements.

Adsorption measurements for pure component experiments

The volumetric measurement of adsorption is also based on the expansion of the gas in the reservoir. Due to the non-ideal behaviour of some gases, the Peng-Robinson equation of state (PR-EOS, Appendix D) is applied. As for the helium calibration, the adsorption measurement starts with the evacuated adsorption chamber and reservoir after degassing. After the evacuation, the reservoir is disconnected from the adsorption chamber and filled with the adsorptive. The pressure in the reservoir should be higher than the pressure point to measure since the pressure will drop due to expansion and adsorption. When the reservoir is equilibrated with the ambient air, the temperature is read and the amount of gas in the reservoir calculated using the PR-EOS. Then the gas in the reservoir is expanded into the adsorption chamber. After thermal equilibration, the pressure and temperature in the system are read and the amount of gas in the reservoir is calculated again using the PR-EOS. Since the dead volume, V_{dead}, is known from the helium calibration, the amount of not-adsorbed gas in the adsorption chamber can be also calculated using the PR-EOS. Then, with the

amounts in the reservoir and in the dead volume known, the amount adsorbed, which is in equilibrium with the gas phase defined by the temperature and pressure in the system, can be obtained. For the calculations of the second and higher points the amount in the adsorption chamber from the point before has to be taken into account. The procedure is repeated for each point of the isotherm.

Adsorption measurements for gas mixture experiments

The approach used for the pure component measurements does not work for the adsorption of mixtures since the composition of the gas phase is changing during equilibration. Therefore, for the adsorbed phase to be in equilibrium with a gas phase of constant composition, a continuous feed of the set composition is used. This is achieved by controlling the flow rates of the pure gases before they are mixed and come into contact with the sample. The flow control valves are calibrated for the components used and a continuous flow of the desired composition is set. The sample has to be degassed and the adsorption chamber evacuated before each pressure point. The sample is equilibrated for 4 hours with the flow of constant composition, pressure and temperature. After this equilibration, the adsorption chamber is isolated, the gas flow stopped and the reservoir is evacuated again. The gas is transferred from the adsorption chamber to the desorption tank by heating the adsorption chamber and cooling the desorption chamber with liquid nitrogen. A pressure gradient is created between the adsorption chamber and the desorption chamber by the gas condensing due to the low temperature. The result is that almost all adsorbed fluid desorbs and condenses in the desorption chamber. The evacuated adsorption chamber is isolated from the desorption chamber where the temperature is increased to ambient temperature. This leads to an evaporation of the condensate whose composition is a mixture of the set composition in the gas phase of the adsorption chamber and the composition of the adsorbed phase. The total amount that was adsorbed can be calculated as above from the pressure and temperature in the reservoir. The gas mixture in the reservoir is analysed by gas chromatography. The composition for the adsorbed phase in equilibrium with the flow set up in the experiment is obtained. The same procedure is followed for each point of the isotherm.

3.2 Molecular simulation of adsorption

In this section the relevant statistical mechanics concepts related to the description of adsorption phenomena are presented. More detailed descriptions of statistical mechanics and the grand canonical Monte Carlo method can be found in numerous references e.g. Hill (1960), Allen and Tildesley (1989), Frenkel and Smit (2002).

3.2.1 Statistical mechanics

Statistical mechanics and the computer simulations based upon it provide the link between the properties of the individual molecules observed in the simulation and the thermodynamic properties of the system on the macroscopic level observed in the experiment.

At the microscopic level, the positions and momenta of all molecules define a microstate. A large number of systems, each representing a possible microstate of the real system with the same macroscopic constrains is called an ensemble. On the macroscopic level, only a small number of independent parameters (e.g. volume, temperature and pressure) equal to the degrees of freedom are necessary for a complete description. The ensembles are defined by the macroscopic properties that are held constant. Some important ensembles are:

- microcanonical ensemble or NVE ensemble with constant number of molecules, volume and energy
- canonical ensemble or NVT ensemble with constant number of molecules, volume and temperature
- isobaric/isothermal ensemble or NPT ensemble with constant number of molecules, pressure and temperature
- grand canonical ensemble or μVT ensemble with constant chemical potential, volume, and temperature

In experiments, the average is taken over time and fluctuations of the microscopic properties are usually not observed. In simulations, the molecular dynamics approach also averages over time. By contrast, Monte Carlo simulations average over a large number of microstates that correspond to the same macroscopic system obtaining the ensemble average. The ergodic hypothesis states that the time average equals the ensemble average, i.e. that all accessible microstates are equally probable over a long period of time. A macroscopic property M can therefore be calculated by summing up the corresponding property M_k in all possible microstates weighted with the probability of observing the microstate in the ensemble P_k:

$$M_{observed} = \langle M \rangle_{ensemble} = \sum_k M_k P_k \tag{3.3}$$

where $\langle ... \rangle_{ensemble}$ denotes the ensemble average. The ensemble used for adsorption studies is the grand canonical ensemble where the number of molecules is not fixed. The following deductions are therefore done for this ensemble.

The probability of an arbitrary microstate k with N particles and the Energy E_k, which is the quantum mechanical description of the system having discrete energy level E_k, is (Hill (1960)):

$$P_{k,N} = \frac{1}{\Xi}\exp(-\beta E_k)\exp(\beta\mu N) \tag{3.4}$$

with $\beta = 1/(k_B T)$, where k_B is the Boltzmann constant. Ξ is the partition function for the μVT ensemble, defined as the sum over all possible microstates

$$\Xi = \sum_{k,N}\exp(-\beta E_k)\exp(\beta\mu N) \tag{3.5}$$

Substituting (3.4) into equation (3.3) gives:

$$\langle M\rangle_{\mu VT} = \frac{1}{\Xi}\sum_{k,N} M_k \exp(-\beta E_k)\exp(\beta\mu N) \tag{3.6}$$

In order to be able to solve the equation in a relevant case study, a change from quantum behaviour to classical behaviour is required, where a point in phase space corresponds to a microstate. The configuration space is the subspace of the phase space containing the positions and orientations of the molecules. Therefore, the sum over all microstates in equation (3.6) is replaced by the sum over all microstates for classical statistical mechanics. The total energy can be divided into a kinetic part depending on the momenta and a potential part depending on the positions of the molecules. The kinetic contribution of a monoatomic particle is $V/(\Lambda^3)$. V is the volume and the thermal de Broglie wavelength Λ is defined as

$$\Lambda = h\sqrt{\frac{\beta}{2\pi m}} \tag{3.7}$$

where h is Planck's constant and m the mass of the molecule. The potential energy depends on intermolecular interactions and the models for it are described in Section 3.2.3. The classical description of equation (3.6) becomes

$$\langle M\rangle_{\mu VT} = \frac{1}{\Xi}\sum_{N}\frac{1}{N!}\frac{V^N}{\Lambda^{3N}}\int M(\mathbf{s})\exp(-\beta U(\mathbf{s}))\cdot\exp(\beta\mu N)d\mathbf{s} \tag{3.8}$$

where **s** are the configurations. The corresponding probability distribution ρ for a state with N particles is given in equation (3.9) for a single component system and in (3.10) for a multi-component system, where index i refers to the species i.

$$\rho(\mathbf{s}) = \frac{1}{\Xi}\frac{1}{N!}\frac{V^N}{\Lambda^{3N}}\exp(-\beta U(\mathbf{s}))\exp(\beta\mu N) \tag{3.9}$$

$$\rho(\mathbf{s}) = \frac{1}{\Xi}\prod_i\left(\frac{1}{N_i!}\frac{V^{N_i}}{\Lambda^{3N_i}}\exp(\beta\mu_i N_i)\right)\exp(-\beta U(\mathbf{s})) \tag{3.10}$$

Solving equations (3.8), (3.9) and (3.10), techniques such as the Monte Carlo integration scheme becomes useful, since conventionally numerical integration techniques are only feasible for very small systems.

In the Monte Carlo method, the integral is solved by calculating it at randomly chosen points. The simplest case, namely using sampling points that are evenly spread over the integration space and contribute unweighted to the value of the integral, has the disadvantage that a major part of the computing time might be spent on evaluating the expression at points where it has a negligible value. This is the case for evaluating equations (3.9) and (3.10), where the Boltzman factor $\exp(-\beta U)$ has a large number of points in phase space that do not contribute to the integral. Therefore, to improve this approach, preference should be given to sampling points where the integrated function has a significant value, referred to as importance sampling. This can be achieved by selecting the sampling points using a probability distribution. Due to the resulting uneven distribution of evaluated points, the obtained values have to be weighted accordingly to calculate the value of the integral.

Metropolis *et al.* (1953) proposed a widely used importance sampling scheme which enables the sampling of the configuration space of all configurations s in accordance to the probability density $\rho(s)$ of finding the real system in a microstate with configuration s, without knowing the density distribution $\rho(s)$ explicitly. The system has to be ergodic, meaning that every point in the configuration space can be reached within a finite number of trials.

The phase space is sampled by a random walk, generating a Markov chain of configurations. Markov chains have no memory and the probability for a move from an old configuration (**o**) to a new configuration (**n**) depends only on these microstates, not on any previous configurations. The move is accepted or rejected according to the ratio of probabilities of these configurations. For the probabilities of a trial $P(\mathbf{o}\rightarrow\mathbf{n})$ and the reverse trial $P(\mathbf{n}\rightarrow\mathbf{o})$, the detailed balance condition has to be satisfied:

$$\frac{P(\mathbf{o}\rightarrow\mathbf{n})}{P(\mathbf{n}\rightarrow\mathbf{o})} \equiv \frac{\rho(\mathbf{n})}{\rho(\mathbf{o})} \tag{3.11}$$

The overall probability of a trial $P(\mathbf{o}\rightarrow\mathbf{n})$ is composed of the a priori probability $P_{gen}(\mathbf{o}\rightarrow\mathbf{n})$ and the acceptance probability $P_{acc}(\mathbf{o}\rightarrow\mathbf{n})$. The a priori probability is the probability of attempting the trial $\mathbf{o}\rightarrow\mathbf{n}$ when the system is in the state o and the latter is the probability of accepting this generated trial and (3.11) becomes

$$\frac{\rho(\mathbf{n})}{\rho(\mathbf{o})} \equiv \frac{P(\mathbf{o}\to\mathbf{n})}{P(\mathbf{n}\to\mathbf{o})} = \frac{P_{gen}(\mathbf{o}\to\mathbf{n})\cdot P_{acc}(\mathbf{o}\to\mathbf{n})}{P_{gen}(\mathbf{n}\to\mathbf{o})\cdot P_{acc}(\mathbf{n}\to\mathbf{o})} \tag{3.12}$$

The a priori transition probability has a positive value less or equal 1. The acceptance probability $P_{acc}(\mathbf{o}\to\mathbf{n})$ can range between 0 and 1, inclusive. Metropolis *et al.* chose the same constant a priori probability for the trial $\mathbf{o}\to\mathbf{n}$ as for the reverse trial $\mathbf{n}\to\mathbf{o}$ so that $P_{gen}(\mathbf{o}\to\mathbf{n})$ and $P_{gen}(\mathbf{n}\to\mathbf{o})$ cancel out in equation (3.12). Furthermore, the greater of the acceptance probabilities $P_{acc}(\mathbf{o}\to\mathbf{n})$ and $P_{acc}(\mathbf{n}\to\mathbf{o})$ was set to 1 and the other one according to equation (3.12) giving the acceptance probabilities of the Metropolis scheme:

$$P_{acc}(\mathbf{o}\to\mathbf{n}) = \min\left(1, \frac{\rho(\mathbf{n})}{\rho(\mathbf{o})}\frac{P_{gen}(\mathbf{n}\to\mathbf{o})\cdot P_{acc}(\mathbf{n}\to\mathbf{o})}{P_{gen}(\mathbf{o}\to\mathbf{n})}\right) \tag{3.13}$$

$$P_{acc}(\mathbf{n}\to\mathbf{o}) = \min\left(1, \frac{\rho(\mathbf{o})}{\rho(\mathbf{n})}\frac{P_{gen}(\mathbf{o}\to\mathbf{n})\cdot P_{acc}(\mathbf{o}\to\mathbf{n})}{P_{gen}(\mathbf{n}\to\mathbf{o})}\right) \tag{3.14}$$

Biased sampling techniques can help to speed up the simulation by favouring trials with a high acceptance probability. For this, certain a priori probabilities $P_{gen}(\mathbf{o}\to\mathbf{n})$ are modified. Since the detailed balance condition has to be satisfied, the acceptance probabilities are used to even out the imbalance caused, e.g. when $P_{gen}(\mathbf{o}\to\mathbf{n})$ is reduced, $P_{acc}(\mathbf{o}\to\mathbf{n})$ is increased. Furthermore, ergodicy has to be ensured. Equations (3.13) and (3.14) show that the acceptance probability is a function of the a priori probability of the trial as well as of the a priori probability of the reverse trial, which can be computationally expensive.

3.2.2 Grand Canonical Monte Carlo simulation of adsorption

In adsorption, the adsorbed phase on the porous material is in equilibrium with a reservoir, meaning that the chemical potential is the same for constant pressure and temperature. In the simulations of adsorption in this thesis, the adsorption volume is kept constant. Therefore, the grand canonical ensemble, where the chemical potential, the volume, and the temperature are constant, is chosen for the simulations of adsorption.

The trial moves that are used to generate the Markov chain of microstates in the grand canonical Monte Carlo (GCMC) simulation are: creating a molecule, deleting a molecule and moving a molecule. They are explained in detail below. By these Monte Carlo moves, the system moves towards equilibrium. Once this is reached, the configurations can be sampled. To obtain the thermodynamic property of interest, averaging over a large number of

configurations is necessary. For a simulation of adsorption, the number of molecules in the simulation volume is usually of main interest.

The acceptance probabilities of the trial moves are derived from the detailed balance condition given in (3.12). This general equation is specified for the grand canonical ensemble by substituting the probability densities $\rho(\mathbf{o})$ and $\rho(\mathbf{n})$ of the old and new configurations by equation (3.10).

$$\frac{P(\mathbf{o}\rightarrow\mathbf{n})}{P(\mathbf{n}\rightarrow\mathbf{o})}=\frac{\frac{1}{\Xi}\exp(-\beta U(\mathbf{o}))\prod_i\left(\frac{1}{N_i(\mathbf{o})!}\frac{V^{N_i(\mathbf{o})}}{\Lambda^{3N_i(\mathbf{o})}}\exp(\beta\mu_i N_i(\mathbf{o}))\right)}{\frac{1}{\Xi}\exp(-\beta U(\mathbf{n}))\prod_i\left(\frac{1}{N_i(\mathbf{n})!}\frac{V^{N_i(\mathbf{n})}}{\Lambda^{3N_i(\mathbf{n})}}\exp(\beta\mu_i N_i(\mathbf{n}))\right)} \tag{3.15}$$

Using the definition of the chemical potential

$$\mu_i=\frac{1}{\beta}\ln(\beta f_i\Lambda^3) \tag{3.16}$$

with f_i as the fugacity of species i in the bulk phase, gives

$$\frac{P(\mathbf{o}\rightarrow\mathbf{n})}{P(\mathbf{n}\rightarrow\mathbf{o})}=\prod_i\left(\frac{N_i(\mathbf{n})!}{N_i(\mathbf{o})!}(f_i\beta V)^{N_i(\mathbf{o})-N_i(\mathbf{n})}\right)\exp(-\beta\Delta U(\mathbf{o}\rightarrow\mathbf{n})) \tag{3.17}$$

The term $f_i\beta V$ is the dimensionless fugacity of species i. The calculation of the potential energy is addressed in Section 3.2.3 and this is referred to for the calculation of $\Delta U(\mathbf{o}\rightarrow\mathbf{n})$. The acceptance probabilities of the trials in the grand canonical Monte Carlo simulation are derived by substituting equation (3.17) into equation (3.13) and (3.14). The trials used in this work are introduced in the following part.

The creation and destruction of molecules are required parts of the GCMC simulation. These moves change the number of molecules in the adsorption volume and equilibrate its chemical potential with the adsorptive in the reservoir. For the creation trial, the species, the location within the GCMC volume as well as the orientation are random. Therefore, the a priori probability for the creation of a molecule of the species i is independent of the mole fraction in the bulk phase and the adsorbed phase and is given as

$$P_{gen}(\mathbf{o}\rightarrow\mathbf{n})=\frac{1}{N_{spec}} \tag{3.18}$$

where N_{spec} is the number of species in the system. The resulting acceptance criteria of a creation trial is

$$P_{acc}(\mathbf{o}\to\mathbf{n}) = \min\left(1, \frac{N_{spec}N_i(\mathbf{n})}{\sum_{j=1}^{N_{spec}} N_j(\mathbf{n})} \frac{f_i \beta V}{N_i(\mathbf{n})} \exp(-\beta u_m)\right) \tag{3.19}$$

In the destruction trial, every molecule in the GCMC volume has the same probability of being chosen. Therefore, the a priori probability of destructing a molecule of the species *i*, with N_i molecules of this species in the GCMC volume, is

$$P_{gen}(\mathbf{o}\to\mathbf{n}) = \frac{N_i(\mathbf{o})}{\sum_{j=1}^{N_{spec}} N_j(\mathbf{o})} \tag{3.20}$$

The resulting acceptance criteria for the destruction trial is

$$P_{acc}(\mathbf{o}\to\mathbf{n}) = \min\left(1, \frac{\sum_{j=1}^{N_{spec}} N_j(\mathbf{n})}{N_{spec}N_i(\mathbf{n})} \frac{N_i(\mathbf{n})}{f_i \beta V} \exp(\beta u_m)\right) \tag{3.21}$$

Translational and rotational moves alter the position and/or orientation of a randomly chosen molecule. In this way the configuration space is sampled. The move trial can be restricted to a certain distance. The number of molecules is constant and the difference in the potential is therefore due to the difference in the potential of the moved molecule. The acceptance criteria for the move trial is

$$P_{acc}(\mathbf{o}\to\mathbf{n}) = \min(1, \exp(-\beta\Delta U(\mathbf{o}\to\mathbf{n}))) \tag{3.22}$$

In order to efficiently create trial configurations for flexible chain molecules such as surface groups, the Configurational Bias Monte Carlo (CBMC) method is used. Inserting or moving a longer molecule often leads to overlapping with other molecules or the framework. In order to increase the acceptance probability, in CBMC, the chain is not inserted or moved as one but the beads of the chain are "grown", i.e. the positions are generated one after another. The choice of the position of a bead is biased due to the restrictions by its bonds to previously placed beads. The energy of the bead and its so called Rosenbluth weight are calculated. They are combined for all beads in the Rosenbluth factor, which replaces the Boltzmann factors in the acceptance criteria. CBMC and dual-cut-off CBMC are described in more detail in Frenkel and Smit (2002) and Vlugt *et al.* (1998).

3.2.3 Potentials

The potential functions describe the fluid-fluid and fluid-framework interactions in a Monte Carlo simulation. The change in the potential energy $\Delta U(\mathbf{o} \rightarrow \mathbf{n})$ used in the acceptance criteria of the Monte Carlo moves is calculated with these functions (compare equation (3.17) and the derived criteria for the different moves). Depending on the molecules involved, different interactions have to be included. For non-polar molecules, e.g. ethane, only the valence and dispersive interactions have to be considered. For flexible molecules, such as the organic surface groups, additional contributions due to bond stretching, bending or torsion have to be taken into account. Electrostatic interactions need to be included for quadrupolar molecules, e.g. carbon dioxide and for the light hydrogen molecule the contribution of the quantum effect is not negligible. The general calculation of these potentials is described in this section; the potential parameters used are listed in the corresponding chapters.

3.2.3.1 Lennard-Jones potential

The valence and dispersive interactions are represented by the Lennard-Jones potential. The molecules and porous materials are represented by Lennard-Jones sites and the resulting potential u_{ij} between two interaction sites i and j, is given by:

$$u_{ij}\left(r_{ij}\right) = 4\varepsilon_{ij}\left[\left(\frac{\sigma_{ij}}{r_{ij}}\right)^{12} - \left(\frac{\sigma_{ij}}{r_{ij}}\right)^{6}\right] \tag{3.23}$$

where σ_{ij} is the averaged site diameter of the interaction sites, ε_{ij} is the averaged potential well depth and r_{ij} is the distance between two sites i and j.

The fluids considered in this thesis are carbon dioxide, methane, ethane, propane, nitrogen and hydrogen. For carbon dioxide and nitrogen an atomistic representation was used (each atom is represented by a Lennard-Jones site), all other molecules are represented by a united atom model, i.e. the atoms are not represented individually but combined to interaction sites. Methane and hydrogen are represented by one Lennard-Jones site, ethane by two (each representing CH_3) and propane by three (CH_3-CH_2-CH_3). Each of these interaction sites is considered to be spherical.

To calculate the interaction between two different species, the Lorentz-Berthelot mixing rules are used:

$$\sigma_{ij} = 0.5\left(\sigma_i + \sigma_j\right) \tag{3.24}$$

$$\varepsilon_{ij} = \sqrt{\varepsilon_i \varepsilon_j} \tag{3.25}$$

The Lennard-Jones potential is a pairwise additive potential, i.e. the total interaction between the adsorbate interaction sites, U, is calculated as

$$U = \sum_i \sum_{j<i} u_{ij}\left(r_{ij}\right) \tag{3.26}$$

The Lennard-Jones potential is short-ranged and interactions become negligible after a certain distance. This is taken advantage of by introducing a cut-off radius that reduces the number of interactions calculated. Interactions beyond the cut-off radius are not taken into account and the interaction potential is set to 0 in these cases.

3.2.3.2 Interactions for flexible molecules

For flexible molecules, such as the organic surface groups in Chapter 7, the stretching, bending or torsion of bonds is taken into account. New configurations are generated using the CBMC algorithm (Section 3.2.2). The force field used for the surface group is the OPLS force field (Jorgensen *et al.* (1984), Rizzo and Jorgensen (1999), Jorgensen *et al.* (2004)) and the contributions are calculated in the following way:

$$u_{streching} = K_{stretch}\left(r_{ij} - r_{ij,0}\right)^2 \tag{3.27}$$

$$u_{bending} = K_{bend}\left(\theta_{ijk} - \theta_{ijk,0}\right)^2 \tag{3.28}$$

$$u_{torsion} = K_0 + \frac{1}{2}K_1\left(1+\cos\phi\right) + \frac{1}{2}K_2\left(1-\cos 2\phi\right) + \frac{1}{2}K_3\left(1+\cos 3\phi\right) \tag{3.29}$$

K are the force constants, $r_{ij,0}$ is the equilibrium distance and $\theta_{ijk,0}$ the equilibrium angle. The surface groups are not taken as completely flexible, e.g. ring structures are simulated as rigid. The interactions considered are listed in the potential description of the molecules.

3.2.3.3 Electrostatic interactions

In simulations containing quadrupolar molecules e.g. carbon dioxide, the electrostatic interactions are of importance. In this work, the quadrupolar moment is represented by effective point charges. For carbon dioxide, for example, a negative point charge $-q$ on the oxygen atoms is balanced by a positive point charge of $+2q$ in the centre of mass of the carbon atom. The Coulombic potential of a system containing point charges is calculated as

$$U_{Coul} = \sum_{i=1}^{N_q} \sum_{j=i+1}^{N_q} \frac{q_i q_j}{4\pi\varepsilon_0 r_{ij}} \tag{3.30}$$

where r_{ij} is the distance between the charges q_i and q_j. The electrostatic interaction is long ranging and a calculation over a large number of images would be required. To overcome this problem, the Ewald summation technique is used (Ewald (1921)). In this formalism,

each point charge is surrounded by a Gaussian charge distribution of equal magnitude and opposite sign with the width $\sqrt{2/\alpha}$. The resulting screened, short-ranged charges can be summed efficiently. The effect of the screening charge has to be cancelled and a compensating charge distribution is added. These charges can be represented by a Fourier series and therefore evaluated in reciprocal space. The total is then transferred back into real space and the resulting function for the Coulombic interaction in a cubic box with the unit cell length L after subtraction of the self-interaction becomes

$$U_{Ewald} = \frac{1}{2}\sum_{\mathbf{k}\neq 0}\sum_{i=1}^{N}\sum_{j=1}^{N}\frac{4\pi q_i q_j}{Vk^2}\exp\left[i\mathbf{k}\cdot\left(\mathbf{r}_i-\mathbf{r}_j\right)\right]\exp\left(\frac{-k^2}{4\alpha}\right) - \sqrt{\frac{\alpha}{\pi}}\sum_{i=1}^{N}q_i^2 + \frac{1}{2}\sum_{i\neq j}^{N}\frac{q_i q_j}{r_{ij}}\operatorname{erfc}\left(\sqrt{\alpha}r_{ij}\right) \tag{3.31}$$

where V is the volume of the simulation cell containing N charged particles, and $\mathbf{k} = (2\pi/L)\mathbf{l}$ with $\mathbf{l} = (l_x, l_y, l_z)$ the lattice vectors in Fourier space (Frenkel and Smit (2002)).

3.2.3.4 Quantum effect

For light molecules such as hydrogen, quantum effects become important at low temperature. This means that the thermodynamic properties divert from those of the corresponding classical fluid and these differences have to be accounted for in the simulation. Several methods have been used to implement the influence of the quantum effect and the approach used in this work is the Feynman-Hibbs effective potential method (Feynman and Hibbs (1965)). A quantum particle of mass m is represented by a Gaussian wave packet of width $\sqrt{\beta\hbar^2/12m}$ with $\beta=1/k_BT$ and ħ the reduced Planck's constant. The quantum partition function of such N particles can be written as

$$Z_{FH} = \frac{1}{N!}\left(\frac{m}{2\pi\beta\hbar^2}\right)^{3N/2}\int\ldots\int dr_1\ldots dr_N\exp\left[-\beta\sum_{i<j}U_{FH}\left(r_{ij}\right)\right] \tag{3.32}$$

where $U_{FH}(r)$ is the effective potential between a pair of molecules, with reduced mass μ. $U_{FH}(r)$ is obtained by a Taylor expansion truncated at the quadratic term (Sese (1995)):

$$U_{FH}\left(r\right) = U\left(r\right) + \frac{\beta\hbar^2}{24\mu}\nabla^2 U\left(r\right). \tag{3.33}$$

For $U(r)$ given by the Lennard-Jones interaction potential, the Laplacian becomes

$$\nabla^2 U(r) = U''(r) + \frac{2}{r} U'(r) = 4\varepsilon\left(\frac{132\sigma^{12}}{r^{14}} - \frac{30\sigma^6}{r^8}\right) \tag{3.34}$$

The quantum correction enlarges the effective diameter of the molecule leading to a lower adsorption which is observed for quantum molecules due to the Heisenberg uncertainty principle.

3.3 Comparison of simulated and experimental results

In this thesis, grand canonical Monte Carlo simulations are used for the simulations of adsorption. Trial configurations are generated by inserting, deleting and moving molecules and the trial configurations are accepted with a probability given in (3.19), (3.21) and (3.22). Once equilibrium is reached, configurations are sampled and properties of the ensemble, such as the number of molecules, are evaluated. The potential calculations are based on the models given in this chapter with the potential parameters and further simulation details given in the respective chapters. In order to compare the amount adsorbed obtained by simulations and experiments, the excess amounts adsorbed have to be calculated for the simulations since these are obtained from the volumetric adsorption measurements presented. The excess amount adsorbed is the amount that is in the pores of the material in addition to the amount expected due to the density of the bulk phase at the given conditions. By contrast, molecular simulation predicts the absolute number of sorbate molecules within the framework material at the given conditions. The excess adsorption, N_{ex}, is calculated from the absolute adsorption, N_{abs}, by subtracting the pore volume of the adsorbent, V_g, calculated as described by Myers and Monson (2002) multiplied by the density of the ambient gas phase, ρ_g, calculated with the Peng-Robinson equation of state:

$$N_{ex} = N_{abs} - V_g \rho_g \tag{3.35}$$

4 Adsorption on CuBTC

This chapter investigates the gas adsorption on CuBTC, a metal-organic framework introduced in Chapter 2. In order to validate the molecular models, a large set of experimental data preferably measured on the same sample is useful to exclude the influence of the synthesis and activation that can be very strong as discussed in Section 2.1. To provide a set of data, the adsorption isotherms at 298 K for methane, ethane, propane, carbon dioxide and nitrogen from low pressures up to 25 bar were measured and compared with simulation results. In addition, the adsorption of the equimolar methane-carbon dioxide mixture has been measured. To the best of our knowledge, experimental mixture adsorption isotherms on this material have not been reported in literature. The influence of the composition on the selectivity for methane-carbon dioxide, ethane-carbon dioxide and methane-ethane mixtures is investigated through simulation. The outline of this chapter is as follows: in Section 4.1, details of the experiments and the simulations are given. In Section 4.2, the material is characterised experimentally and theoretically. Section 4.3 gives the pure gas adsorption results with the accessibility of the small pores in CuBTC investigated in Section 4.4. The adsorption of gas mixtures is studied in Section 4.5 and the conclusions are given in Section 4.6.

4.1 Experiments and simulations

The sample of CuBTC that was used in this experimental study was synthesised by Bo Xiao in St. Andrews. The synthesis procedure is described in detail in the paper by Xiao *et al.* (2007). Adsorption experiments were performed as described in Section 3.1.

GCMC simulations of adsorption were done as described in Section 3.2. The MUltipurpose SImulation Code (MUSIC, Gupta *et al.* (2003)) was used for the simulation. Between $1 \cdot 10^7$ and $32 \cdot 10^7$ number of simulations steps were performed. The large number of simulation steps ensured that equilibrium was achieved also in the mixture simulations. The first half of the steps was used to equilibrate the system and the second for sampling.

For the parametrisation of MOF materials, three different force-fields have been widely used in the literature: UFF (Rappe *et al.* (1992)), Dreiding (Mayo *et al.* (1990)) and OPLS-AA (Jorgensen *et al.* (1996)). The UFF force field contains parameters for all atoms, the number of metal atoms for which parameters are available is limited in the Dreiding force field. The OPLS was parameterised for small organic molecules and does therefore not describe the

interaction with the metal (these parameters have to be taken from the UFF force field). Fairen-Jimenez *et al.* (2009) compared simulated isotherms and the heat of adsorption for these three force fields for two MOF materials (MIL-47 and IRMOF-1) and ZIF-8. The difference between the results of the different force fields was small indicating that the isotherms and heat of adsorption results are not very sensitive to the choice of the force field. The Lennard-Jones parameters for the framework atoms were taken from the Universal Force Field (UFF) by Rappe *et al.* (1992) and for the fluids from the transferable Potentials for Phase Equilibria (TraPPE) force field (Martin and Siepmann (1998), Potoff and Siepmann (2001)). The values used are summarised in Table 4-2 and the bond lengths given in Table 4-3. The C-O-C bond angle in carbon dioxide was 180° and the CH_3-CH_2-CH_3 angle in propane was set to 114°. The cut-off applied was 18.7 Å i.e. interactions beyond 18.7 Å were neglected. The framework-fluid potential was tabulated with a spacing of 0.2 Å. As in other simulation studies, in this thesis a model of the activated CuBTC structure with the water ligands removed is used in the simulations which corresponds to the sample used in the experiment. The activation before the experimental adsorption measurements removed these water ligands and the resulting colour change from turquoise to dark blue was observed. The CuBTC unit cell for the simulations is shown in Figure 4-1.

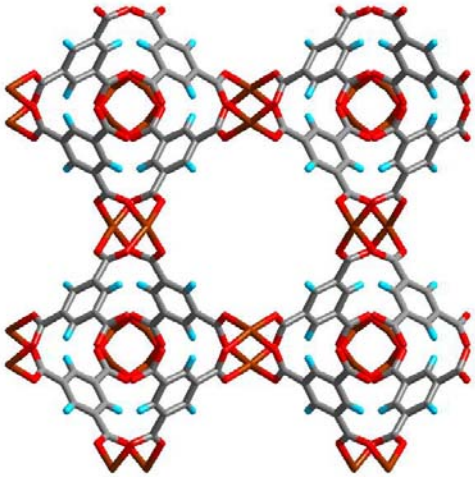

Figure 4-1 CuBTC framework, copper (brown), oxygen (red), carbon (grey) and hydrogen (light blue) atoms.

Partial charges for the framework were derived from density functional theory (DFT) calculations using a cluster approach by Gaetano Festa (a former postdoc in the group at the University of Edinburgh). Clusters were cut from the crystallographic unit cell and the resulting uncoordinated atoms were terminated by hydrogen atoms. A cluster size of 18 copper atoms was found to be sufficient to mimic the bulk. Different Pople basis sets were

tested and it was found that using a mixed basis set with 6-31+G(d) on the core atoms and the copper centres, and 6-31G on the remaining atoms resulted in a good compromise between accuracy and computational effort. The DFT calculations were performed with the Gaussian 03 package (Gaussian (2004)) using TPSS density functionals (Tao *et al.* (2003)). The charges of the framework were then calculated using the electrostatic potential derived method CHELPG (Breneman and Wiberg (1990)) and are listed in Table 4-1 with the sites shown in Figure 4-2. Electrostatic interactions were considered in the adsorption simulations of nitrogen and carbon dioxide and were calculated using Ewald summation (Section 3.2.3.3).

Table 4-1 Partial charges used for CuBTC.

Atom	Charge	Number in uc
Cu	0.989	48
C_1	-0.001	96
C_2	-0.131	96
C_3	0.679	96
O	-0.601	192
H	0.159	96

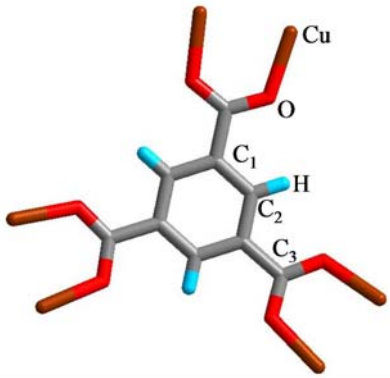

Figure 4-2 Linker CuBTC.

Table 4-2 Lennard-Jones potential parameters.

Species	Site	σ (Å)	εk_B^{-1} (K)	q (e)	Reference
CuBTC	O	3.118	30.2141	*a)*	Rappe *et al.* (1992)
	H	2.571	22.1570		
	C	3.431	52.8746		
	Cu	3.114	2.5178		
N_2	N	3.31	36.0	-0.482	Potoff and Siepmann (2001)
	Charge	0.0	0.0	+0.964	
CO_2	C	2.8	27.0	+0.70	Potoff and Siepmann (2001)
	O	3.05	79.0	-0.35	
CH_4	CH_4	3.73	148.0		Martin and Siepmann (1998)
C_2H_6	CH_3	3.75	98.0		Martin and Siepmann (1998)
C_3H_8	CH_3	3.75	98.0		
	CH_2	3.95	46.0		Martin and Siepmann (1998)

a) Partial charges for the atoms of the framework are displayed in Table 4-1.

Table 4-3 Bond lengths for fluids used in the simulation.

Species	Sites	Length (Å)	Reference
N_2	N-N	1.10	Potoff and Siepmann (2001)
	N-Charge	0.55	
CO_2	C-O	1.16	Potoff and Siepmann (2001)
C_2H_6	CH_3-CH_3	1.54	Martin and Siepmann (1998)
C_3H_8	CH_3-CH_2	1.54	Martin and Siepmann (1998)

4.2 Characterisation of CuBTC

As described in Chapter 2, the adsorption performance of MOFs is often not reproducible and therefore the characterisation is of high importance. The X-ray powder diffraction (XRD) is the first method used to characterise the sample. The obtained spectrum is distinctive for the material, where the positions of the peaks correspond to the spacing of the lattice. Spectra of materials are available in databases and are used for the identification of the material. Furthermore, XRD measurements can be used to detect changes in the structure after pelletisation or activation. The XRD spectrum for the pelletised material is given in Figure 4-3 a) and for the pelletised and activated sample in Figure 4-3 b). The sharp peaks in the spectra indicate that the crystallinity of the sample is preserved throughout the pre-treatment.

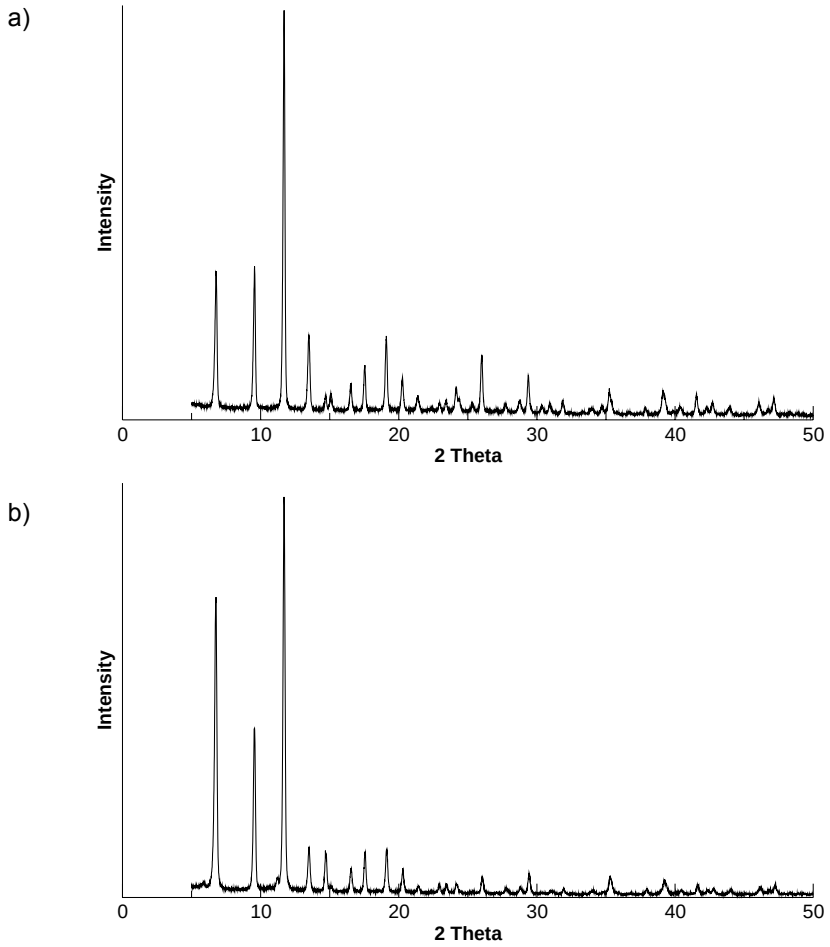

Figure 4-3 XRD spectrum of a) the pelletised and b) the pelletised and activated sample.

After the structure is determined by XRD measurements, further characteristic data can be obtained by adsorption measurements, for example the heat of adsorption and the surface area. For the characterisation of the CuBTC sample, a nitrogen isotherm at 77 K was measured by Bo Xiao at the University of St. Andrews, and from this the BET surface area was calculated. Furthermore, calorimetric data for carbon dioxide and methane measured on the same sample as used for the measurements of the isotherms was provided by Sandrine Bourelly from MADIREL, Université de Provence, CNRS Marseille.

Figure 4-4 shows the nitrogen isotherm at 77 K for the CuBTC sample used in this work together with the simulated isotherm.

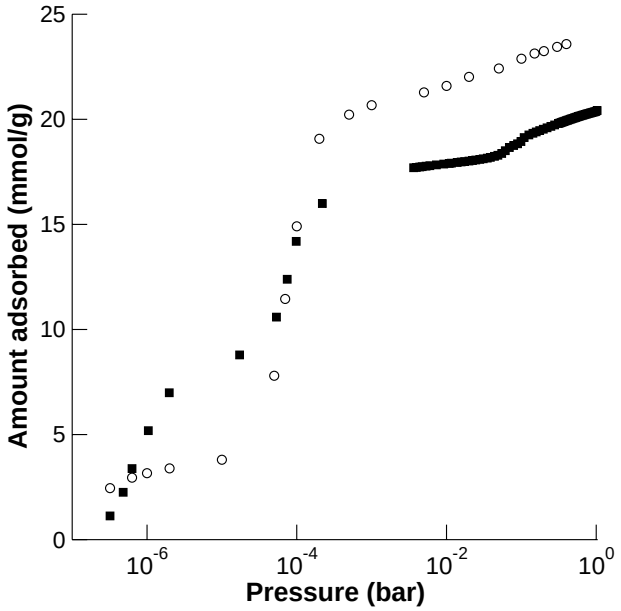

Figure 4-4 Simulated (○) and measured (■) nitrogen isotherms at 77 K.

The experimental nitrogen isotherm shows two characteristic steps that are also found in the simulated isotherm. It can be seen from the snapshot in Figure 4-5 that the first step corresponds to the filling of the small cavities. At $1 \cdot 10^{-5}$ bar, four nitrogen molecules are present in each small pore. In the experimental isotherm, the first step reaches a higher loading indicating that more molecules are adsorbed at low pressures. This could be due to high energy sites around the unsaturated copper atoms indicating that the force field and partial charges used in the simulations were not capturing this correctly. The second step occurs at the same pressure in the experimental and simulated isotherms. The material reaches a higher capacity in the simulation than in the experiment, which is expected due to the perfect crystal structure of the model compared to the experimental sample that exhibits defects and imperfections. The synthesised sample depends on the synthesis and pre-treatment as discussed in Chapter 2. The partial collapse of the framework or solvent/precursor molecules still present even after activation are examples of factors that reduce the free volume and in this way the amount adsorbed at high pressure.

Several published simulation studies use fitted force field parameters in order to achieve better agreement between experimental and simulation results (e.g. Yang and Zhong (2006a), Wang *et al.* (2008)). As shown in Section 2.1, experimental data can vary widely depending on the synthesis and activation procedure. Refitting force field parameters to one set of experimental adsorption data therefore results in a set of parameters unique to one

particular sample. The transferability of force field parameters is lost. Therefore, in this study the generic UFF force field was used without refitting any parameters.

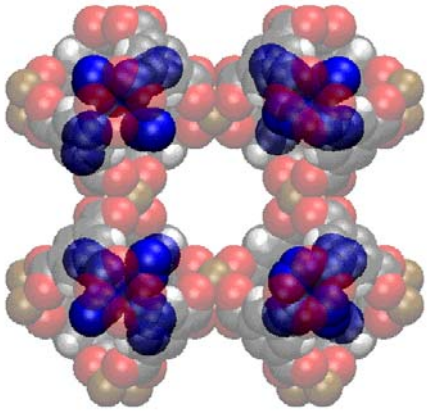

Figure 4-5 Snapshot at P = $1 \cdot 10^{-5}$ bar; N (blue), C (grey), O (red), H (white), Cu (brown). Framework atoms are transparent for better visibility of the adsorbed molecules.

4.2.1 Surface area

The surface area of a material is an important characteristic. It can not be directly measured and must be calculated from adsorption data assuming a model. The two models that are commonly used to calculate the surface area from nitrogen adsorption data at 77 K are the Langmuir (Langmuir (1916) and the BET model (Brunauer *et al.* (1938). Both methods assume close packing, the Langmuir model in a monolayer and the BET model in multilayers. If the pores are large enough that multilayers can form, the BET model is more appropriate.

In this work the BET equation was applied, which describes the multi-layer adsorption. The linearised equation reads

$$\frac{P}{V_{ads}\left(P_0 - P\right)} = \frac{1}{V_m c} + \frac{\left(c-1\right)P}{V_m c P_0} \tag{4.1}$$

For the analysis, the left side of the equation is plotted vs. P/P_0 which gives a linear plot for the pressure range of interest. P_0 is 1 bar and V_{ads} the volume of nitrogen adsorbed per gram of material at STP. The slope and y intercept of this linear region give the monolayer capacity, V_m. V_m is then used to calculate the surface area from $A = V_m \sigma N_{Av}$, where σ is the cross sectional area of the adsorbate at solid or liquid density (16.2 $Å^2$ for nitrogen, Adamson and Gast (1997)).

Consistency criteria have been proposed for choosing the pressure range for the calculation (Rouquerol *et al.* (2007)):

- The straight line fitted to the BET plot must have a positive intercept.
- The pressure range should be chosen so that $V_{ads}(1 - P/P_0)$ is always increasing with P/P_0.

In simulations, the surface area can be calculated in the same way as in experiments, i.e. simulating a nitrogen isotherm and applying the same analysis. The surface area acts as another indicator of the quality of the agreement between the experimental sample and the model in the simulation. The surface area can also be calculated using geometrical considerations which is a much quicker method. One way is to use the "accessible" surface area. It is calculated by "rolling" a probe molecule over the surface of the material. The surface area is calculated from the centre of the molecule and therefore the size of the molecule affects the result. To compare the accessible surface area with experimental results, a nitrogen sized molecule with a diameter of 3.681 Å was chosen. Düren *et al.* (2007) showed that the accessible surface area is the best geometrical method to calculate the surface area for comparison with experimental BET results for MOF materials.

Table 4-4 compares the experimental and simulated surface areas for CuBTC. The experimental surface area was obtained from the isotherm using the BET equation. The pressure range was chosen based on the criteria proposed by Rouquerol *et al.* (2007) and was $P/P_0 = 0.001\text{-}0.01$. The same procedure was applied for the simulated nitrogen isotherm. Here the pressure range that satisfied the criteria was at an even lower relative pressure of $P/P_0 = 0.0002\text{-}0.005$. The ratio between the BET values and the geometrical value is given as an indicator of how well the BET theory compares with the geometric value for this material.

Table 4-4 Surface areas for CuBTC obtained by experiment and simulation.

	Experimental	Simulated	
Method	BET	BET	"Rolling molecule"
P/P_0	0.001-0.01	0.0002-0.005	
Surface area (m^2/g)	1790.43	2076.07	2162.06
Ratio	0.828	0.960	1

As reported by Walton and Snurr for IRMOFs, the BET surface area calculated from the simulated isotherm are in good agreement with the geometrical value. The simulated and experimental BET surface areas agree well and the experimental value of 1790 m^2/g shows that the sample is highly crystalline and well activated.

4.2.2 Heat of adsorption

Experimentally, the heat of adsorption can be determined in different ways. A comparison of the three commonly used methods, differentiation of adsorption isotherms at constant loading, measurement of adsorption isosteres and calorimetry, is given by Shen *et al.* (2000). The experimental results in Chapter 4 were obtained by calorimetry, where the differential heat of adsorption is measured directly. The measurements for this work were done by Sandrine Bourelly from MADIREL, Université de Provence, CNRS Marseille.

To compare the experimental results with the simulation, the differential heat of adsorption can be calculated based on a classical thermodynamic treatment of the adsorption system at the fixed pressure P, temperature T and pore volume V (Vuong and Monson (1996)) as

$$q_d = u^b - \left(\frac{\partial U^a}{\partial N^a} \right)_{T,V} \tag{4.2}$$

where u^b is the internal energy of the bulk fluid, U^a is the configurational energy of the adsorbed fluid within the pore, and N^a is the number of molecules in the pore. Another way of calculating q_d is by using the fluctuation theory (Nicholson and Parsonage (1982)):

$$q_d = h^{b,r} - \frac{\langle NU \rangle - \langle N \rangle \langle U \rangle}{\langle NN \rangle - \langle N \rangle \langle N \rangle} \tag{4.3}$$

where the brackets, $\langle ... \rangle$, denote the ensemble average obtained from simulation and $h^{b,r}$ is the residual enthalpy of the bulk fluid. In GCMC simulations, the use of equation (4.3) has the advantage that it can be calculated directly during the simulation, whereas equation (4.2) requires either the fitting of U^a as a function of N^a for differentiation or a discrete approximation of the differential using changes in U^a and N^a from one isotherm point to the next. In this thesis, equation (4.3) is therefore used to calculate q_d.

Calorimetry measurements for carbon dioxide and methane on the same sample were done at 303 K. Figure 4-6 and Figure 4-7 show the results for methane and carbon dioxide at low pressure together with the simulated values. For methane, the values measured lie between 1-2 kJ/mol over the simulated results. The decreasing trend with pressure is found in both series and the overall agreement between simulation and experiment is good.

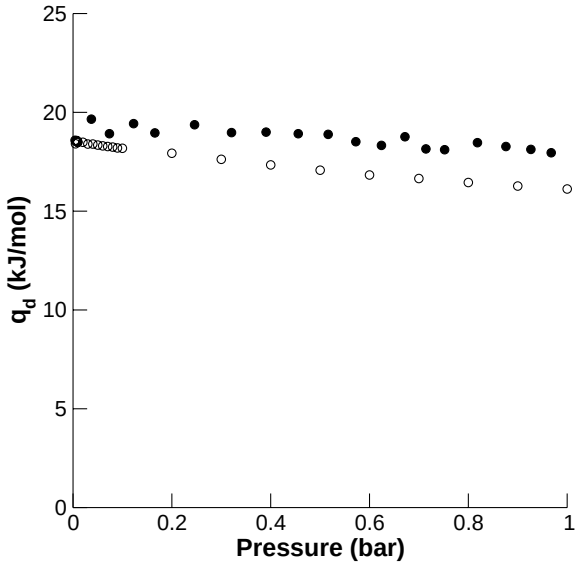

Figure 4-6 Heat of adsorption for methane at 303 K, experimental results (calorimeter, ●) and simulated values (○).

The difference between the calorimetric measurements and the simulated values is higher for carbon dioxide and ranges from 5 kJ/mol to 7.5 kJ/mol. Both curves show a very weak dependency on pressure in the pressure range measured. The decrease over pressure is found in the simulation whereas in the experiment a slight increase is measured. The larger difference in case of the carbon dioxide molecule with a quadrupole suggests that the electrostatic interactions might be stronger at this low coverage than represented in the model.

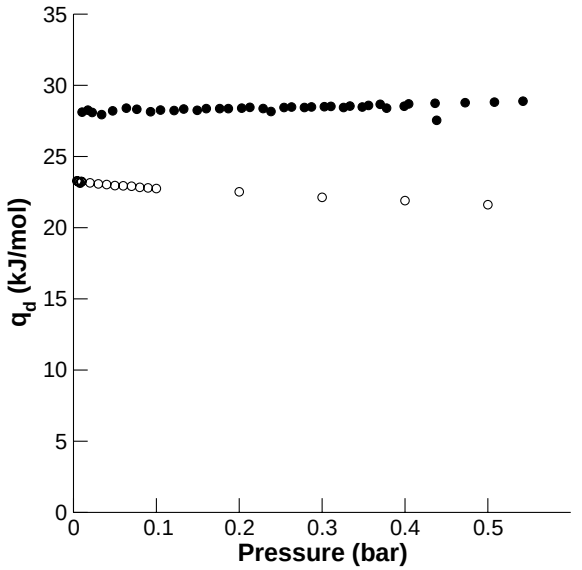

Figure 4-7 Heat of adsorption for carbon dioxide at 303 K, experimental results (calorimeter, ●, two data sets) and simulated values (○).

4.3 Single gas adsorption results

Experiments were carried out as described in Section 3.1 using the following gases: carbon dioxide, methane, ethane, propane and nitrogen. The isotherms were measured at 298 K. Each presented isotherm consists of at least two sets of data to verify the repeatability of the experiment. Carbon dioxide was the first gas to be investigated; and after measuring all single gas isotherms another carbon dioxide isotherm was measured. A further carbon dioxide adsorption was measured after the mixture isotherm. All three sets are combined in a single isotherm in Figure 4-8, showing that the experiments and the time in the rig (~ about five months) did not affect the performance of the sample.

From Figure 4-8 to Figure 4-12 the experimental isotherms for the different gases are shown together with the simulated isotherms. In general, at low pressure an isotherm provides information about the interaction of the fluid with the framework, whereas at high pressures, pore filling occurs and the total adsorption capacity of the material is obtained. To allow for a better description of the agreement in the low pressure range, the isotherms are shown with the pressure axis in log scale.

Figure 4-8 compares the experimental and simulated isotherms for carbon dioxide. The experimental uptake exceeds the values reported by Millward and Yaghi (2005) (which exceed the results obtained by Wang *et al.* (2002)) and is another indicator of the good quality of the sample used. The agreement with the simulated isotherms is very good up to 5 bar. At higher pressures, the measured and calculated isotherms deviate with a higher capacity given by the simulation. Deviations between simulations and experiments are expected as described for nitrogen.

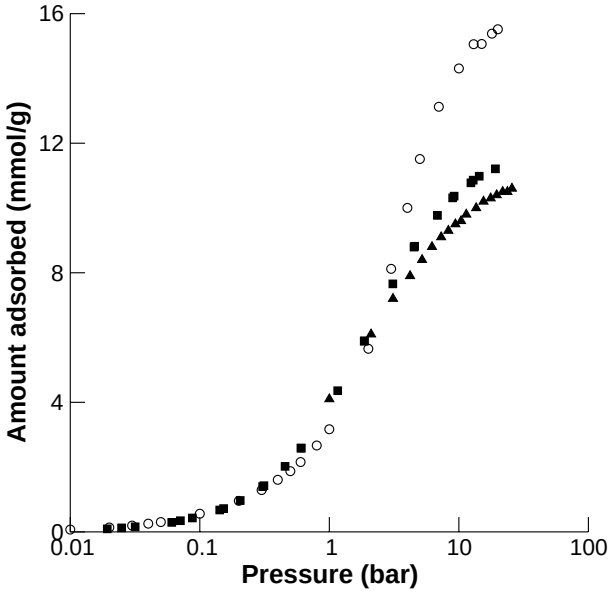

Figure 4-8 Carbon dioxide isotherms at 298 K: experimental results this work (■, three data sets), Millward and Yaghi (2005) (▲) and simulated results (○).

For methane, the agreement between simulation and experiment, as shown in Figure 4-9, is good over the whole pressure range. The amount adsorbed is higher in the simulations.

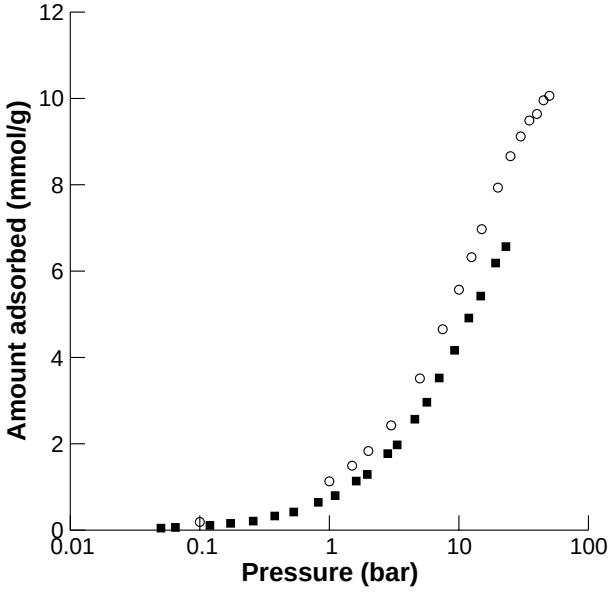

Figure 4-9 Methane isotherms: experimental results (■, two data sets) and simulations (○) at 298 K.

The isotherms for ethane are represented in Figure 4-10. The agreement between the measurements and simulations is similar to the one observed for carbon dioxide. A good fit up to about 1 bar is followed by an overprediction of the amount adsorbed at high pressures.

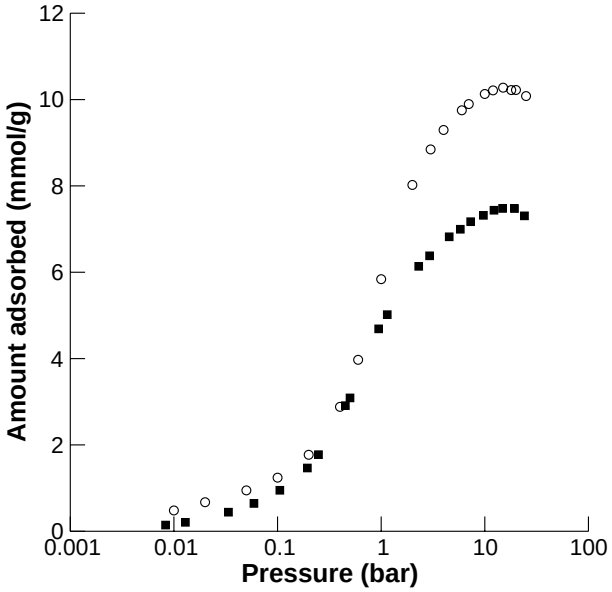

Figure 4-10 Ethane isotherms: Experimental results (■, two data sets) and simulation (○) at 298 K.

The propane isotherms in Figure 4-11 have the same shape. At high pressure, the behaviour is comparable with the other gases in that the simulation overpredicts the experimentally observed values for the amount adsorbed. Although for the other gases the agreement at low pressures is good, for propane the amount is also overpredicted in this pressure range. The simulation predicts an adsorption at low pressures whereas in the experiment no adsorption occurs below 0.005 bar. This disagreement might be caused by the size of the propane molecule. Propane is the largest molecule studied and the access to the smaller cavities could be restricted for it in the experiment whereas in the simulation all pores are accessible.

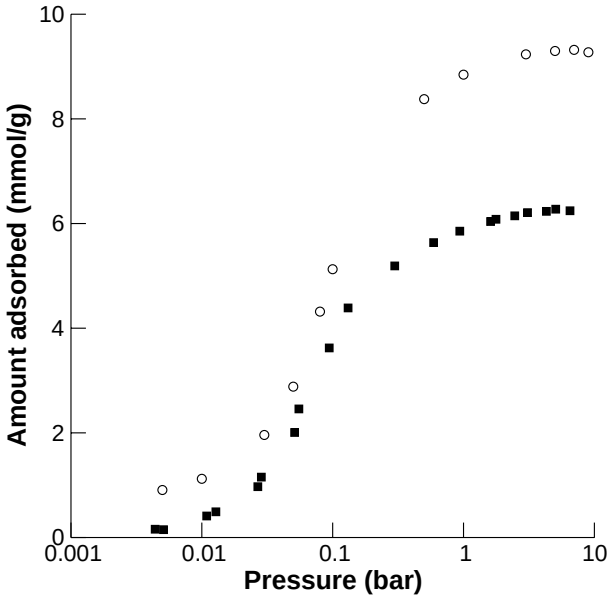

Figure 4-11 Propane isotherms: Experimental results (■, two data sets) and simulations (○) at 298 K.

The agreement for nitrogen between the simulated and measured isotherm is very good at low pressures. At higher pressures, the values in the simulation are higher than the experimentally measured ones. The steps observed in the isotherm at 77 K are not present at 298 K. At low temperatures, the movement of the molecules is restrained and the adsorbed molecules are sitting localised in the positions corresponding to high energetic interactions. At higher temperatures, the movement is increased and the energies experienced by the molecules have a broader distribution.

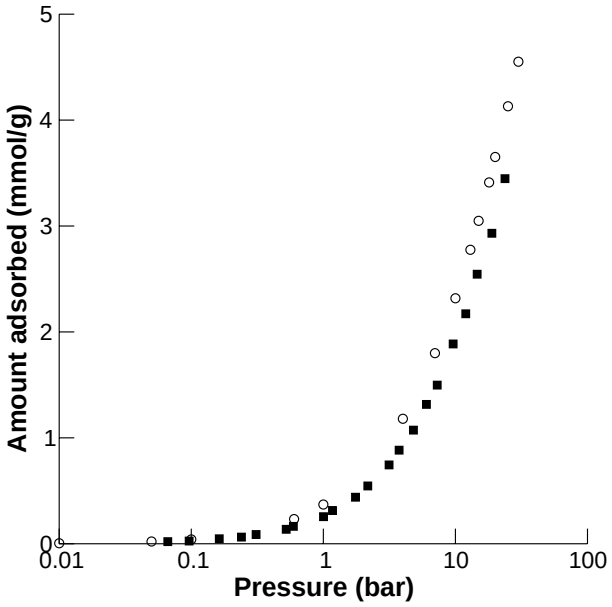

Figure 4-12 Nitrogen isotherm: Experimental result (■, two data sets) and simulation (○) at 298 K.

Summarising, the agreement between experiments and simulations is good at low pressures for all gases investigated, except for propane. This exception could be due to the inaccessibility of the small pores for propane which will be investigated in the next section. At high pressures, the experimental and simulated isotherms deviated considerably. The good agreement at low pressure is an indication that the fluid-framework interactions are represented well, deviations at higher pressure are caused by differences in the pore volume between the real and the ideal sample.

4.4 Accessibility of small pores

The framework consists of pores with three different sizes: two kinds of larger pores of about 10.2 Å and 12 Å in diameter and smaller octahedral ones with a diameter of about 4.8 Å. The pore sizes were obtained from the largest spheres fitting inside without overlapping with the framework atoms as described by Gelb and Gubbins (1999). The octahedral pores can only be accessed through triangular windows of about 3.5 Å. This size is very close to the size of the models for the hydrocarbons and the windows might restrict the available adsorption sites for these molecules by preventing them from entering the small pores.

Burde and Calbi (2007) investigated the adsorption in carbon nanopores and found that when $R \sim 0.95\ \sigma_{fc}$ (where R is the pore radius and σ_{fc} the fluid-carbon length parameter for the

Lennard-Jones potential) a potential barrier will develop and fluid molecules will have great difficulty penetrating inside the pore.

The values for 0.95 σ_{fc} for the fluids used in this study are listed in Table 4-5. Carbon was also chosen here as representative framework atom since the atoms surrounding the window are carbon atoms. For ethane and propane, this parameter is close to the diameter of the triangular windows and therefore simulations where insertions of molecules within the side pockets were not possible were also performed.

Table 4-5 Burde and Calbi parameter (0.95 σ_{fc}) for fluids used.

Gas	Carbon dioxide	Methane	Ethane	Propane	Nitrogen
$0.95 \cdot \sigma_{gf}$	3.0784	3.4014	3.4109	3.5059	3.2019

Figure 4-13 shows the isotherms for ethane comparing the simulation results with and without the small octahedral pockets with the experimental isotherm. The effect of the exclusion is highest at low pressures leading to a lower uptake. The difference becomes less pronounced with increasing pressure until at high pressures the difference disappears. Although the values at low pressure for the fully accessible model slightly overpredict the amount adsorbed it agrees better with the experimental values than the results for the restricted model that underpredicts the amount adsorbed up to pressures of 1 bar. Ethane molecules entered the small cavity with the translation move in the GCMC simulation. These findings indicate that the small cavities are generally accessible for ethane.

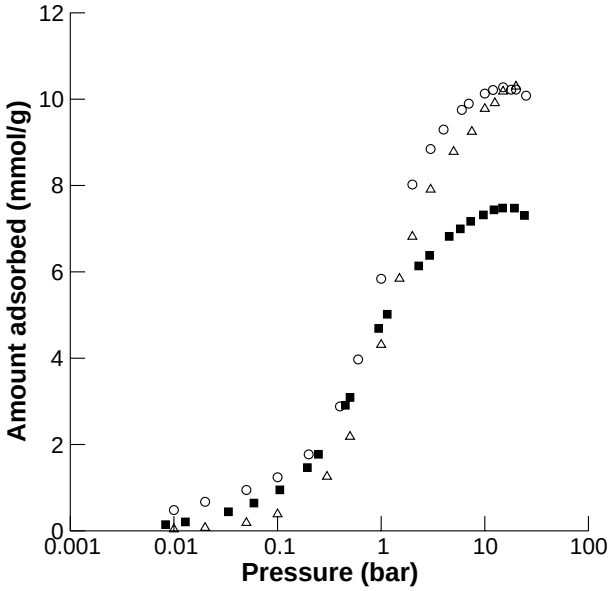

Figure 4-13 Ethane adsorption on CuBTC, comparison between simulations with all sites accessible (○) and exclusion of small pores (Δ) and experiment (■, two data sets).

For propane, the simulated isotherms with and without the small pores together with the experimental isotherm are shown in Figure 4-14. Preventing propane molecules to be inserted in the small pores results in a reduced amount adsorbed over the whole pressure range giving a better agreement with the experimental findings. The amount adsorbed is still overpredicted at pressures above 0.1 bar. The difference at high pressure between the two simulated isotherms show that no propane molecules are entering the small cavities and the predicted barrier is present. Whereas for ethane the small pockets are accessible, for propane the small windows prevent the molecules from entering.

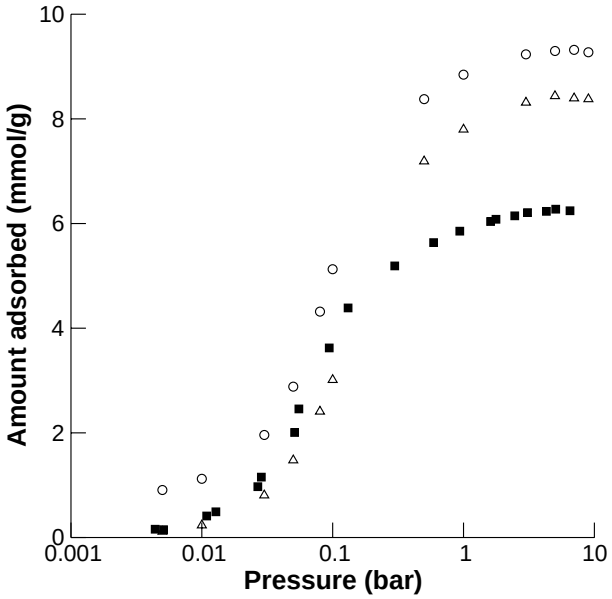

Figure 4-14 Propane adsorption on CuBTC, comparison between simulations with all sites accessible (○) and exclusion of small pores (Δ) and experiment (■, two data sets).

4.5 Adsorption of gas mixtures

Adsorption is widely used to separate gas mixtures. Separation is possible through either equilibrium, kinetic or steric mechanisms. If the molecules interact with a different strength with the material, a separation based in the equilibrium mechanism is possible, where the more strongly interacting fluid is enriched in the adsorbed phase. Kinetic separation relies on differences in the rate of adsorption and/or transport, and steric separation is possible if one of the fluids can not penetrate a large section of the material due to shape or size. GCMC simulations as well as the volumetric adsorption experiments give the amount adsorbed at equilibrium. No steric constrains were observed for methane, ethane or carbon dioxide in CuBTC. In this section, it is investigated if a separation based on the equilibrium mechanism can be achieved. For this, it is not only important to know how much of a single gas a material can store in equilibrium but also how selective this material is. The selectivity S is defined as

$$S(i/j) = \frac{x_i / y_i}{x_j / y_j}, \tag{4.4}$$

where x and y are the mole fractions of components i and j in the adsorbed and bulk gas phase, respectively. The higher the selectivity the better the separation of the fluids.

4.5.1 Carbon dioxide – methane mixtures

The experimental and simulated mixture isotherms for an equimolar mixture of methane and carbon dioxide at 263.9 K are shown in Figure 4-15. For carbon dioxide, the simulated amount adsorbed is higher for pressures above 1 bar than the experimental value. For methane, the amount adsorbed in the experiment exceeds the amount in the simulation. The overprediction of the amount adsorbed by simulation at high loading was shown for the single gas results (compare Figure 4-8 and Figure 4-9). The higher predicted values for the more strongly adsorbing carbon dioxide led to the underprediction of the methane values.

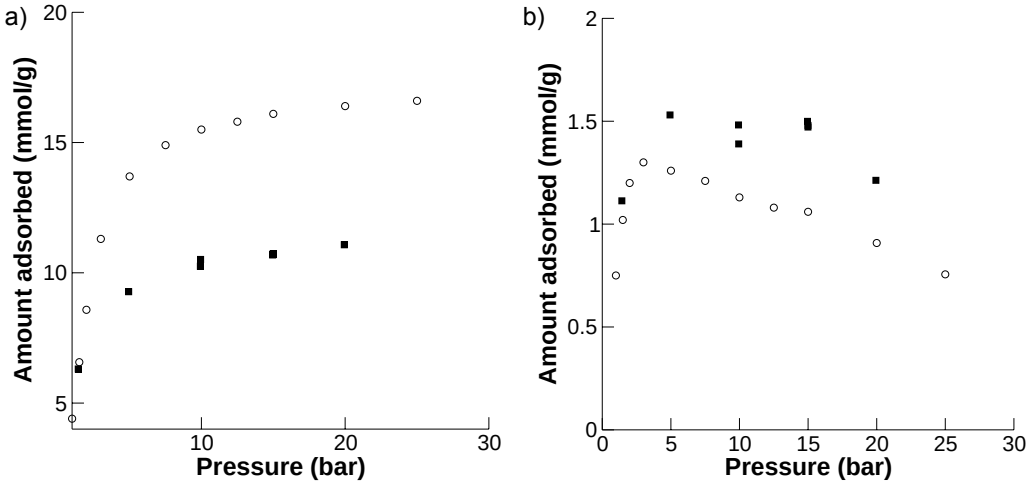

Figure 4-15 Simulated (○) and measured (■) isotherms for a) carbon dioxide and b) methane at 263.9 K from an equimolar mixture of carbon dioxide and methane.

The selectivity as a function of pressure is plotted in Figure 4-16. Both in the simulation and in the experiment a selectivity for carbon dioxide is observed. The selectivity in the simulation increases with pressure whereas in the experiment the selectivity does not change much in the pressure range investigated

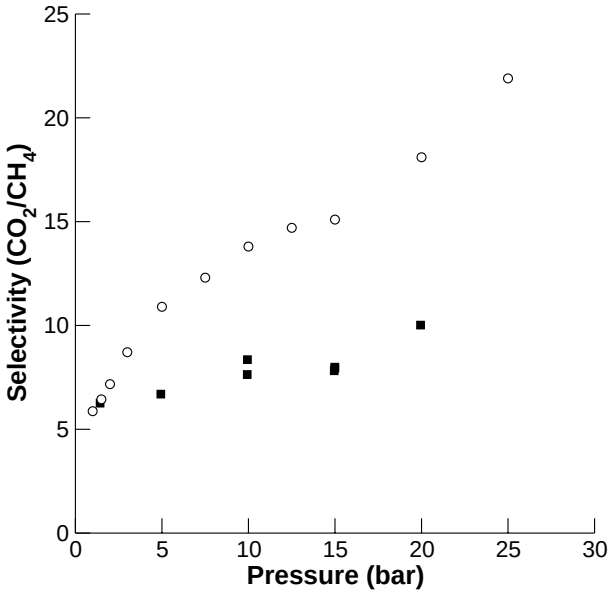

Figure 4-16 Simulated (○) and experimental (■) selectivity at 263 K.

Furthermore, the influence of the composition of the bulk phase on the selectivity was studied. Figure 4-17 shows the selectivity of carbon dioxide over methane for different compositions for 1, 5 and 20 bar. At 5 and 20 bar, an increase of the selectivity for carbon dioxide is observed related to the fraction of carbon dioxide in the gas phase. At 1 bar, the selectivity does not change much with the composition. At the same pressure, Yang and Zhong (2006b) also investigated the influence of the composition on the selectivity for a methane-carbon dioxide mixture at 298 K on CuBTC. They also observed a nearly constant selectivity over concentration but at a higher selectivity of just over 6. The difference in the results is due to differences in the potential parameters and partial charges. In their work, the LJ parameters for the framework were based on the OPLS-AA Force Field (except for Cu which was taken from the UFF) and were fitted to experimental data by Wang *et al.* (2002), whereas in this work the unchanged UFF parameters were used for all the atoms in CuBTC.

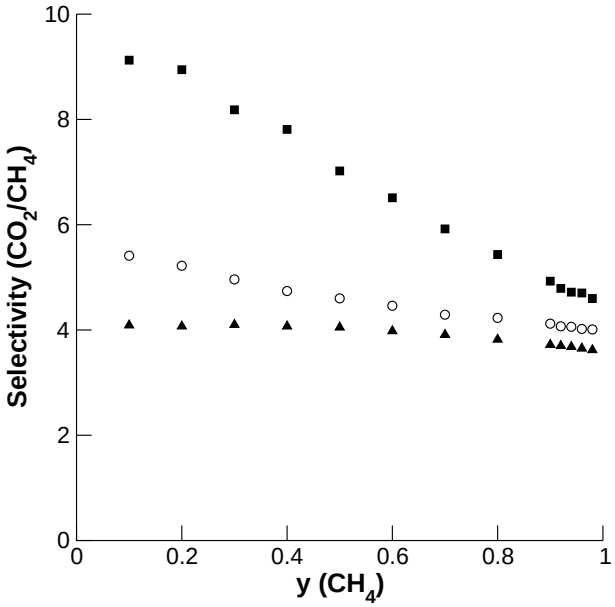

Figure 4-17 Selectivity of CO_2 over CH_4 for 1 (▲), 5 (○) and 20 (■) bar over the composition of the gas phase at 298 K

To investigate the molecular level mechanisms that lead to the macroscopically observed selectivity, energy histograms were used to analyse the interactions between the carbon dioxide molecules and the framework and the carbon dioxide molecules themselves. The energy histograms show the distribution of the energy of the adsorbed molecules. Histograms for the mixtures with 10 % methane in the gas phase are shown in Figure 4-18. This composition was chosen to find an explanation for the strong pressure dependence of the selectivity at high mole fractions of carbon dioxide in the bulk phase. In Figure 4-18 a) the energy of the molecules with the framework is displayed. The peak at low energy (< - 23 kJ/mol) is the contribution of molecules in the small pockets, higher energies belong to molecules in the bigger pores. At 20 bar, a small peak appears at energies between - 4 kJ/mol and - 1 kJ/mol. Pore filling occurs at this pressure and this peak corresponds to molecules in the centre of the large pores. At 1 bar, a high proportion of the molecules can be found in the small pores, at higher pressures this proportion in reduced since the small pores are filled and further molecules can only adsorb in the larger pores. The histograms at 5 bar and 20 bar are similar and do not explain the differences in the selectivity.

Figure 4-18 b) shows the histograms for the CO_2-CO_2 interactions. At 1 bar, about a quarter of the CO_2 molecules hardly interact with other CO_2 molecules as the loading is relatively low (89.5 CO_2 molecules/uc). At higher pressures, the loading increases (140 CO_2 molecules/uc at 20 bar) and each CO_2 molecule is attracted by other CO_2 molecules. This

interaction increases with pressure and at 20 bar the average contribution is -13 kJ/mol. The contribution of the Coulombic interactions for this condition is displayed separately and shows that the electrostatic interactions have a positive effect, which is investigated further in the next section.

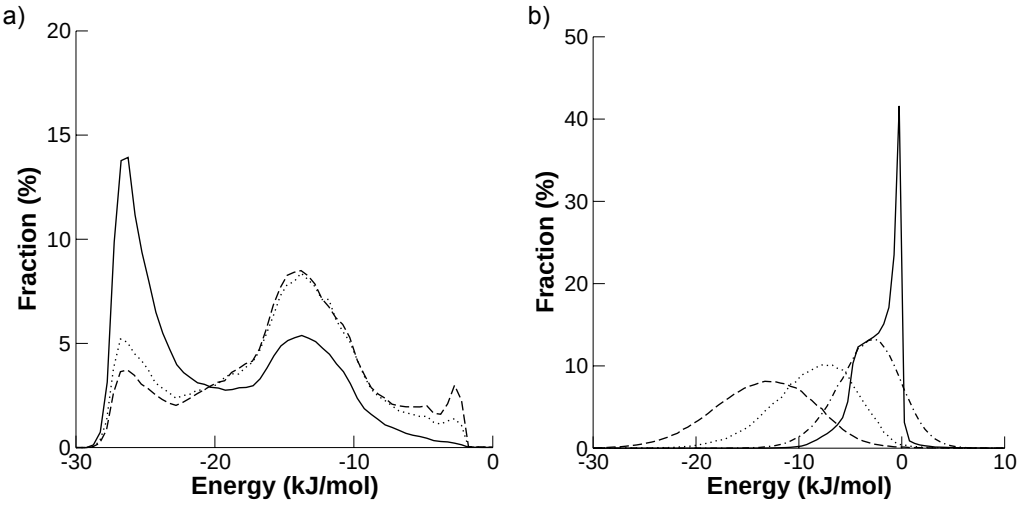

Figure 4-18 Energy histograms for y_{CH4} = 0.1 and 1 (solid line), 5 (dotted line) and 20 (dashed line) bar; a) CO_2-CuBTC interactions and b) CO_2-CO_2 interactions, the electrostatic contribution at 20 bar (dash-dotted line).

Influence of electrostatic interaction

In order to investigate the influence of the electrostatic interactions on the selectivity, simulations were carried out where these interactions were switched off partially or completely. Figure 4-19 shows the selectivity as function of the composition for these simulations at 5 bar. When the electrostatic interactions are switched off completely, the selectivity for carbon dioxide decreases considerably over the whole range of composition. The selectivity is nearly independent of the composition of the gas phase, increasing only slightly from 2.4 at y_{CH4} = 0.1 to 2.75 at y_{CH4} = 0.98.

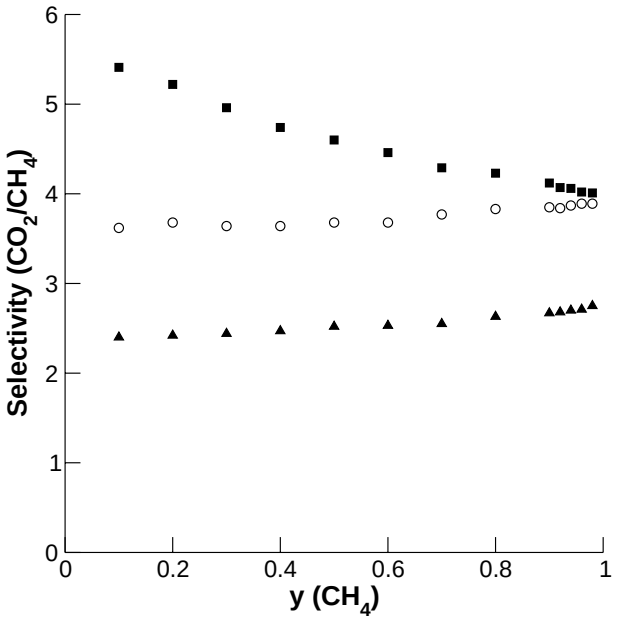

Figure 4-19 Influence of the electrostatic interactions for CO_2-CH_4 at 5 bar and 298 K. Selectivity of CO_2 over CH_4 over gas phase composition for a model with all interactions (■), only CO_2-framework electrostatic interactions (○) and no electrostatic interactions (▲).

Allowing only electrostatic interactions between the framework and the CO_2 molecules but not between the CO_2 molecules themselves, the selectivity increases evenly over the full range of composition compared to the system without any electrostatic contributions. Again, the increase in the selectivity with increasing methane content in the gas phase is only minor from 3.62 to 3.89.

The difference between this simulation and the simulation including all interactions are therefore the CO_2-CO_2 electrostatic interactions. Accounting for these results in a strong increase at high CO_2 concentrations dropping to a similar selectivity at low CO_2 concentrations compared to the case where these interactions where not considered. This indicates that when the CO_2 molecules are close enough to each other to interact, this interaction has a strong effect on the selectivity. This also explains why the selectivity increases strongly with pressure at high CO_2 concentrations in the bulk phase. Again, more CO_2 molecules are able to interact with each other and thus enhancing the selectivity. At high y_{CH4}, even at high pressure, only few CO_2 molecules are present (31 CO_2 molecules/uc at $y_{CH4} = 0.9$) and thus leading only to a small positive contribution of the CO_2-CO_2 interaction.

4.5.2 Ethane – methane mixtures

Mixtures of ethane and methane were studied by simulations investigating the influence of pressure and composition. Contrary to the methane-carbon dioxide mixtures investigated in the previous section, these mixtures consist of two unpolar components and the electrostatic interactions that influenced the selectivity for the methane – carbon dioxide mixtures are not present. Figure 4-20 shows the selectivity of ethane over methane for varying concentrations and pressures of 1, 5 and 20 bar.

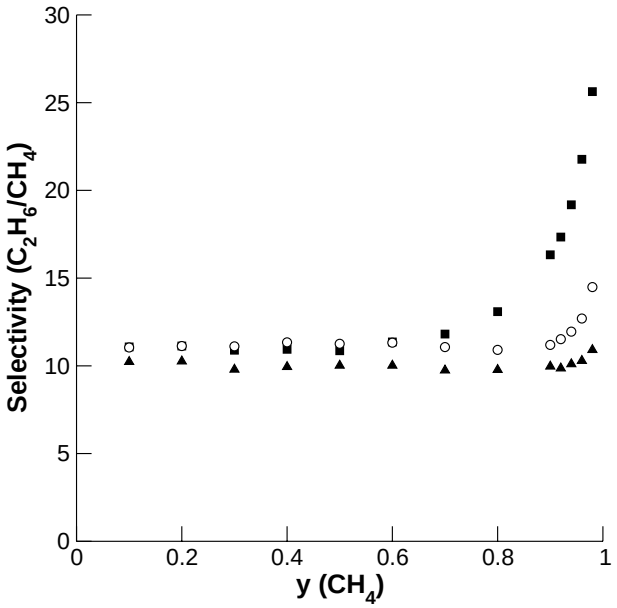

Figure 4-20 Selectivity of ethane over methane for 1 (■), 5 (○) and 20 (▲) bar over the gas phase composition at 298 K.

The selectivity changes very little in a wide range of composition. Overall, the selectivity of ethane over methane is higher than carbon dioxide over methane. At high methane concentrations in the bulk, the selectivity of ethane over methane is increasing exponentially. This indicates that although there are only few ethane molecules present these molecules adsorb preferentially. This finding is similar to the observations by Yang and Zhong (2006a) for the equimolar mixture where at low pressure the selectivity for ethane over methane increases sharply. The selectivity at 1 bar only deviates considerably from the selectivity at 20 bar at high methane loading. This means that not the relative low amount of ethane molecules but an absolute low amount leads to an additional increase in the selectivity due to the limited number of high energy interaction sites as illustrated by the histograms in the next paragraph.

To obtain more details about the interaction between the framework and the fluids, the energy histograms for three different gas compositions (y_{CH4} = 0.1, 0.5 and 0.98) at 1 bar are shown in Figure 4-21. The percentage of the molecules is plotted over the molecule-framework energy. The interaction between ethane and the framework (Figure 4-21 b) is stronger than the interaction of methane with the framework (Figure 4-21 a). At y_{CH4} = 0.1 and 0.5, the fraction of methane molecules that occupies a highly negative energy site (i.e. the strongest interaction sites) is very low, whereas for ethane, the sites with the high negative energy are fully occupied. Interestingly, at y_{CH4} = 0.98 the percentage of molecules occupying energy site with high interaction energies increases for both gases. Since only few ethane molecules are present, these molecules are located at these attractive sites, but they do not occupy all sites with a high interaction energy and therefore also the amount of methane molecules at these sites increases.

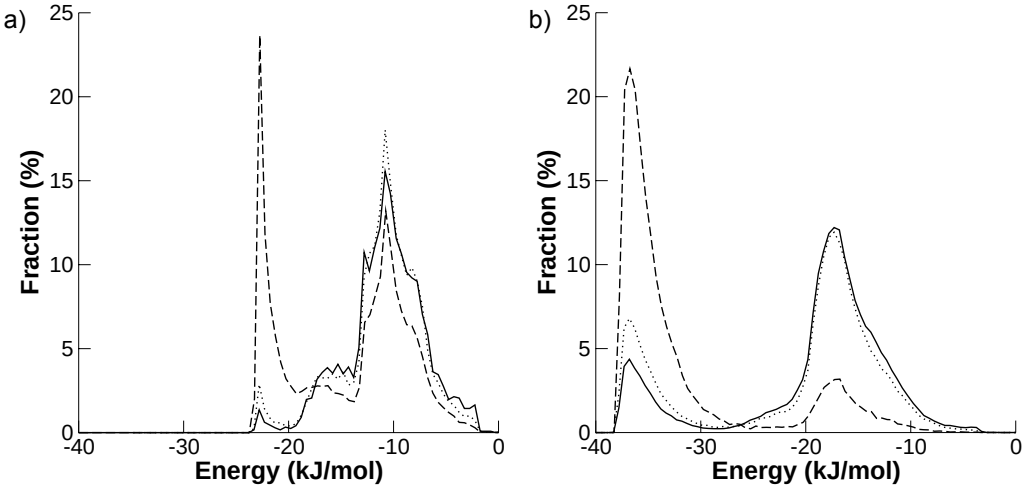

Figure 4-21 Energy histograms at 1 bar and 298 K with y_{CH4} = 0.1 (solid line), 0.5 (dotted line) and 0.98 (dashed line) for a) CH_4 and b) C_2H_6.

4.5.3 Ethane – carbon dioxide mixtures

In the previous sections, both ethane and carbon dioxide were shown to be selective over methane in the conditions investigated. It is therefore interesting to see how these molecules compete with each other. Ethane has a higher interaction potential which led to an increased selectivity at low ethane loadings. For carbon dioxide, the dispersive interactions are weaker but the Coulombic interactions increased the selectivity at high carbon dioxide loadings. Therefore, it is expected that for both species the same conditions are the most favourable to achieve high selectivities respectively, namely a low ethane/high carbon dioxide loading.

The selectivity for ethane-carbon dioxide mixtures at 298 K and for 1, 5 and 20 bar is shown in Figure 4-22. The selectivity is dependent on the pressure. At 1 bar, the selectivity is high for ethane and at 20 bar, the selectivity is close to unity, meaning no separation of the gases can be achieved. At 1 bar and low ethane loadings, the few ethane molecules are adsorbed preferentially and the selectivity increases, but not as much as in the mixture with methane (compare Figure 4-20). With increasing pressure, the favourable ethane-framework interactions become less important and the selectivity drops.

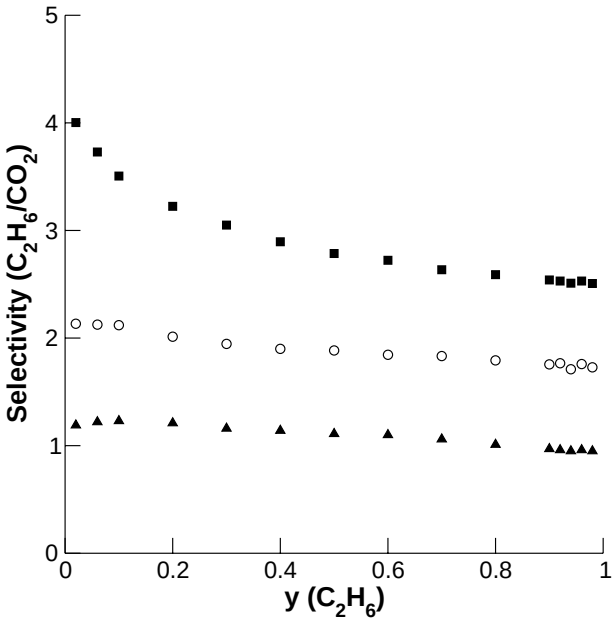

Figure 4-22 Selectivity of ethane over carbon dioxide for 1 (■), 5 (○) and 20 (▲) bar over the gas phase composition at 298 K.

As for the carbon dioxide-methane mixture, the influence of the electrostatic interactions is investigated. Figure 4-23 compares the selectivity for ethane over the gas phase composition. Disabling all electrostatic interactions, the selectivity for ethane increases over the whole range of gas compositions from 2.13 to 4.47 at $y_{C2H6} = 0.02$ and from 1.74 to 3.30 at $y_{C2H6} = 0.98$. Allowing for CO_2-CuBTC electrostatic interactions, the selectivity drops to the values with all interactions at high ethane loading in the gas phase. At high carbon dioxide loading the selectivity for ethane is still higher with up to 3.41 at $y_{C2H6} = 0.02$. This value falls to a similar value as at high ethane loading when all electrostatic interactions are taken into account. The CO_2-CO_2 electrostatic interactions only have an influence if sufficient carbon dioxide molecules are present. This was also observed for methane-carbon dioxide where it led to a high selectivity for carbon dioxide. Note that in Figure 4-19 the selectivity is given for carbon dioxide over methane whereas in Figure 4-23 the selectivity of ethane

over carbon dioxide is given (which is the inverse of the selectivity for carbon dioxide over ethane). The increase observed in Figure 4-19 and the decrease in Figure 4-23 at high carbon dioxide concentrations in the bulk phase show therefore the same trend. Contrary to the findings for the carbon dioxide-methane mixture, in the ethane-carbon dioxide mixture the CO_2-CO_2 electrostatic interactions do not create a big difference in selectivity but rather balance the interactions between ethane and carbon dioxide leading to a nearly constant low selectivity for ethane.

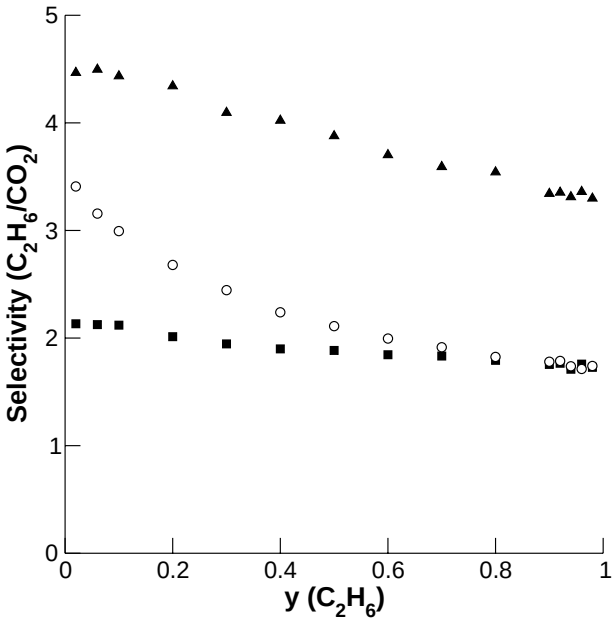

Figure 4-23 Influence of the electrostatic interactions for CO_2-C_2H_6 at 5 bar and 298 K. Selectivity of C_2H_6 over CO_2 over gas phase composition for a model with all interactions (■), only CO_2-framework electrostatic interactions (○) and no electrostatic interactions (▲).

4.6 Conclusions

Single gas high pressure isotherms were measured for carbon dioxide, methane, ethane, propane and nitrogen at 298 K. Simulations were performed for the same gases and showed a good agreement at low and medium pressures and a higher uptake at higher pressures than the experiments. The good agreement in the low pressure range indicates that the interactions between the gas molecules and the framework are well represented. One reason for the differences between experimental and simulated results could be the imperfections of the sample. Although the quality of the sample seems to be very high (higher uptake than other samples), the model in the simulation is an ideal crystal without defects. Furthermore, the

force field parameters used for the simulations were taken from a general force-field without any adjustments.

Furthermore, experimental and simulation data for a methane-carbon dioxide mixture was presented. The simulations over a range of compositions showed that the electrostatic interactions improve the selectivity for carbon dioxide in a mixture with methane. The selectivity increases especially at very high carbon dioxide loading due to the interactions of the carbon dioxide molecules with each other. The material is also selective for ethane over methane and the selectivity increases at low ethane loadings where the ethane molecules occupy the few locations of high energy in the small pockets. The material is less selective for ethane over carbon dioxide and at high pressures no selectivity is achieved since the stronger dispersive interaction of the ethane molecules with the framework are balanced by the electrostatic interactions of the carbon dioxide molecules.

5 Adsorption and desorption of hydrogen on MOFs

Hydrogen is an important gas used as energy storage. One of the aims is to use hydrogen more extensively as fuel in transportation. The U.S. Department of Energy (DOE) has therefore set goals (Department of Energy (2005)) for materials used for on-board hydrogen storage to make hydrogen powered vehicles a competitive alternative. The 2010 targets are 6.0 wt % and 45 kg H_2/m^3. For 2015 these targets are even more demanding with 9.0 wt % and 81 kg H_2/m^3. Furthermore, these conditions should be achieved at near ambient temperature and pressure. So far, no material has satisfied these expectations. The density of liquid hydrogen at 20 K and 1 atm is 70.8 kg/m^3 and therefore less than the target density. High hydrogen uptakes have been achieved with light metal hydrides (e.g. 11.4 wt % with $LiBH_4/½MgH_2$, Vajo *et al.* (2005)), but high temperatures (~ 400 °C) are required during the desorption step for these materials.

The unfavourable desorption conditions are due to the strong interactions upon the chemisorption of hydrogen. Physisorbed hydrogen on porous materials that is more easily desorbed has been investigated as an alternative. Physisorption has the advantage of complete reversibility and fast kinetics. The advantage of the weaker interactions upon desorption becomes a disadvantage upon adsorption where low temperatures are required to achieve high uptakes. At 77 K, a maximum storage capacity for zeolites has been calculated to be between 2.6 and 2.9 wt % (Vitillo *et al.* (2005)). Experimentally, carbon materials reach up to 5 wt % at 77 K and less than 1 % at room temperature as summarised by Rowsell and Yaghi (2005). Therefore, neither zeolites nor carbon materials will be able to reach the DOE targets.

Metal-organic frameworks have shown higher experimental uptakes than zeolites or carbons, e.g. for MOF-177 an hydrogen uptake of 7.5 wt % at 77 K and 70 bar was reported by Wong-Foy *et al.* (2006). For the application of MOFs as hydrogen storage materials for alternative fuels, the adsorption at room temperature is important but the reported hydrogen uptake in MOFs (and even more so for carbons and zeolites) is very low even at elevated pressures. Several strategies have been applied to increase the interaction energy between the framework and the hydrogen molecules in order to increase the storage capacities at low hydrogen pressures. Catenation (introduced in Section 2.1.2) was employed by Kesanli *et al.* (2005) who measured an uptake of 1.12 wt % at 298 K and 48 bar in a highly catenated zinc

based MOF. Impregnation (e.g. MOF-177 with C_{60} by Chae *et al.* (2004)) and open metal sites (Dincă and Long (2008)) are other strategies. Further information about different approaches to increase the hydrogen storage capacity can be found in the review by Rowsell and Yaghi (2005).

In order to increase the hydrogen storage capacity of MOFs, a better understanding of the interaction between hydrogen and the materials is necessary. Molecular simulations can help to interpret experimental findings. In this chapter, adsorption and thermal desorption of hydrogen on metal-organic frameworks is investigated. In Section 5.5, the thermal desorption spectroscopy is introduced and in Section 5.2 the simulation details are given. Hydrogen adsorption simulated hydrogen isotherms at 77 K are compared with experimental results in Section 5.3. In Section 5.4, the adsorption temperature in the simulations is lowered to 20 K, the starting temperature for the desorption spectra presented in Section 5.5. Simulated thermal desorption spectra are presented and compared with experimental results from the literature. The simulations help to explain features in the spectra and give insights into the effects of framework modifications.

5.1 Thermal desorption spectroscopy

With thermal desorption spectroscopy (also known as temperature programmed desorption) the desorption of molecules from a surface is studied. The material is loaded with a certain amount of gas molecules and slow heating provides the energy to desorb the molecules whose mass is detected with a mass spectrometer. The intensity of the peaks of the recorded curve gives the amount desorbed (after calibration) and the integral over the whole spectrum results the total initial amount adsorbed. The desorption temperature depends on the interaction of the sorbate with the surface; and the spectrum gives therefore information about the binding energy.

The aim of the simulations in this chapter is to reproduce the desorption results for hydrogen in MOF materials presented by Panella *et al.* (2008), thus giving further insight into the details of the desorption mechanism. The experimental method used by Panella *et al.* is as follows: prior to the measurement the sample was heated at 470 K in high vacuum ($< 10^{-5}$ mbar) for approximately 3 h to remove moisture and adsorbed gases. Then, at room temperature, a hydrogen pressure of 25 mbar was introduced into the reactor and the sample was slowly cooled down to approximately 20 K. After equilibrating for 30 min, the reactor was evacuated (final pressure ~ 10^{-7} mbar) to remove the non-adsorbed hydrogen molecules.

The temperature program was started with a heating rate of 0.1 K s^{-1} and the signal of desorbed hydrogen was recorded with the mass spectrometer up to 370 K, giving the desorption spectra which are discussed in Section 5.5.

According to Panella *et al.* (2008), the occurrence and location of the peaks in the desorption spectra are correlated to the pore size, giving a lower desorption temperature for larger pores. In this work, this relation is tested and the influence of modification of the framework on the desorption spectra assessed.

5.2 Simulation details

Grand canonical Monte Carlo simulations were used to obtain the isotherms and thermal desorption spectra. The MUltipurpose-SImulation-Code (MUSIC, Gupta *et al.* (2003)) was used. For the simulation of hydrogen on MOF materials, charged (Darkrim and Levesque (1998)) and uncharged (Buch (1994)) models have been used. For modelling hydrogen accurately, especially at low pressures, the effect of the quadrupole should be included. However, Garberoglio (2005) compared experimental hydrogen adsorption isotherms in IRMOF-1 with simulated results using the Buch potential and the potential by Darkrim and Levesque. The agreement with the data obtained with the uncharged potential was good whereas the charged model overpredicted the results considerably. Liu (2007a) used the model by Buch to simulate the hydrogen adsorption in CuBTC and compared the results to his experimental results on a high quality sample. The fit at high pressure was good but at low pressures the model underpredicted the adsorption. In this work, the potential parameters for hydrogen were taken from Buch (1994) and a second order FH correction (Section 3.2.3.4) was used to account for quantum effects. The potential parameters for the MOF materials were taken from the Universal Force Field (UFF) by Rappe *et al.* (1992). A cut-off of 17 Å was used. The Lennard-Jones potential parameters used are listed in Table 4-2. A potential map was employed for the hydrogen-framework interactions with a spacing of 0.1 Å. The influence of the quadrupole and the polarisability were not considered. The frameworks were kept rigid throughout the simulations. Eleven different MOFs were investigated and the properties of the materials are summarised in Table 5-2.

Table 5-1 Lennard-Jones potential parameters.

Species	Site	σ (Å)	εk_B^{-1} (K)	Reference
MOFs (UFF)	Zn	2.462	62.4424	Rappe *et al*. (1992)
	O	3.118	30.2141	
	H	2.571	22.1570	
	C	3.431	52.8746	
	Cu	3.114	2.5178	
	Br	3.732	126.393	
	Al	4.008	254.296	
	Cr	2.693	7.5533	
H_2 (1LJ)		2.958	36.700	Buch (1994)

Table 5-2 Properties of the materials used in this work.

Material	Mass (g/mol uc)	Free volume [a] (Å^3)	Crystal density (g /cm^3)	Pore sizes [b] (Å)
CuBTC	9199.680	13708.5	0.838	4.8, 10.2, 12.0
IRMOF-1	6155.840	14169.2	0.595	11.0, 14.2
IRMOF-2	8049.656	13384.8	0.783	9.1, 12.2
IRMOF-7	7355.840	13272.8	0.711	10.0
IRMOF-8	7351.840	23770.8	0.450	12.6, 17.0
IRMOF-9	15959.68	31672.4	0.658	6.5, 8.1, 10.5
IRMOF-10	7979.840	36354.9	0.330	16.7, 19.9
IRMOF-13	18263.68	30322.0	0.754	4.1, 5.1, 6.5, 7.5, 11.6
IRMOF-14	9131.840	36769.3	0.374	14.7, 19.9
MIL-53-Cr	931.984	876.0	1.038	6.6
MIL-53-Al	831.928	943.5	0.982	6.3

[a] The free volume is calculated with the second virial coefficient as described in Myers and Monson (2002). [b] The pore sizes are determined as described by Gelb and Gubbins (1999).

As a first step, hydrogen adsorption isotherms at 77 K were calculated to see the quality of the fit with the experimental results. Secondly, the desorption spectra were calculated. This was done as following:

- The adsorption isotherms at 20 K were simulated.
- Starting configurations were chosen corresponding to the experimental loading or pressure reported by Panella *et al.* (2008).
- The temperature of the simulation was subsequently increased by 0.5 K and an equilibrium configuration sampled. This step was repeated until all molecules had desorbed.
- The desorption rate was calculated as

$$D = (N_{Ti} - N_{Ti+1})/(T_{i+1} - T_i) \tag{5.1}$$

where N_T is the number of molecules adsorbed at the temperature T with $T_{i+1} > T_i$. Plotting the desorption rate over time gave the desorption spectra.

5.3 Hydrogen adsorption at 77 K

Figure 5-1 and Figure 5-2 compare the simulated hydrogen isotherms at 77 K with the experimental isotherms reported by Panella *et al.* (2008).

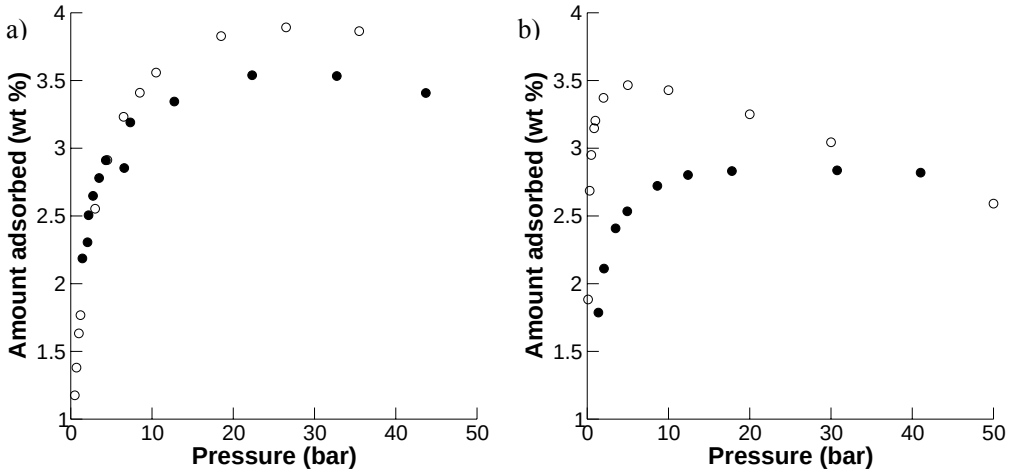

Figure 5-1 Isotherms at 77 K for hydrogen in a) CuBTC and in b) MIL-53-Al. Simulations (○), measured isotherms by Panella *et al.* (2008) (●).

For CuBTC, the isotherms agree well at low pressure as shown in Figure 5-1 a). At high pressure the amount adsorbed is overpredicted by the simulation. In general, a perfect fit between simulations and experiments is unlikely since the framework in the simulation is modelled as a perfect crystal without any defects and no solvent or other guest molecules present. As shown in Figure 2-2, the experimentally measured hydrogen uptake depends strongly on the synthesis and activation. Furthermore, the force fields simplify the interactions and the parameters used are taken from a general force field. Considering these factors, the fit is very good. For MIL-53-Al, Figure 5-1 b) shows that the simulations overpredict the amount adsorbed. This is especially pronounced at low pressures. Higher experimental adsorption in MIL-53-Al has been reported, exceeding 3.5 wt % (Férey *et al.* (2003)). The framework of MIL-53 is flexible and a breathing effect has been reported for MIL-53 upon hydration and dehydration (Serre *et al.* (2002)). Hydrogen could also have an effect on the framework affecting the accessibility of the adsorption sites at low pressures. The framework flexibility is not accounted for in the simulation and the dehydrated, open framework is used (Figure 2-7 b)).

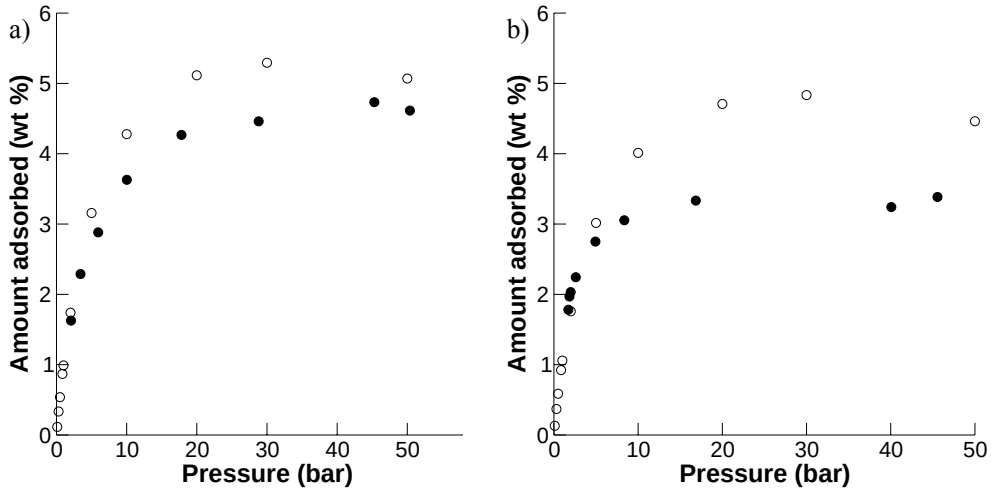

Figure 5-2 Isotherms at 77 K for hydrogen in a) IRMOF-1 and b) IRMOF-8. Simulations (○), measured isotherms by Panella *et al.* (2008) (●).

Figure 5-2 a) compares the results for IRMOF-1, which show good agreement. Again, at high pressure, the simulated amount adsorbed is increased compared to the experiment. For IRMOF-8, the framework in the experiment is saturated at a lower pressure and a lower loading, the amount adsorbed reaching a plateau at a lower pressure and with less amount adsorbed in Figure 5-2 b). Panella *et al.* (2008) suggested that the structure might be catenated (interlinked as shown in Figure 2-6). Due to a restricted pore volume of a catenated structure, the reduced amount adsorbed upon saturation is expected. At low pressure, catenation increases the adsorption due to additional adsorption sites created by smaller pores but the effect is reduced by the increased density in the gravimetric representation. The low pressure region is not sufficiently represented in the experimental data to give more information.

5.4 Hydrogen adsorption at 20 K

Experimental low temperature isotherms are usually measured at 77 K, the boiling point of nitrogen. In simulations, the temperature can easily be fixed to any given value and extreme conditions can be achieved. Low temperatures lead to adsorption at very low pressures, which can be also more easily adjusted in the simulations. Simulated isotherms at 20 K, the starting temperature for the desorption spectra, are shown in Figure 5-3.

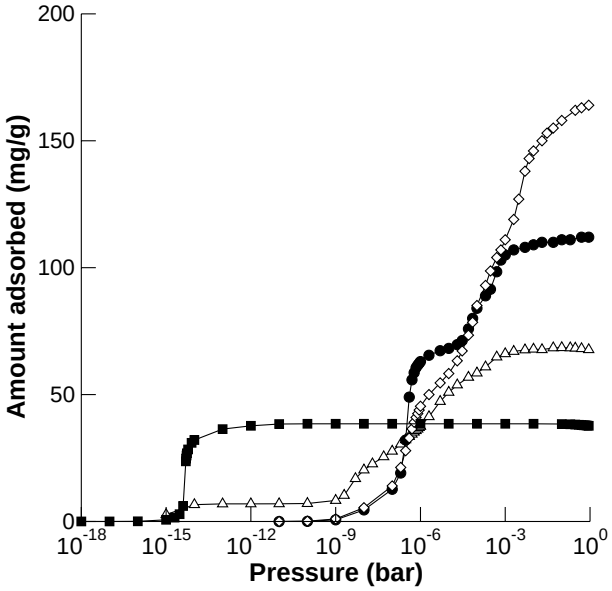

Figure 5-3 Simulated hydrogen isotherms at 20 K. CuBTC (Δ), IRMOF-1 (●), IRMOF-8 (◊), MIL-53-Al (■), lines are drawn to guide the eye.

The pressure axis is plotted in logarithmic scale for better visibility of the steps in the isotherm. MIL-53-Al adsorbs the first molecules at a low pressure of about $4 \cdot 10^{-15}$ bar. MIL-53-Al has a 1-D pore system with a pore size of 6.3 Å (Figure 2-7 b)). In small pores, the interaction with the framework is increased due to overlapping potentials from several framework atoms. The pore is so small that even at high pressures each molecule in the pores occupies a position close to the framework as shown in Figure 5-4. This leads to a quick filling of the pore and it reaches the full capacity below $1 \cdot 10^{-12}$ bar.

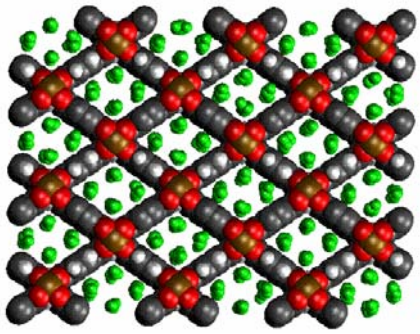

Figure 5-4 Snapshot for hydrogen (green, size scaled by 0.5) adsorbed in MIL-53-Al at 20 K and 0.9 bar.

CuBTC shows a first uptake at about $1 \cdot 10^{-15}$ bar. Up to $1 \cdot 10^{-9}$ bar, molecules only adsorb in the smaller pores of the framework. These are already filled at $1 \cdot 10^{-14}$ bar with four hydrogen molecules in each tetrahedral pocket, one molecule in each corner which is shown in the

snapshot in Figure 5-5. Several experimental studies observed a high attraction of the hydrogen molecules towards the unsaturated copper atoms, stating that the first molecules adsorb around it (Bordiga *et al.* (2007), Liu *et al.* (2007b), Vitillo *et al.* (2008)). The strong interaction between the hydrogen molecules and the open metal sites was also confirmed by the DFT by Yang and Zhong (2006c). This is not observed in this simulation since effects of polarisation and the influence of the quadrupole are neglected. Around $1 \cdot 10^{-9}$ bar, hydrogen starts to adsorb in the bigger pores. This is the same pressure range as the first uptake in IRMOF-1 and IRMOF-8.

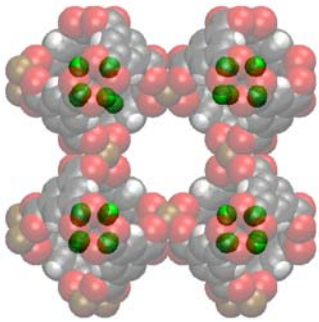

Figure 5-5 Snapshot for hydrogen (green, size scaled by 0.6) adsorbed in CuBTC at 20 K and $1 \cdot 10^{-10}$ bar. The framework atoms are transparent for better visibility of the adsorbed hydrogen molecules.

IRMOF-1 and IRMOF-8 have very similar hydrogen adsorption isotherms. The adsorption isotherms show two steps. At very low pressures, the molecules adsorb in the corner of the framework (Figure 5-6 a). The first step corresponds to a filling of the corner and the centre of the linker (Figure 5-6 b). The second step corresponds to the pore filling. Whereas the location of the first step is observed for the same pressure range for IRMOF-1 and IRMOF-8 due to the similarity of the attractive adsorption sites, the maximum amount adsorbed is higher in IRMOF-8 as this material has larger pores and a larger pore volume (compare Table 5-2).

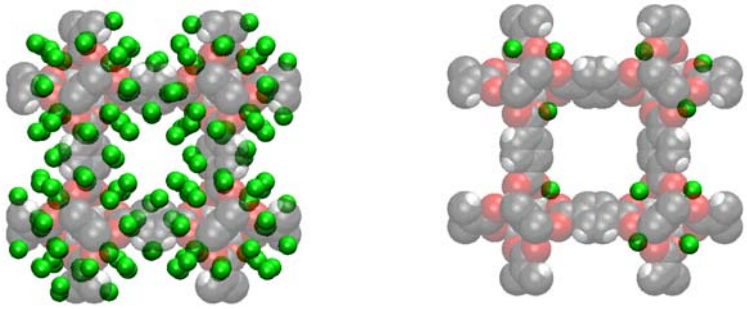

Figure 5-6 Snapshot for hydrogen (green, size scaled by 0.6) adsorbed on IRMOF-1 at 20 K. a) P = $1 \cdot 10^{-8}$ bar, b) P = $2 \cdot 10^{-6}$ bar. Framework atoms are transparent for better visibility of the hydrogen atoms.

5.5 Desorption spectra

The simulation of thermal desorption differs from the simulation of adsorption/desorption isotherms in that respect that the temperature varies and the pressure is kept constant. The pressure that is used during the desorption simulation determines the starting configuration and the desorption strength. Using a higher vacuum, less molecules will adsorb in the starting configuration and the desorption step will occur earlier. Due to the nature of the simulation technique, the influence of the pressure and the starting loading can not be investigated independently, since fixing one determines the other at a given temperature. MIL-53-Al is the only structure that shows sufficient adsorption in the simulations at the high vacuum of about $1 \cdot 10^{-10}$ bar that was used during the experiment.

For a comparison with the experimental values, starting configurations were chosen that correspond to the loading reported. For MIL-53-Al, this configuration is at a lower pressure than the reported pressure and the configuration at $1 \cdot 10^{-10}$ bar was used. The starting configurations are summarised in Table 5-3.

Table 5-3 Starting configurations for desorption.

Material	Wt %	Molecules/uc	Pressure (10^{-7} bar)
IRMOF-1	2.5	76.9	2.56
CuBTC	3.3	151.8	3.6
IRMOF-8	2.5	91.9	2.5
MIL-53-Al	3.8	16.0	0.001

The desorption rate was calculated according to equation (5.1) and the experimental and simulated spectra are shown in Figure 5-7. In the desorption spectra, the desorption rate is plotted over temperature. The weakly interacting molecules desorb already at low temperatures, whereas the molecules that interact more strongly desorb at higher

temperatures. The temperature scale in the graphs is up to 100 K in the experiments and up to 50 K in the simulations. In the simulations, the desorption is completed at lower temperatures than in the experiment. One reason could be that the temperature in the experiment is raised by 0.1 Ks^{-1} and equilibrium might not be achieved in every instant. Furthermore, electrostatic interactions and induction are not accounted for in the simulations but at these low temperatures and low loadings these might increase the interaction between

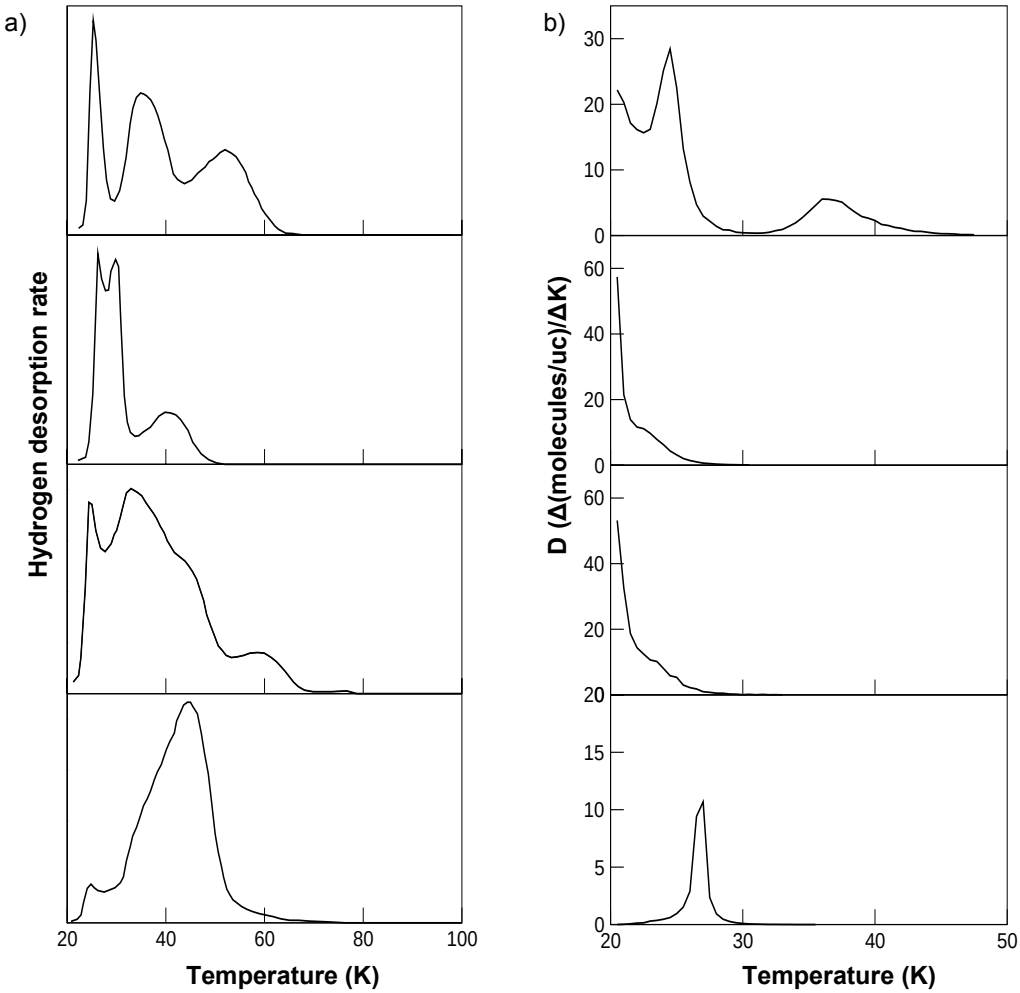

Figure 5-7 Desorption spectra for CuBTC, IRMOF-1, IRMOF-8 and MIL-53-Al (top to bottom), a) experimental data. Figure adapted with permission from Panella *et al.* (2008). Copyright Wiley-VCH Verlag GmbH & Co. KGaA
b) simulated spectra.

The first peak in the experimental data at around 25 K was attributed to liquid hydrogen or lightly adsorbed molecules in multilayers by Panella *et al.* (2008). This hydrogen does not interact with the framework and this peak was found to be influenced by the experimental

conditions rather than the MOF used and is therefore not characteristic for the material. They concluded that the peak below 27 K should thus be disregarded and not be included in the analysis for the material. We are following this suggestion and analyse and compare the desorption spectra excluding the experimental data below 27 K.

CuBTC shows two peaks in the desorption spectra, in the experiments as well as in the simulation. By carefully analysing simulation snapshots, each peak can be attributed to the desorption in specific pores: the first peak (around 35 K in the experiment / 24.5 K in the simulations) to the larger cavities of 10.2 and 12.0 Å and the second one (around 52 K in the experiments / 36.5 K in the simulations) to the smaller one of 4.8 Å. This indicates that the molecules in the smaller pores interact more strongly with the framework than the molecules in the larger cavities.

For IRMOF-1, a high and narrow peak is followed by a broader small peak completing the desorption at about 50 K. This was explained by Panella *et al.* as desorption occurring first in the larger pores of 15 Å and then in the pores of 12 Å. The experimental spectra for IRMOF-1 and IRMOF-8 show a surprising difference, given that the structures are very similar. In IRMOF-8, the benzenedicarboxylate linker of IRMOF-1 is replaced by a naphthalene-2,6-dicarboxylate one (Figure 2-5). For IRMOF-8, the initial strong desorption rate drops much more slowly and the desorption is only completed at around 70 K. Catenation might be a reason for these findings as proposed by Panella *et al.* This possibility will be investigated at the end of Section 5.6. The simulated spectra for both materials are similar as expected from their structures. Starting with a very high initial desorption rate, this is dropping quickly but the decline is slowed down around 22 K. The final desorption temperature is similar for both materials in the simulation, meaning that the last desorbed molecules (the most strongly interacting ones) are adsorbed with a similar strength. This is supported by the fact that both materials show an initial adsorption at a similar pressure in the isotherms at 20 K corresponding to hydrogen adsorption in the corners of the framework as illustrated in Figure 5-6.

Molecular simulation provides additional insight into molecular level phenomena, for example giving information about the location of the molecules inside the framework. As an example, desorption processes in IRMOF-1 are discussed in more detail. Initially, hydrogen molecules are located around the linkers and in the corners of the framework. The hydrogen molecules around the linker and in the corners of the small pores which are not strongly

interacting with the framework are desorbed first, resulting in a high initial desorption rate in the simulation. The desorption of molecules near the zinc-oxide corners, surrounded by three benzene rings in the big pores of the materials, which are the most attractive sites, correspond to the slow decline in the simulation. The density distribution in Figure 5-8 visualises the positions of hydrogen molecules over a range of configurations at 23 K, a temperature where the desorption rate is decreasing more slowly than at the beginning of the simulation, showing that the corners in the big pores are the most attractive positions.

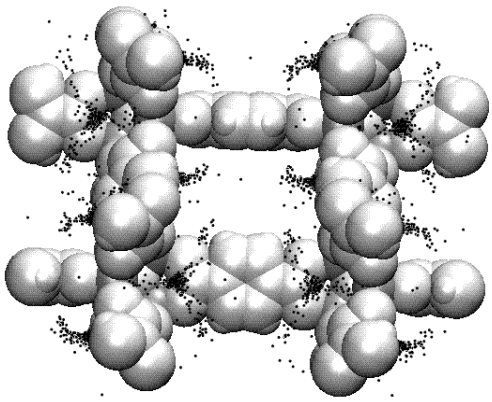

Figure 5-8 Density distributions of hydrogen in IMROF-1 (half a unit cell shown) at 23 K; framework atoms are white. The black dots represent the centres of hydrogen molecules.

The strength of the interaction of hydrogen with the IRMOF-1 framework is therefore not determined by the pore sizes as suggested by Panella *et al.* (2008) but by the orientation of the linker which provides a different explanation of the two features of the experimental desorption spectrum of IRMOF-1: the first high desorption around 20 K is caused by the desorption of the more weakly interacting molecules around the linkers as well as in the smaller pores and the peak around 40 K corresponds to the desorption of the more strongly interacting molecules in the corners in the big pores.

For MIL-53-Al, in the experiment as well as in the simulation a single peak is observed. The peak in the simulation is much narrower than in the experiment which might be due to the fixed framework. The open framework provides the highest pore volume but upon desorption a flexible structure can provide higher interaction energies through adaptation leading to a slower desorption.

5.6 Influence of framework modifications

In order to investigate which factors influence the spectra, several further adsorption and desorption simulations were done. MIL-53-Al and MIL-53-Cr are two isostructural materials that only vary in the metal. Each metal interacts with a different strength with the hydrogen which is reflected in the potential parameters (Table 4-2), but these materials also differ in their molecular weight (Table 5-2). The isoreticular MOFs vary in the linker but have the same zinc-oxide corner leading to the same topology. They are used here to investigate the influence of the linker length leading to variations in the pore size and the influence of chemical modifications of the linker in materials with similar pore sizes. Finally, catenated frameworks are compared with their uncatenated counterparts to study the effect of the catenation.

Since the pressure has an influence on the starting configuration as well as the desorption, two simulations were performed for each structure: One where the loading corresponds to the loading reported by Panella *et al.* (2008) and another at a higher pressure, corresponding to a higher initial loading, to capture additional features in the desorption spectrum.

5.6.1 Influence of the metal

The influence of the metal on low temperature adsorption and the thermal desorption spectra can be investigated for MIL-53. In addition to MIL-53-Al, MIL-53-Cr, a chromium version of the material has been reported by Serre *et al.* (2002). The isotherms for MIL-53-Al and MIL-53-Cr at 20 K presented in Figure 5-9 have a similar shape. MIL-53-Al adsorbs already at lower pressure than the MIL-53-Cr due to the stronger interaction of the aluminium with the hydrogen reflected in the potential parameters (Table 4-2). At high pressure both structures adsorb the same amount of molecules per unit cell (16) and the difference in the isotherm is due to the difference in the molecular weight of the metal.

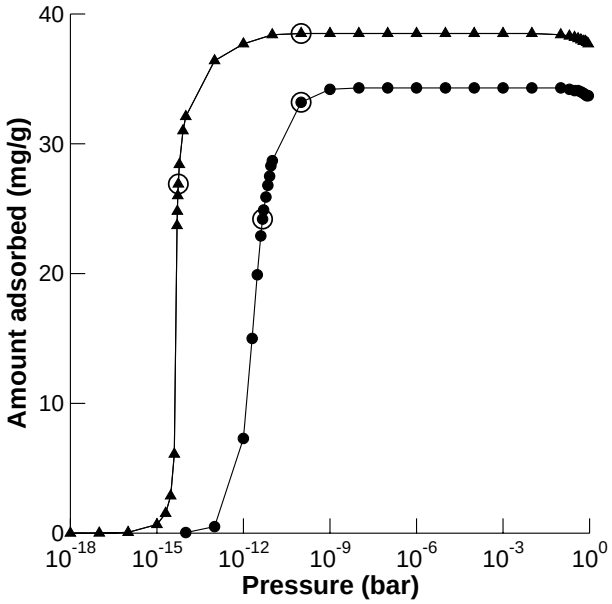

Figure 5-9 Simulated hydrogen adsorption at 20 K on MIL-53-Al (▲) and MIL-53-Cr (●). Lines are drawn to guide the eye. Starting configurations are circled.

For the desorption spectra in Figure 5-10 a), the starting loadings were fixed to 11.2 molecules/uc. This corresponds to the loading used by Panella *et al.* (2008). The corresponding pressures were $4.6 \cdot 10^{-12}$ bar for MIL-53-Cr and $5.5 \cdot 10^{-15}$ bar for MIL-53-Al. The isotherms around this loading are steep and the initial desorption rate high. For MIL-53-Al, the isotherm is steeper and the initial desorption rate higher. The molecules are all desorbed at a lower temperature than in MIL-53-Cr which compares to a smaller pressure difference between the pressure of initial adsorption in the isotherm and the starting pressure for the desorption.

The desorption spectra in Figure 5-10 b) were calculated using a higher pressure of $1 \cdot 10^{-10}$ bar. At this pressure, both frameworks have nearly reached the highest loading possible and the initial loadings were 15.5 molecules/uc for MIL-53-Cr and 16.0 molecules/uc for MIL-53-Al. Both desorption spectra exhibit a single peak corresponding to the single step in the isotherm. The desorption peak for MIL-53-Al is higher and narrower than for the Cr material which correlates with the steeper isotherm. Contrary to the findings at equal loading, at equal pressure, the MIL-53-Al framework desorbs at higher temperatures. The isotherms provide an explanation for this phenomenon. The starting configuration is on the plateau of the isotherm for MIL-53-Al and not as close to the step as in MIL-53-Cr. Choosing the same starting pressure for both structures means that

the desorption of hydrogen in the Al framework finishes at higher temperature since the isotherm shows a first uptake at lower pressures than for MIL-53-Cr.

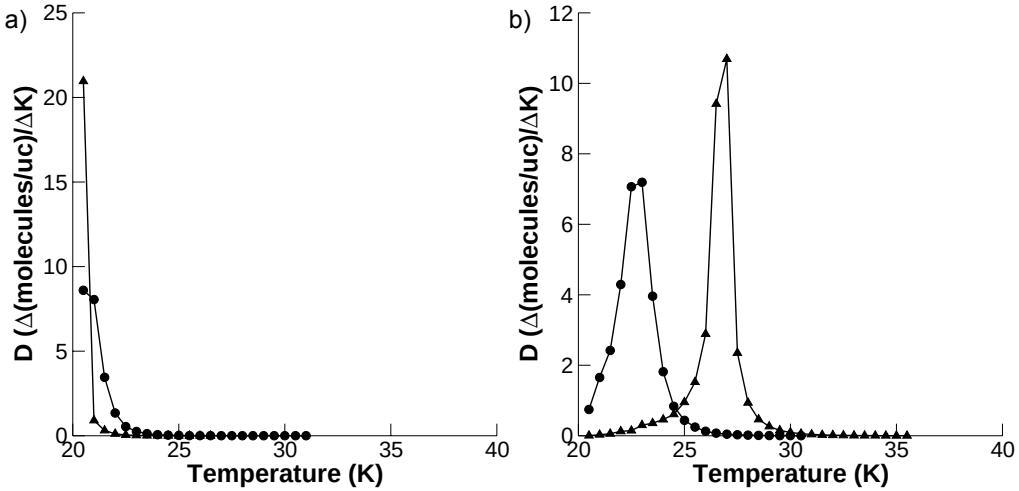

Figure 5-10 Simulated hydrogen desorption spectra for MIL-53-Al (■) and MIL-53-Cr (●) for a) a starting loading of 11.2 molecules/ uc, corresponding to $5.5 \cdot 10^{-15}$ bar (Al) and $4.6 \cdot 10^{-12}$ bar (Cr) and b) a starting pressure of $1 \cdot 10^{-10}$ bar, corresponding to 16.0 (Al) and 15.5 (Cr) molecules/uc.

Energy histograms give the energy distribution of the adsorbed molecules. Especially the interaction energy histograms of the hydrogen molecules with the framework can lead to a better understanding of the adsorption and desorption phenomena. The energy histograms for molecules adsorbed in both frameworks for the starting configuration at 20 K and $1 \cdot 10^{-10}$ bar are presented in Figure 5-11 a). Both histograms show two peaks. For MIL-53-Cr, the peaks are clearly separated, one around -6 kJ/mol and the other one around -4.5 kJ/mol. For MIL-53-Al, the peaks are closer together at -6.8 and -6.45 kJ/mol without a clear separation in-between. The energy distribution is narrower and shifted to lower energies. This increased interaction requires higher temperatures for the desorption and the narrower energy distribution leads to the high and narrow peak in the desorption spectra in Figure 5-10 b). The histogram in Figure 5-11 b) compares the hydrogen-MIL-53-Cr interaction energies at 20 K and 23 K. At the higher temperature only the lowest energy sites around -6 kJ/mol are occupied confirming that sites with a higher interaction energy are vacated first.

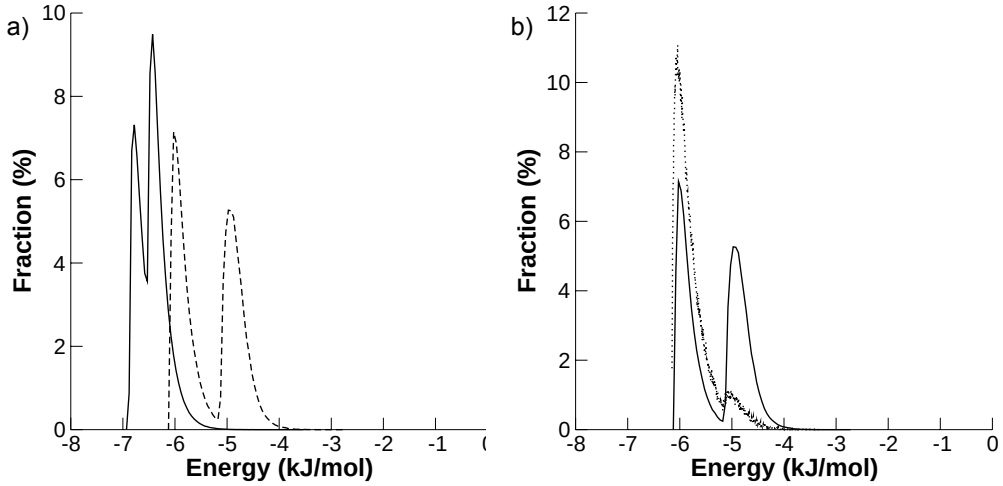

Figure 5-11 Energy histograms for hydrogen-framework interaction, $P = 1 \cdot 10^{-10}$ bar. a) 20 K, MIL-53-Al (solid line), MIL-53-Cr (dashed line); b) MIL-53-Cr, 20 K (solid line), 23 K (dotted line).

Density distributions giving the location of molecules over thousands of configurations can visualise the location for a given energy range. To find out where the molecules belonging to the peaks in the energy histogram are located within the frameworks, the density distributions for hydrogen is given in Figure 5-12. Figure 5-12 a) shows that the distinct peaks in MIL-53-Cr belong to the two types of corners of the structure and the hydrogen molecules in the corners with a smaller angle interact more strongly with the framework. For MIL-53-Al, the picture is not as clear and in the small corners molecules with energies belonging to either peak can be found depending on the distance to the aluminium atom.

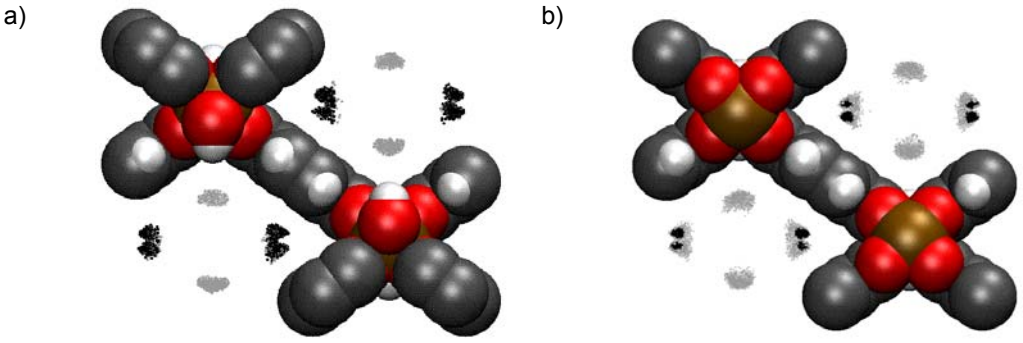

Figure 5-12 Density distribution for hydrogen showing the energy sites in a) MIL-53-Cr and b) MIL-53-Al. The dots represent the centre of the molecules in the sampled configurations. In a) energy lower (black dots) and higher (grey dots) than -5.15 kJ/mol. In b) energy lower (black dots) and higher (grey dots) than -6.55 kJ/mol.

The desorption spectra give an overall picture of the desorption over a range of temperatures. The energy histograms provide further information about the energy of the desorbing molecules, allowing the calculation of desorption curves for each peak identified in Figure 5-11 a) individually. Such desorption curves are displayed in Figure 5-13 where the variations of number of molecules per peak as function of the temperature are shown. The curves are normalised by the number of molecules in the starting configuration for each of the peaks. Desorption occurs in the order of energy of the peak for MIL-53-Cr. Although the difference between the energies of the highest energy peak for MIL-53-Al (-6.45 kJ/mol) and the lowest energy peak for MIL-53-Cr (-6 kJ/mol) are not that high, the desorption in MIL-53-Cr takes place at a lower temperature of around 23 K whereas in MIL-53-Al the desorption occurs around 27 K. Since it is the peak with the highest energy for MIL-53-Al, and the framework is still saturated, the delayed desorption could be due to interactions with other hydrogen molecules. In MIL-53-Al, the number of molecules for both peaks is changing in a similar way due to the similar energies. The hydrogen molecules in the narrower and wider corners in MIL-53-Al desorb concurrently whereas the desorption of the hydrogen molecules in the narrower corners in MIL-53-Cr takes place at higher temperature, due to a stronger interaction with the framework, than in the wider corners.

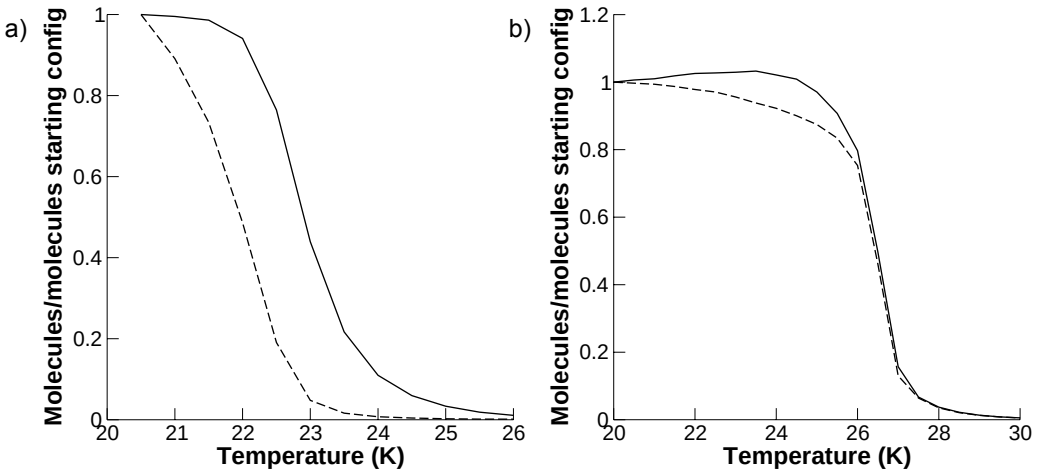

Figure 5-13 Evolution of the molecules per peak at $1 \cdot 10^{-10}$ bar in a) MIL-53-Cr, peak around -6 kJ/mol (solid line) and around -4.5 kJ/mol (dashed line) and b) MIL-53-Al, peak around -6.8 kJ/mol (solid line) and around -6.45 kJ/mol (dashed line).

5.6.2 Influence of chemical modifications of the linker

IRMOF-2 and IRMOF-7 are similar to IRMOF-1, having the same metal corner and linkers of same length. Within the linker of IRMOF-2 a bromine atom replaces a hydrogen atom on

the phenyl ring. IRMOF-7 has a further phenyl ring in the linker. The linkers are represented in Figure 5-14.

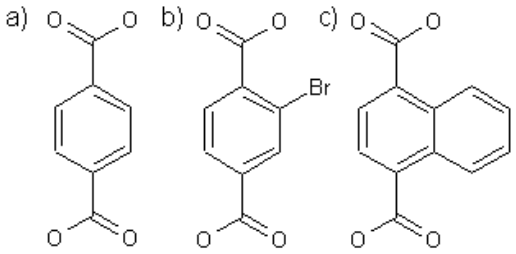

Figure 5-14 Linker for a) IRMOF-1, b) IRMOF-2 and c) IRMOF-7.

The hydrogen adsorption isotherms at 20 K for IRMOF-1, IRMOF-2 and IRMOF-7 are shown in Figure 5-15. Both IRMOF-2 and IRMOF-7 adsorb at lower pressure than IRMOF-1. The isotherm of IRMOF-1 shows two distinct steps. These steps are present in the other isotherms but much less distinctive. For IRMOF-1 and IRMOF-2, the steps occur at similar pressures, with a first strong increase in the amount adsorbed between the pressures of $1 \cdot 10^{-8}$ bar and $1 \cdot 10^{-5}$ bar and the second increase between $1 \cdot 10^{-5}$ and $1 \cdot 10^{-3}$ bar. The first step for IRMOF-7 occurs already at lower pressure between $1 \cdot 10^{-12}$ and $1 \cdot 10^{-8}$ bar and the second on between $1 \cdot 10^{-7}$ and $1 \cdot 10^{-5}$ bar.

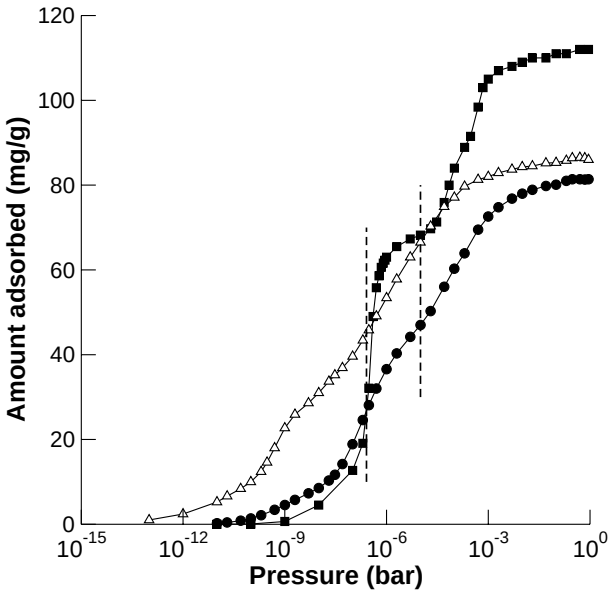

Figure 5-15 Hydrogen adsorption at 20 K for IRMOF-1 (■), IRMOF-2 (●) and IRMOF-7 (Δ). Lines are drawn to guide the eye. Dashed lines mark the pressures used for the desorption simulations.

The pressure for the desorption calculations was set to $2.56 \cdot 10^{-7}$ bar for all three simulations. The starting configurations differ in the amount adsorbed and were 77 molecules/uc for IRMOF-1, 108 molecules/uc for IRMOF-2 and 164 molecules/uc for IRMOF-7. The resulting desorption spectra are shown in Figure 5-16 a). IRMOF-1 has a very high initial desorption rate, which drops down quickly. Complete desorption is reached at 28 K. The initial desorption rate for IRMOF-2 is lower but it does not drop as quickly and molecules are desorbed up to 30.5 K. The starting desorption rate for IRMOF-7 is still lower. A peak in the spectra is found around 26 K. Starting at a higher pressure of $1 \cdot 10^{-5}$ bar, one peak is observed for IRMOF-1 and IRMOF-2 and two peaks for IRMOF-7 (Figure 5-16 b)). The same features as in Figure 5-16 a) can be found shifted by around 5 K to higher temperature.

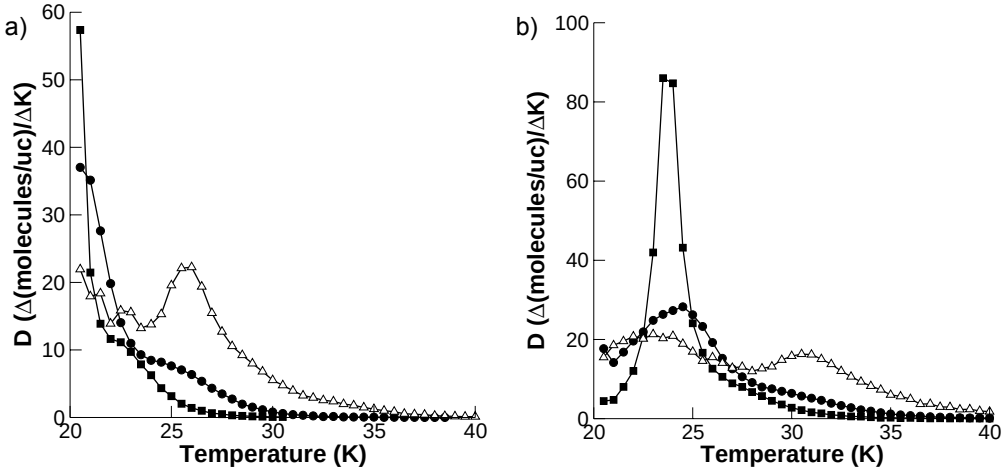

Figure 5-16 Hydrogen desorption spectra for IRMOF-1 (■), IRMOF-2 (●) and IRMOF-7 (Δ) a) starting pressure = $2.56 \cdot 10^{-7}$ bar;
b) starting pressure = $1 \cdot 10^{-5}$ bar.

The desorption occurring at high temperature in IRMOF-7 can be explained by the interaction of the hydrogen with the framework. Figure 5-17 a) shows that for IRMOF-7 the energies stretch to lower values than for IRMOF-1 and IRMOF-2. At 23 K (Figure 5-17 b)), the main energy site around -3.6 kJ/mol in IRMOF-1 and IRMOF-2 are only occupied by a small fraction whereas in IRMOF-7 the site is still of main importance. Only at higher temperatures corresponding to the peak in Figure 5-16 a) are the molecules desorbed.

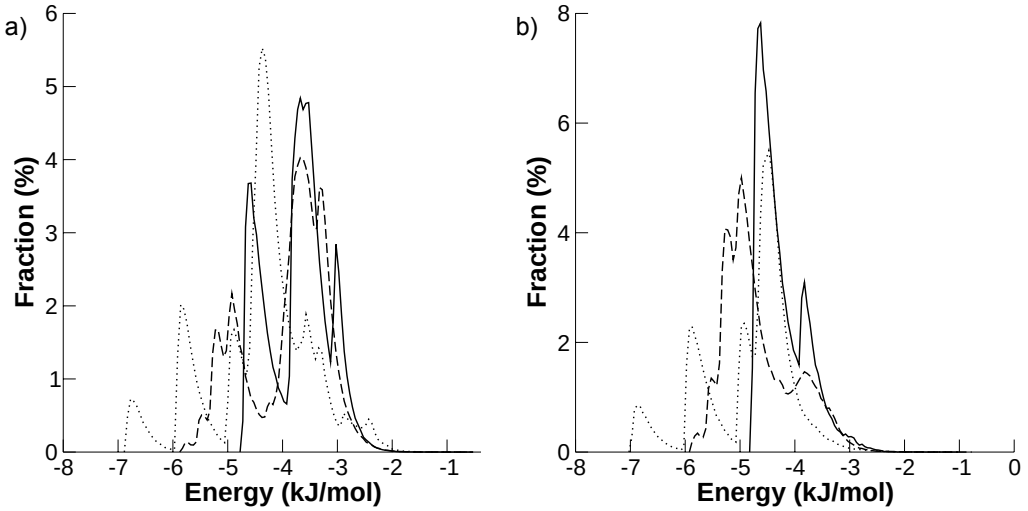

Figure 5-17 Energy histograms for IRMOF-1 (solid line), IRMOF-2 (dashed line) and IRMOF-7 (dotted line) for P = $2.56 \cdot 10^{-7}$ bar. a) 20 K; b) 23 K.

The density distribution in Figure 5-18 gives the location of the energy sites corresponding to the peaks for IRMOF-1 in Figure 5-17. The zinc-oxide clusters are very attractive for the hydrogen with the corner providing the highest interaction. The linker is less attractive and only the centre of the phenyl ring is occupied at this condition.

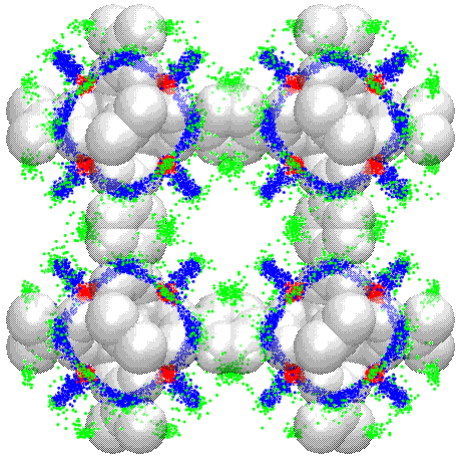

Figure 5-18 Density distributions of hydrogen in IMROF-1; lowest energy (red), medium (blue) and high (green); framework atoms are white and transparent.

In Figure 5-19, the density distributions for the two lowest energy sites corresponding to the two lowest energy peaks in IRMOF-7 are shown. The hydrogen molecules with the lowest energy interact with three additional phenyl rings. The second lowest peak contains molecules that interact with one additional phenyl ring and close to the zinc-oxide centre.

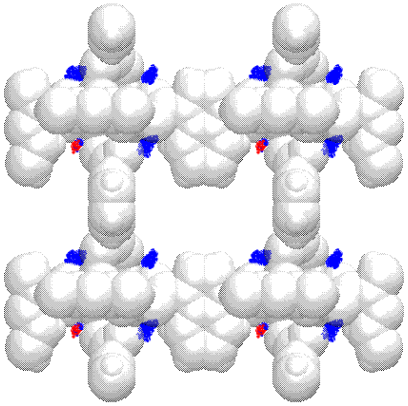

Figure 5-19 Density distribution for hydrogen in low energy sites in IRMOF-7. Lowest energy peak (red) and second lowest peak (blue), framework atoms are white and transparent for better visibility.

5.6.3 Influence of the linker length

IRMOF-8 and IRMOF-10 both have linker molecules consisting of two phenyl rings, in IRMOF-8 these are connected together in the naphthalene-2, 6-dicarboxylate linker whereas in IRMOF-10 these are separated by a bond in the 4, 4'-biphenyldicarboxylate linker. In IRMOF-14, the amount of rings is doubled in the pyrene-2, 7-dicarboxylate linker but the linker length is similar to IRMOF-10. The three linkers are shown in Figure 5-20 together with the linker of IRMOF-1.

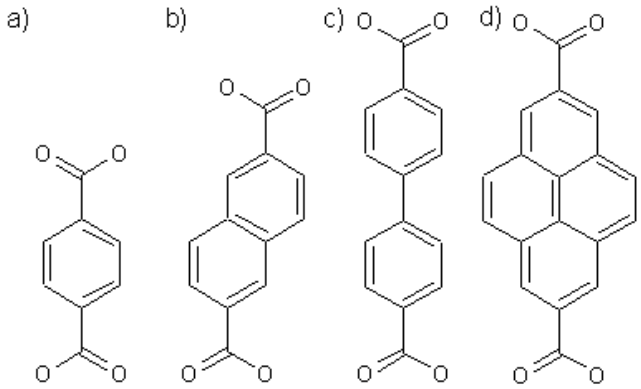

Figure 5-20 Linkers for a) IRMOF-1, b) IRMOF-8, c) IRMOF-10, and d) IRMOF-14.

The isotherms at 20 K for IRMOF-1, -8, -10 and -14 are presented in Figure 5-21. They show three different stages for all four materials: First, all isotherms show an initial uptake at about the same pressure, $1 \cdot 10^{-8}$ bar. At low pressures up to $1 \cdot 10^{-5}$ bar, the uptake in IRMOF-14 is highest. At medium pressures, from $1 \cdot 10^{-5}$ to $1 \cdot 10^{-2}$ bar this picture reverses and IRMOF-14 shows the lowest uptake. In this pressure range, the isotherms are very close

together. At pressures above $1 \cdot 10^{-2}$ bar, IRMOF-10 shows the highest uptake, followed by IRMOF-14 and IRMOF-1 has the lowest capacity. The high free volume and low crystal density of IRMOF-10 (Table 5-2) explain the high capacity for this material. The free volume of IRMOF-14 is slightly higher, but the higher crystal density reduces the capacity. For IRMOF-8 and IRMOF-1, the free volume is decreasing and the crystal density increasing, leading to the low capacities compared to the materials with the longer linkers.

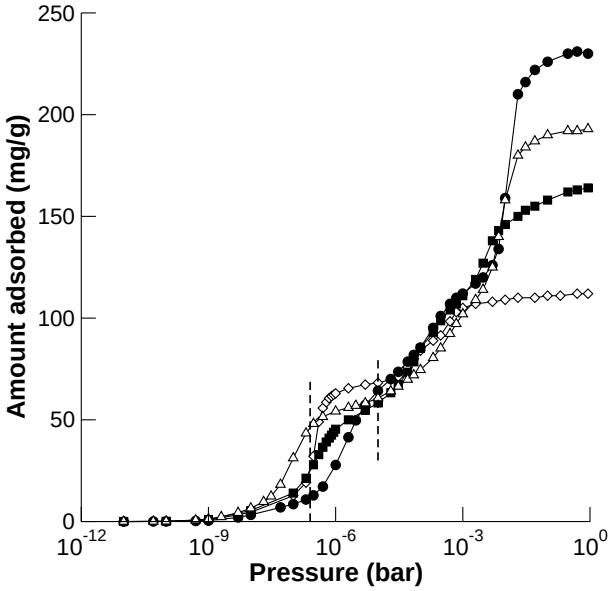

Figure 5-21 Hydrogen adsorption at 20 K for IRMOF-1 (◊), IRMOF-8 (■), IRMOF-10 (●) and IRMOF-14 (Δ). Lines are drawn to guide the eye. Dashed lines mark the pressures for the desorption.

The desorption spectra in Figure 5-22 a) were calculated at a pressure of $2.5 \cdot 10^{-7}$ bar corresponding to initial loadings of 91 molecules/uc for IRMOF-8, 48 molecules/uc for IRMOF-10 and 211 molecules/uc for IRMOF-14, respectively. The starting configuration lies on the steep increase of the isotherm for IRMOF-14, indicating that a small change of the conditions has a strong effect. This leads to the high initial desorption rates. By contrast, with the low initial loading in IRMOF-8, most of the molecules occupy very favourable positions and the initial desorption rate is low compared to the other materials. Above 23 K, the desorption spectra become very similar and the energy distributions at 23 K (Figure 5-23 b)) do not differ much. The molecules in the positions of higher energy that were present at 20 K (Figure 5-23 a)) have desorbed and a very high fraction of the molecules occupies the low energy sites in the corner of the structures that are similar in all three materials.

The desorption spectra for the higher pressure of $1 \cdot 10^{-5}$ bar are shown in Figure 5-22 b). The starting configurations lie after the first steep increase on all isotherms. The initial loadings increased considerably for IRMOF-8 and IRMOF-10 to 215 and 256 molecules/uc respectively. For IRMOF-14, the initial loading increased to 277 molecules/uc. All desorption spectra show a single peak with a slower decline of the desorption rate as discussed before for IRMOF-1. The order of appearance of the peaks with increasing temperature is opposite to the appearance of the steep increase with increasing pressure in the isotherm, since the hydrogen molecules adsorbing more strongly are adsorbed first and desorbed last. The more ring structures are located close together, the more attractive sites are close to the linker, resulting in the shift of the peak to the higher desorption temperature. The initial desorption rate for IRMOF-10 is not as low as for the other two materials since no extended plateau is present in the isotherm.

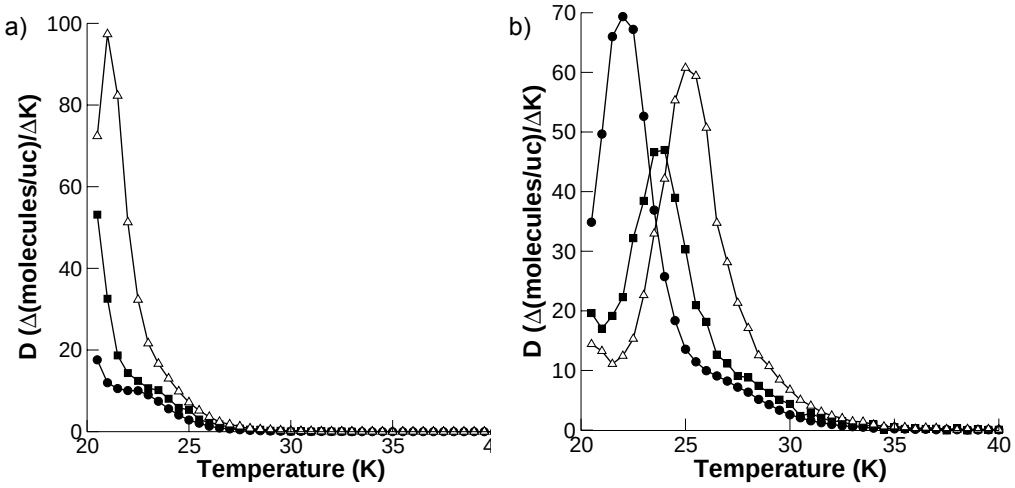

Figure 5-22 Hydrogen desorption spectra for IRMOF-8 (■), IRMOF-10 (●) and IRMOF-14 (Δ) a) starting pressure = $2.5 \cdot 10^{-7}$ bar, b) starting pressure = $1 \cdot 10^{-5}$ bar.

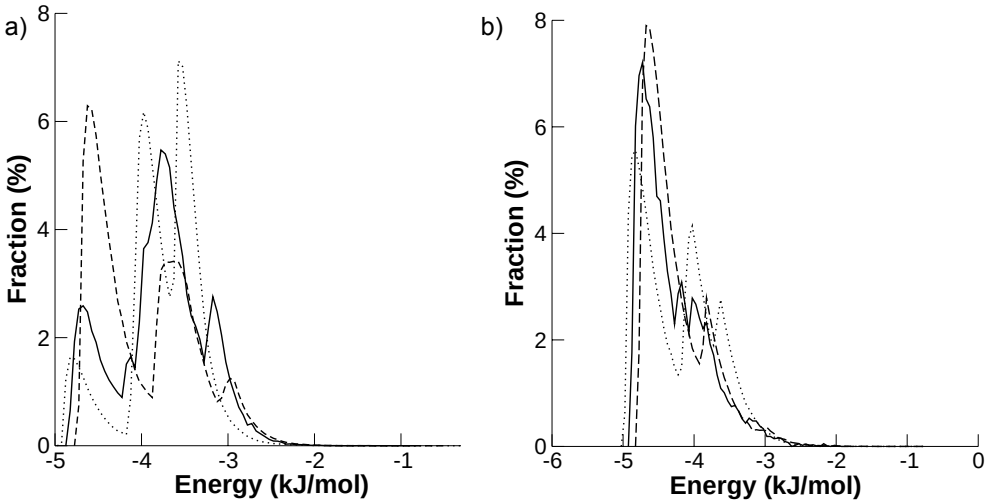

Figure 5-23 Energy histograms for IRMOF-8 (solid line), IRMOF-10 (dashed line) and IRMOF-14 (dotted line) at $2.5 \cdot 10^{-7}$ bar at a) 20 K and b) 23 K.

5.6.4 Influence of catenation

For both IRMOF-10 and IRMOF-14, catenated versions of the framework exist (Figure 2-6) which are called IRMOF-9 (catenated version of IRMOF-10) and IRMOF-13 (catenated version of IRMOF-14). Catenation results in smaller pores and more adsorption sites per unit cell, which is favourable for hydrogen adsorption but catenation also increases the framework density and decreases the pore volume, which has a negative impact on the gravimetric hydrogen uptake.

Figure 5-24 shows that at low pressure the adsorption in the catenated frameworks is increased compared to the non-catenated ones. At high pressure, the trend is reversed due to the lower pore volume and higher density of the samples.

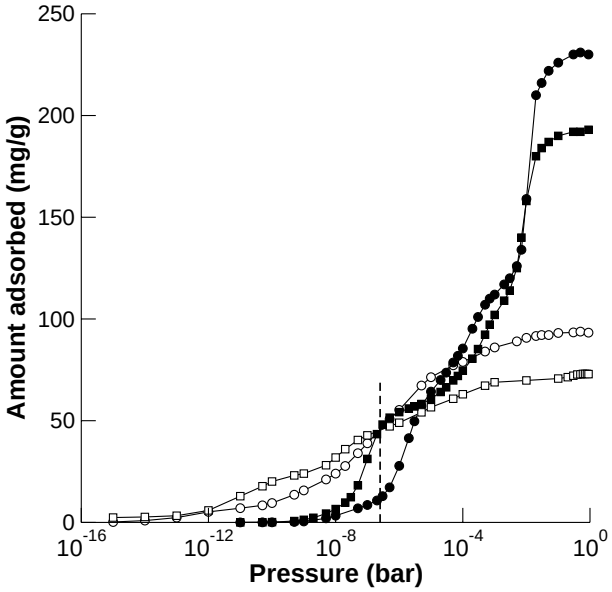

Figure 5-24 Hydrogen adsorption at 20 K for IRMOF-9 (○), IRMOF-10 (●), IRMOF-13 (□) and IRMOF-14 (■).Lines are drawn to guide the eye. Dashed line marks the pressure for the desorption.

The desorption spectra in Figure 5-25 were calculated with a pressure of $2.5 \cdot 10^{-7}$ bar. The starting loadings were 367 molecules/uc for IRMOF-9, 48 molecules/uc for IRMOF-10, 415 molecules/uc for IRMOF-13 and 211 molecules/uc for IRMOF-14. As expected from the isotherms (Figure 5-24), the catenated materials show a higher uptake. IRMOF-9 shows a very high initial desorption rate that drops with temperature up to 29.5 K. Then the desorption rate is nearly constant for 5 K and decreases again afterwards until the final desorption at 40 K. IRMOF-13 shows two peaks in the spectrum: one at 22.5 K and a broad one around 28 K. The desorption rate at high temperature is constant at a low level.

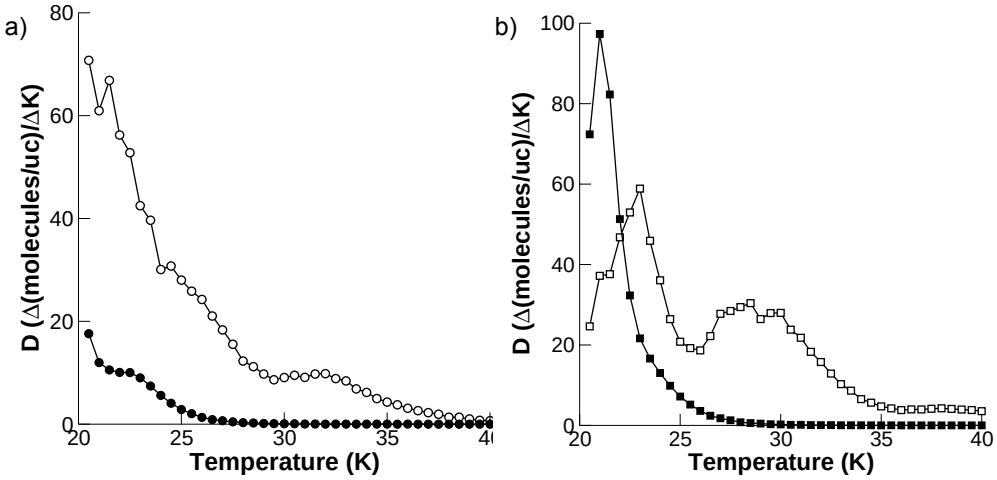

Figure 5-25 Hydrogen desorption spectra for a catenated framework and its non-catenated counterpart a) IRMOF-9 (○) and IRMOF-10 (●), b) IRMOF-13 (□) and IRMOF-14 (■), starting pressure of $2.5 \cdot 10^{-7}$ bar.

The energy histogram for IRMOF-9 in Figure 5-26 a) indicates that the molecules that occupy the low energy positions in IRMOF-10 are distributed over a broader low energy range down to -7.15 kJ/mol.

The energy histogram for IRMOF-13 in Figure 5-26 b) shows that a smaller fraction of molecules have an interaction energy between -3 and -4.1 kJ/mol than in IRMOF-14. The low energy peak of IRMOF-14 is extended to lower energies and an additional very low energy site exists for IRMOF-13. The desorption peaks can be therefore explained with these energy sites. The first peak in the desorption spectrum for IRMOF-13 corresponds to the desorption of molecules with interaction energies around -3.8 kJ/mol. For IRMOF-14, the higher initial desorption rate for temperatures up to 22 K is due to the molecules with an interaction energy of around -3.5 kJ/mol.

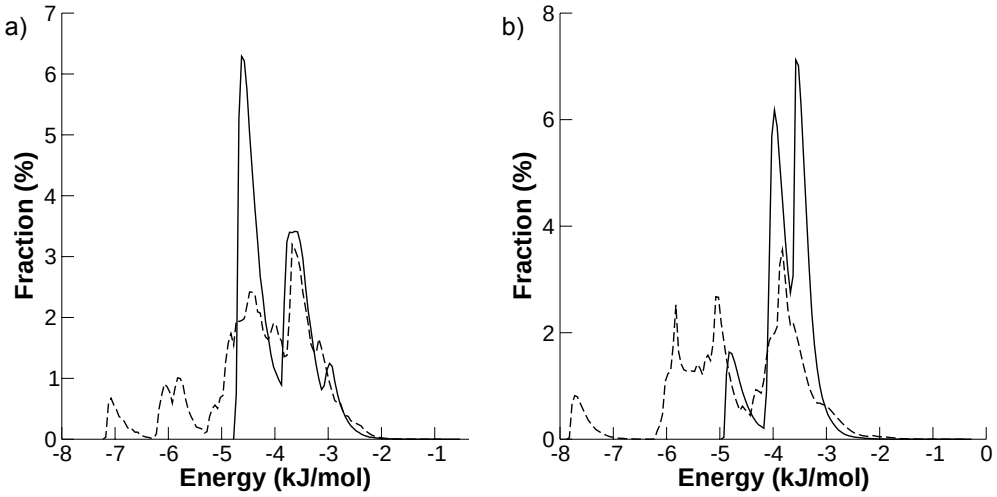

Figure 5-26 Energy histogram at 20 K and $2.5 \cdot 10^{-7}$ bar. a) IRMOF-9 (dashed line) and IRMOF-10 (solid line); b) IRMOF-13 (dashed line) and IRMOF-14 (solid line).

Comparing the energy histograms at different temperatures (Figure 5-27) gives that the broad peak in the desorption spectrum for IRMOF-13 corresponds to the interaction energies between -5 and -6 kJ/mol and the final extended peak to the molecules occupying the very low energy positions of less than -6 kJ/mol.

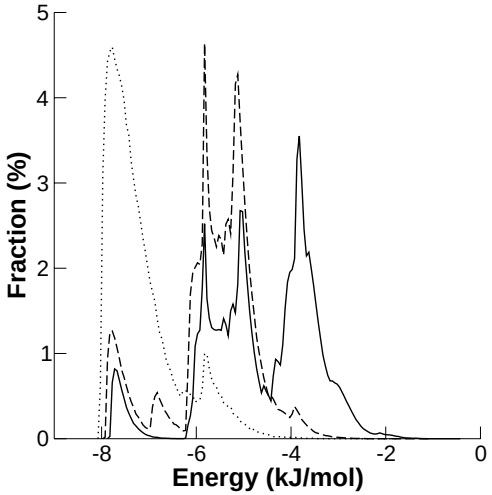

Figure 5-27 Energy histogram for hydrogen in IRMOF-13 at P = $2.5 \cdot 10^{-7}$ bar at 20 K (solid line), 26 K (dashed line) and 36 K (dotted line).

Catenation results in the creation of low energy sites, consequently extending the desorption to higher temperatures. The spectrum for IRMOF-9 resembles the experimental spectra for IRMOF-8 indicating that the experimental sample used by Panella *et al.* (2008) was indeed a catenated structure.

5.7 Conclusions

The simulation of adsorption of hydrogen in MOFs and temperature controlled desorption was investigated systematically. The isotherms at 77 K were calculated and showed good agreement with the experimental isotherms for IRMOF-1 and CuBTC. For IRMOF-8, the simulated adsorption at high pressures was higher than observed in the experiment, indicating that the sample was catenated. For MIL-53, the simulated adsorption exceeded the experimental one at low pressures. This might be due to neglecting the framework flexibility.

Lowering the temperature to 20 K, the isotherms showed steps at low pressures which can be attributed to adsorption sites and pore filling respectively. The simulated temperature controlled desorption gave spectra with similar features than in the experiment but at much lower temperatures. High desorption rates were found to correspond to steep increases in the adsorption isotherms and therefore the peaks in the spectra correspond to steps in the isotherm.

Contrary to the findings by Panella *et al.* (2008), the simulations showed no clear relation between the desorption temperature and the pore size. Instead, the desorption temperature related to the interaction between the molecules and the framework which is not necessarily correlated to the pore size. Since the strength is higher in smaller pores such as MIL-53 or in the smaller cavities of CuBTC, the desorption temperature was generally higher but modifications of the frameworks showed that the pore size is not the main factor. In IRMOF-1, the desorption in the smaller pores occured at lower temperatures than in the larger pores due to favourable sites in the corners of the big pores. The simulations showed that in frameworks with different linker lengths the desorption temperature is similar, in frameworks with modifications in the metal or the linker, the desorption temperature differed. For further investigations, a hydrogen potential incorporating the quantum effect, the electrostatic interactions and the polarisability should be developed and applied.

6 Mesoporous silica materials

Mesoporous silica materials as adsorbents are considered in this chapter. In order to simulate the adsorption on a mesoporous silica material such as MCM-41, a model capturing the characteristics of the material is needed. Due to the amorphous structure at the atomic level, models are more difficult to relate to experiments than in the case of crystalline materials. The models do not provide an exact representation of the synthesised material but rather represent the material in a statistical sense. Several approaches have been used to model mesoporous silica materials on different levels, from the equilibrium phase to a single pore, some of which are presented in Chapter 2. In the first part of this chapter, a new methodology to obtain atomistic models is described that combines the strengths of two simulation techniques that have so far been used independently, the equilibrium Monte Carlo and kinetic Monte Carlo methods. In Section 6.1.1 and 6.1.2, these two methods are described respectively. The combined method is explained in 6.1.3 and results are given in the Sections 6.1.4 and 6.1.5.

Furthermore, the pore walls of atomistic models in the simulation can be modified with surface groups in the simulation to represent mesoporous silica materials with organic functinalization. These surface groups alter the surface chemistry and influence the adsorption properties (Section 2.2.2). In the second part of this chapter, mesoporous silica materials modified with organic surface groups are investigated for the adsorption of carbon dioxide with the details of the simulations given in Section 6.2.1. The influence of halo-phenyl surface groups on the adsorption of carbon dioxide is studied in 6.2.2 and the effect on the selectivity for carbon dioxide from an equimolar carbon dioxide-methane mixture of one iodo and two amino groups are studied in 6.2.3.

6.1 Modelling of the material

The two methods, on which the new approach is based, are the equilibrium Monte Carlo (eMC) and the kinetic Monte Carlo method (kMC). By using the eMC simulation, the equilibrium phase behaviour can be studied (Siperstein and Gubbins (2003), Patti *et al.* (2007)). The models used are coarse grained, i.e. the inorganic oxide is represented by one or two sites and the surfactant is represented by a small number of sites. Furthermore, the simulation is based on a lattice, restricting the position of the sites. The complexity is reduced in this way, in order to make the simulations computationally feasible.

In contrast to the eMC simulation that captures properties on the mesoscale, the kinetic Monte Carlo method developed by Schumacher *et al.* (2006b) is used to model the mesoporous silicas on the atomistic scale. The silica matrix is created around a representation of the micelle, mimicking the experimental synthesis. The templating micelle in the original method is represented by a cylinder which can be changed to a hexagonal rod with rounded edges during the aggregation step. The ideal geometries used in this approach simplify the structure for the micelle and have a smoother surface than micelles in the experimental synthesis. In the approach presented here, a more heterogeneous model is applied, aiming for a more realistic representation of the micelle. The coarse-grained micelles obtained from the eMC simulations are an ideal starting point for the creation of the atomistic models and therefore these two methods have been combined here.

In the combined approach, equilibrium Monte Carlo (eMC) simulations based on the coarse grained model are used to simulate the formation of the periodic mesophase and the kinetic Monte Carlo (kMC) method simulates the condensation reaction around a micelle with a shape extracted from the eMC simulation, in order to obtain the periodic mesoporous materials. The initial mixture is represented in the eMC simulation by a random distribution of surfactant, solvent and silica precursors. After the system reaches equilibrium, the surfactant forms a regular hexagonal array of micelles. Once the mesophase has been obtained, a single micelle is extracted to build around it the silica pore wall using the kMC scheme developed by Schumacher *et al.* (2006b). These atomistic representations of the material are then used for adsorption studies using grand canonical Monte Carlo simulation. The two approaches and their combination are presented in more detail in the following sections.

6.1.1 Equilibrium Monte Carlo simulations

The eMC simulations in the NVT ensemble were performed by Alessandro Patti at the University Rovira i Virgili in Tarragona, under the supervision of Flor Siperstein, to model the aggregation behaviour of surfactant/silica/solvent systems. In general, the formation of ordered phases depends on the surfactant concentration and on the nature of the precursor involved. Both factors have been analyzed by Patti *et al.* (2006), where the appearance of hexagonally ordered micellar rods was observed at surfactant concentrations between 50 % and 70 % by volume when a pure silica precursor was used. The compositions for the systems used in this study were chosen to ensure that a single, ordered hexagonal phase was obtained. The size of the lattice box was set to $40 \times 40 \times 40$ for the linear surfactant and

50 × 50 × 50 for the longer surfactant with the branched head. Periodic boundary conditions were applied.

The coarse-grain lattice model used in these simulations represents the most important features of an amphiphilic system with a surfactant, an inorganic precursor and a solvent. In this model, the surfactant (H_mT_n) is composed of m hydrophilic segments (called "heads", H) and n hydrophobic segments (called "tails", T). The surfactant is represented by a flexible chain of connected sites in the 3D-lattice. The inorganic precursor is modelled by two connected segments, I_2, whose individual interaction parameters are tuned to simulate a complete miscibility with the solvent (Patti *et al.* (2007)). Equivalent results can be obtained from partially miscible systems (Patti *et al.* (2006)), which are not considered here. Those lattice sites left available by the surfactant and the inorganic precursor are then filled by the solvent beads, each of them occupying a single site. Surfactant heads are completely soluble in the solvent.

In the model used, all interactions are represented by a single interaction parameter for each pair of species, which is referred to as the global interchange energy, ω_{ij}, between types of sites i and j. It is given by

$$\omega_{ij} = \varepsilon_{ij} - \frac{1}{2}\left(\varepsilon_{ii} + \varepsilon_{jj}\right) \tag{6.1}$$

with $i \neq j$ and ε_{ij} being the individual interaction energies of different types of sites with values summarised in Table 6-1.

Table 6-1 Individual interaction parameters (ε_{ij}) between surfactant (*T, H*), inorganic oxide (*I*) and solvent (*S*) in units of k_BT.

	I	*H*	*T*	*S*
I	0			
H	-2	0		
T	0	0	-2	
S	0	0	0	0

It is computationally convenient to define all individual interactions with the solvent, ε_{is}, as zero, and calculate the individual interaction parameters ε_{ij} for the rest of the pairs using the selected global interchange energies, therefore, in this work the solvent is not modelled explicitly. The surfactant - solvent interchange energies used are the same as those proposed in previous works by other researchers (Larson *et al.* (1985), Mackie *et al.* (1997)).

The dimensionless temperature is defined using the head-tail interchange energy: $T^* = k_B T/\omega_{HT}$, where k_B is the Boltzmann constant, T is the absolute temperature and ω_{HT} is the surfactant head-tail interaction energy. The simulations with a linear surfactant were run at $T^* = 8.0$ for $90 \cdot 10^9$ MC steps and with a branched surfactant at $T^* = 12.0$ for $80 \cdot 10^9$ MC steps. The silica-precursor and surfactant chains were moved by reptation, and partial or complete regrowth using configurational bias moves. The type of moves were randomly selected, using an 80 % probability for reptation, 10 % for partial regrowth, and 10 % complete regrowth. This combination was chosen after analyzing the evolution of dilute and concentrated systems for several possible combinations of MC moves.

6.1.2 Kinetic Monte Carlo simulation

The eMC simulation gives information about average properties in an equilibrated system, whereas in the kMC simulation, a random reaction pathway is generated leading to a metastable state. The kMC simulation samples only the part of all possible configurations that lie near the reaction pathway and is therefore not ergodic. Kinetic Monte Carlo simulations are used in this work to simulate the condensation reaction around the surfactant micelle as described by Schumacher *et al.* (2006b). This off-lattice simulation method follows the pathway of a silica sol-gel process with each simulation step corresponding to a reaction step. Trial configurations are created using the following Monte Carlo moves: formation of a siloxane bridge, hydrolysis of a siloxane bridge, swapping of a silanol group and a siloxane bridge, swapping of two siloxane bridges between neighbouring silicon atoms or the random displacement of all atoms. The type of move is randomly selected with equal probability for each type. The energy of the resulting configuration is minimized and the change in energy to the previous configuration calculated to obtain the acceptance probability (Chapter 3). The energy of the formation of the siloxane bridge from two silanol groups was set to -13.4 kJ/mol (Catlow *et al.* (1997)).

The kMC simulation starts with a model for the micelle and a random distribution of silica monomers. The monomers are attracted by the micelle and the condensation reaction starts. Once a layer around the micelle is formed the aggregation of the micelles is initiated and siloxane bridges are formed between molecules surrounding neighbouring micelles. When no further net reaction occurs, the calcination step is initiated by increasing the network temperature and removing the micelle. Up to this stage the reaction has been reversible, now the hydrolysis move is disabled, reflecting the lack of water molecules (which are not modelled explicitly) at the high temperature. The swapping of siloxane bridges is still

possible. For the final structure the temperature is decreased stepwise to ambient temperature. Figure 6-1 gives a schematic representation of kMC reaction steps.

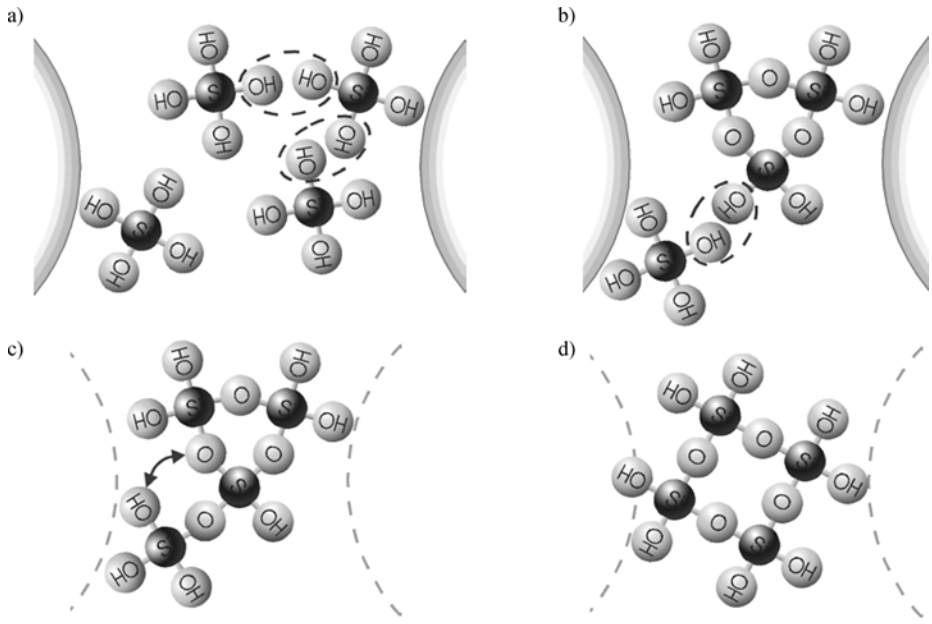

Figure 6-1 Schematic representation of the steps in a KMC simulation. (a) Silicic acid monomers near micelles. Dashed circles show possible condensation reactions (b) Further condensation and formation of rings. Bridging oxygen atoms can be hydrolyzed. (c) Calcination: the arrow indicates switching of a siloxane bridge to relax the ring. Dashed lines show the former positions of the templates. (d) Refined structure after calcination. Figure reproduced with permission from Schumacher and Seaton (2005). Copyright Springer Science and Business Media.

Covalent bonds between oxygen and silicon atoms are modelled as harmonic spring functions (Tu and Tersoff (2000)):

$$U_{bond} = \frac{1}{2}\sum_{i} K_{stretch}\left(r_i - r_{i,0}\right)^2 + \frac{1}{2}\sum_{a}\sum_{i,j} K_{bend,a}\left(\cos\theta_{ij} - \cos\theta_{a,0}\right)^2 \tag{6.2}$$

The first term for the bond stretching accounts for all Si-O-bonds in the simulation cell and the second sum runs over all bond angles between two bonds i and j of the same atom a. The equilibrium Si-O-bond length r_0 is 0.16 nm and the corresponding spring constant $K_{stretch}/k_B$ is $31.33 \cdot 10^6$ K/nm^2. The equilibrium bond angles for the oxygen atoms $\theta_{O,0}$ and silicon atoms $\theta_{Si,0}$ are 180° and 109.47° and the constants $K_{bend,O}/k_B$ and $K_{bend,Si}/k_B$ are 50131 K and 8703 K, respectively. Between two non-bonded atoms that are not bound to the same atom and are within the cut-off radius r_c of 0.28 nm, a soft repulsive potential is applied, which is a quadratic approximation to the repulsive part of the Lennard-Jones potential of an oxygen atom and is given by

$$U_{rep} = \frac{1}{2} \sum_{\substack{i \neq j \\ r_{ij} < r_c}} K_{rep} \left(r_c - r_{ab} \right)^4 \tag{6.3}$$

where the constant k_{rep}/k_B has the value $541.48 \cdot 10^6$ K/nm^4 (Schumacher *et al.* (2006b)). Whereas the silicon and oxygen atoms are represented explicitly, the hydrogen atoms are not, therefore the simulation does not distinguish between protonated and deprotonated forms of silanol groups. The influence of the pH of the synthesis solution can be incorporated in the reaction rates. Schumacher *et al.* (2006b) showed that the kMC simulations show good agreement with experimentally observed kinetics for an acidic system if the reaction probability is the same for all hydroxyl groups.

6.1.3 Combination of the simulation methods

The combination of the methods presented above aims to join the strength of the two simulations to build a new method that gives realistic models for MCM-41 on the atomic as well as the mesoscale and might be applied to a wide range of mesoporous silica materials synthesised by different surfactants. At first, the eMC method is used to obtain an ordered phase. Figure 6-2 gives an example for a hexagonally ordered phase obtained in the eMC simulation for a H_4T_4/I_2/solvent system, along with a cylindrical micelle extracted from that mesophase. From the final configuration in Figure 6-2 (a) a cylindrical micelle, constituting the inner organic core (composed of the surfactants) of its corresponding mesopore, is randomly selected. This selection is made by defining an axis connecting the centre of a given cross section of the cylindrical micelle with another cross section belonging to the same micelle. All the surfactant chains between these cross sections are included in the cylindrical micelle of which a part (Figure 6-2 (b)) is chosen. The final model of the micelle for the kMC simulation is either based on a cross-section (using a single cut through the micelle not allowing the potential to change over the length of the micelle) or a 3D model of the micelle.

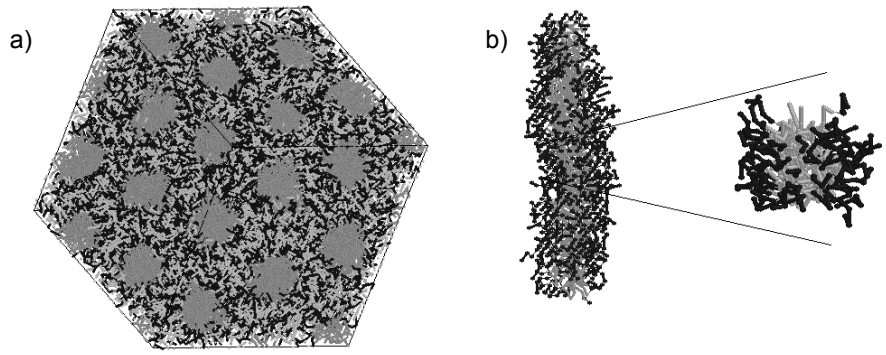

Figure 6-2 (a) Final configuration for a H_4T_4/I_2/solvent system, simulated for 90×10^9 MC steps in a 40×40×40 lattice box and (b) a cylindrical micelle extracted from this final configuration, where the segment used as template in the kMC simulation is indicated. The surfactant tails are represented by dark grey segments, the surfactant heads by black segments, and the inorganic precursor by light grey segments. Volume fractions: H_4T_4 52%, I_2 32%. (Prosenjak *et al.* (2007)).

The model of the micelle obtained from the eMC simulation is represented by a continuous potential function in the kMC simulation. To compare the results with the models obtained from the original kMC methods, the same potential function is used as presented by Schumacher (2006): The potential between the oxygen atoms and the micelle depends on the distance between an oxygen atom and the edge of the micelle and is attractive to oxygen atoms near the micelle and repulsive if they penetrate into the micelle. The potential function for the interaction between the micelle (*Mic*) and the oxygen atoms (*O*) is represented by two smoothly jointed quadratic functions. The shape of the curve is similar to a Lennard-Jones potential but reaches zero at a defined distance from the micelle surface beyond which no interaction takes place. The interaction potential $U_{MicO}(r_{ma})$ function between the micelle and an oxygen atom in the distance r_{ma} from the centre of the micelle is defined as

$$U_{MicO}(r_{ma}) = -\varepsilon_{MicO} \cdot \begin{cases} 1 - \left(\dfrac{r_{ma} - r_{\min}}{r_{zero} - r_{\min}} \right)^2 & \forall r_{ma} \in [0, r_{join}[\\ \dfrac{(r_{cut} - r_{ma})^2}{(r_{cut} - r_{zero})(r_{zero} - 2r_{\min} + r_{cut})} & \forall r_{ma} \in [r_{join}, r_{cut}[\\ 0 & \forall r_{ma} \in [r_{cut}, \infty[\end{cases} \tag{6.4}$$

with

$$r_{join} = \frac{r_{zero}^2 - 2r_{\min} r_{zero} + r_{\min} r_{cut}}{r_{cut} - r_{\min}} \tag{6.5}$$

and r_{zero} is the potential reaching zero between the repulsive part and the attractive part corresponding to the surface of the micelle, the minimum of the energy well, r_{min}, and the cut-off radius, r_{cut} (Schumacher (2006)). The depth of the energy well is ε_{MicO}. Due to the empirical nature of this term and since silicon atoms are always surrounded by four covalently bound oxygen atoms, the interaction with silicon atoms can be included into an effective potential that affects only oxygen atoms. The potential well depth of the micelle attraction was set to ε_{MicO} = 1.8066 kJ/mol (Schumacher (2006)). The area of the micelle obtained from the eMC simulation is defined as the combined area of the surfactant segments with the shape defined by the head segments on the surface of the micelle and the radii in the potential defined as for a cylindrical micelle with the same volume. In the micelle defined by the surfactant segments no holes are allowed. The simulations by Jorge *et al.* (2009) showed that silica monomers fit inside the head group layer whereas oligomers do not. Therefore, the assumption that all the silica molecules are outside the micellar region is reasonable. The shape of the micelle is fixed during the simulation. The more complex shape of the micelle increases the computational effort for the calculation of the micelle-oxygen potential. In order to reduce the simulation time, the micelle-oxygen interaction potential is stored in a potential map with a lattice spacing of 0.1 Å.

6.1.4 Results for a linear surfactant

A linear surfactant with equal head and tail length of four beads (H_4T_4) as shown in Figure 6-3 was chosen as a starting point since this model has been used extensively in eMC simulation studies by Patti *et al.* (2007). A head segment, *H*, represents one oxyethylene unit (-C-C-O), whereas one tail segment, *T*, represents two or three CH_2 groups. This means that the surfactant used in this work is roughly equivalent to the real poly(oxyethylene) (PEO) surfactant CH_3-$(CH_2)_y$-$(O$-CH_2-$CH_2)_4$-OH, where *y* is between 7 and 11 (Fodi and Hentschke (2000)). POE surfactants are used for the synthesis of MSU; and SBA-15 is synthesised with POE-poly(oxipropylene)-POE surfactants (Chapter 2). These surfactants are longer than the one used in this simulation study. This short surfactant requires a smaller simulation size and less simulation time and is therefore an ideal test structure.

Figure 6-3 Representation of the linear surfactant used with four head (black) and four tail (grey) segments.

First, a cut through the micelle was used as shape for the micelle with no change of potential over the length of the micelle. The spacing between two lattice sites was set to 5.4 Å resulting in a surfactant volume of the same size as for a model with an ideal cylinder with a diameter of 3.6 nm. The potential map obtained is shown in Figure 6-4, the deviation from a circular/hexagonal shape is strong.

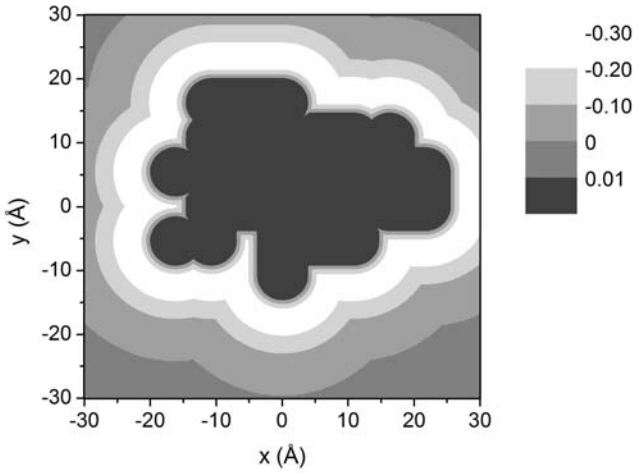

Figure 6-4 Potential map for the kMC simulation created from a cut through the micelle obtained from the eMC simulation with a linear surfactant. The micelle is represented in dark grey and the lighter the area the more attractive it is. Energy is given in 10^{-20} J.

Figure 6-5 shows snapshots of different stages of the kMC simulation for this model. In Figure 6-5 (a) the formation of the initial silica layer around the micelle is shown. 288 Si-O_4 monomers were used in this simulation. Only very few condensation reactions have taken place at that stage. In Figure 6-5 (b) a snapshot of the aggregation step is shown and Figure 6-5 (c) shows the calcined sample. The surface area is larger than for a rod-shaped micelle of the same volume due to the irregular shape of the micelle.

When the micelle is removed during the calcination step, the kMC simulation smoothes out some irregularities. This results in a stronger decrease of the unit cell parameter of 3.2 Å and higher degree of polymerisation with Q_4:Q_3 = 2.2 for the model shown in Figure 6-5 (c) compared to a shrinkage of 1.9 Å and Q_4:Q_3 = 1.24 of a comparable sample generated with a regular model for the micelle with a diameter of 3.6 nm. The Q_n distribution describes the connectivity of the silicon atoms in a silica material. The index (ranging from 0 to 4) gives the number of bonded oxygen. At the beginning of the simulation, only monomers that are Q_0 are present. Q_4 and Q_3 are silicon atoms with four and three bonded oxygen respectively

that are formed during the simulation and their ration is a measure for the degree of polymerisation.

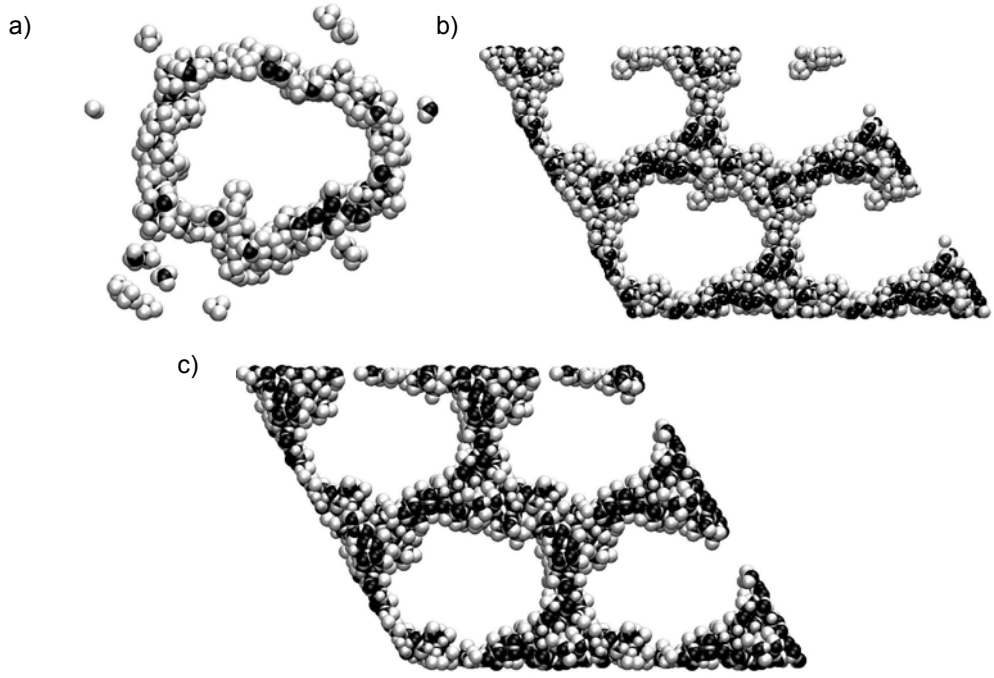

Figure 6-5 Snapshots of the kMC simulation. The model was created using a representation of the micelle taken from the eMC simulation using a linear surfactant. The potential along the pore was assigned a constant value. a) Beginning of the simulation. b) Material after the templated synthesis (four unit cells). c) Material after calcination (four unit cells). Colour coding: black - silicon atoms, grey – oxygen atoms.

In this first simulation, the micelle shape was based on a slice of atomic thickness running across the pore, taken from the EMC simulation, so that the potential did not vary along the axis of the pore. In a second simulation, a 3-D model of the micelle was taken with variations of the potential over the micelle length. This increased the heterogeneity of the potential. Due to the short length of the simulation box in the direction of the micelle (2 nm), only four layers of the lattice were considered. Figure 6-6 shows snapshots of this simulation.

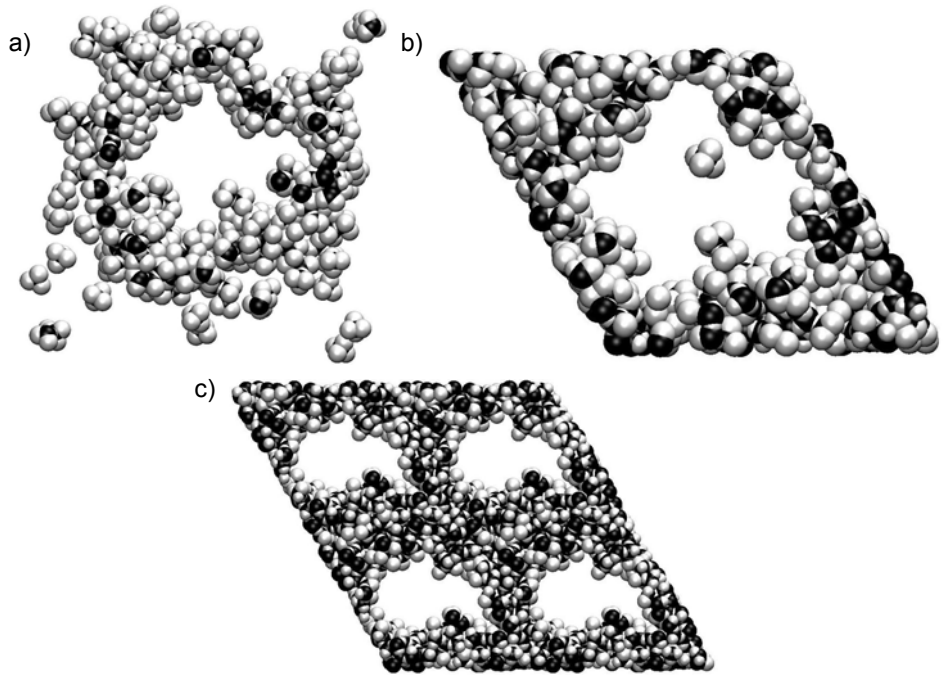

Figure 6-6 Snapshots of the kMC simulation. The model was created using a representation of the micelle taken from the eMC simulation. The potential along the pore varies. a) Beginning of the simulation. b) Material after the templated synthesis. c) Material after calcinations (four unit cells). Colour coding: black – silicon atoms, grey – oxygen atoms.

For a model of the micelle with varying potential along the pore, the shrinkage is further increased to 5.5 Å and Q_4:Q_3 = 2.3. This increased shrinkage is typical for mesoporous silicas synthesised with block-copolymers (Kleitz *et al.* (2003)). Furthermore, in some parts the wall was thin and connections between the pores were established. These connections are also reported for mesoporous silica materials synthesised with block copolymers such as SBA-15. The results of the successful combination of the eMC and kMC methods indicate that this new method might be able to give realistic models for these materials. The surfactants used in the syntheses for these mesoporous silica materials are usually longer than the one used in this study and simulations with more representative chains could give a realistic model for the micelle.

6.1.5 Results for a branched surfactant

The linear surfactant in the previous section is not an adequate representation for surfactants present in the synthesis of MCM-41 in which ionic surfactants are used. The ionic surfactants consist of a long tail and a bulky head. The model that is used in the eMC simulation is therefore modified to represent such a surfactant. The tail is elongated compared to the linear surfactant consisting now of ten beads (T_{10}) each representing one

CH_3 group. The hydrophilic head is not anymore represented by a linear chain but six head segments arranged around one central bead to represent the ionic head (*HH_6*). A representation of the surfactant is shown in Figure 6-7.

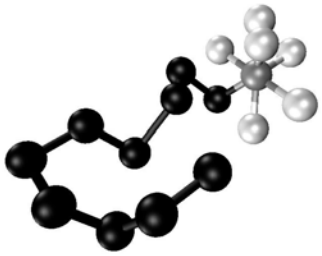

Figure 6-7 Representation of the branched surfactant used in the simulation. It is composed of ten tail segments (black) and six head segments (white) arranged around one central head segment (grey).

The spacing between the beads was set to 1.29 Å to represent the spacing between CH_3 groups. The potential surface was build around three randomly chosen head segments from the six that surround the central head bead. The additional segments were used in the eMC simulation to represent the ionised water. The potential map obtained is shown in Figure 6-8. Due to the branched heads and the smaller spacing used in the implementation, the micelle surface is smoother compared to the micelle obtained from the simulation with the H_4T_4 surfactant and more similar to the ideal geometries used in the original kMC method.

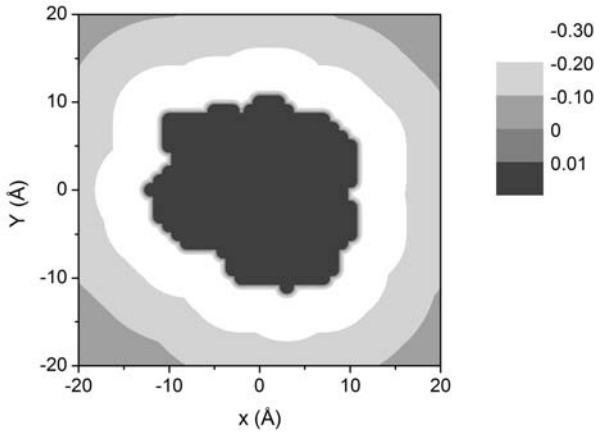

Figure 6-8 Potential map created with the branched surfactant. The micelle is represented in dark grey and the lighter the area the more attractive it is. Energy is given in 10^{-20} J.

173 SiO_4 monomers were used in the simulation. Snapshots of the kMC simulation are shown in Figure 6-9. Again, the decrease in the cell parameter is more pronounced for the model based on the eMC simulation with 3.2 Å compared to 1 Å for the model with a

cylindrical micelle of 11 Å. However, the final degree of polymerisation is similar giving Q_4:Q_3 = 1.5 for the regular micelle and 1.6 for the model based on *HH_6 T_{10}*.

Figure 6-9 Snapshots from the kMC simulation with a potential based on the micelle with the *HH_6 T_{10}* surfactant. a) At the beginning of the simulation; b) during aggregation and c) the calcined sample (four unit cells).

With both pore models, nitrogen adsorption at 77 K was simulated. Figure 6-10 shows the resulting isotherms that were obtained by GCMC simulations. The details of the simulations are described in Section 6.2.1. The interaction parameters used are given in Table 6-2. The isotherms for both models are very similar; the model with the micelle based on the combined approach shows only a higher uptake at medium pressures indicating that the surface area is increased. This was confirmed by the BET surface area calculation using the pressure range 0.003 to 0.03 P/P_0. For the model with the cylindrical micelle a surface area of 722 m^2/g was obtained and for the model based on the new approach, the surface area was 874 m^2/g. Both models reach comparable capacities. The similarity in the isotherms was expected since the representation of the micelle used in this simulation was smoother and closer to a cylinder than the representations with the linear surfactant but rougher than an ideal cylinder, resulting in a higher surface area.

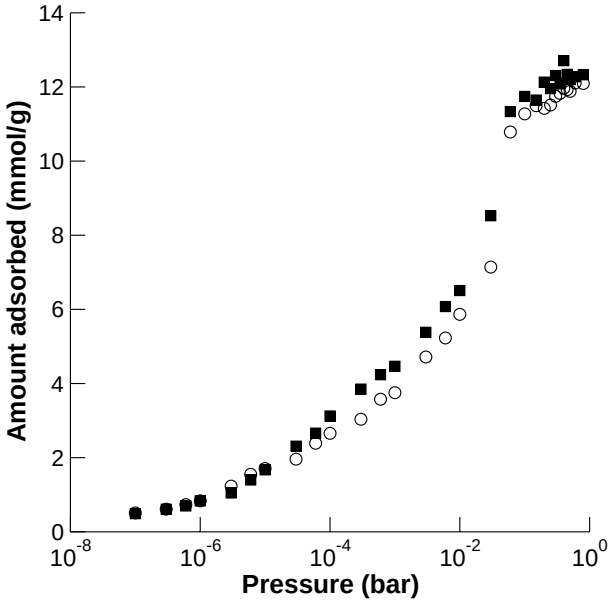

Figure 6-10 Nitrogen adsorption isotherms at 77 K in the models obtained with a cylindrical micelle (○) and with a micelle from the eMC simulation (■).

By using the kMC method with ideal geometries and in combination with the eMC simulation, models with different degrees of surface roughness can be obtained, allowing a greater flexibility in matching experimental data in the future.

6.2 Organic surface groups

In this section, the influence of organic groups placed on the pore surface of MCM-41 on the adsorption of carbon dioxide is investigated. For this, atomistic models were created containing organic surface groups using the methodology developed by Schumacher *et al.* (2006a), introduced in Section 6.2.1. The adsorption data in the previous section showed that the influence of the micelle for the branched surfactant is not pronounced and a model of MCM-41 created with the original kMC method was used in this study. Amine surface groups have been widely studied and improve the adsorption of carbon dioxide due to their strong polarity and reactivity. Here, the adsorption of carbon dioxide on MCM-41 modified with halo surface groups is studied and the halo surface group that shows the highest adsorption in the single gas study is compared to two amine surface groups in a mixture adsorption study.

6.2.1 Computational details

The model used for the unmodified MCM-41 was a basis structure used by Schumacher *et al.* (2006a). The pore structure has a simulated unit cell parameter of 4.5 nm and a pore diameter of 3.78 nm. This pore was used as a base for all the simulations in this chapter. The

surface groups were included in the model structure in a separate NVT simulation run, similar to a post-synthesis modification in experiments. The volume used in this step was restricted to the accessible parts of the pore and the volume inside the wall was excluded. The desired amount of surface groups was introduced by replacing silanol groups as schematically shown in Figure 6-11 a). The initial distribution was random and the energy of the configurations could thus be very high. Subsequently, new configurations were obtained either by regrowing the surface group at its location on the pore surface or by swapping a silanol and an organic surface group. In the swap move, the organic surface group was replaced by the silanol group and regrown in its position as schematically shown in Figure 6-11 b). The new configuration was accepted according to the Metropolis acceptance criterion. This was continued until a local minimum was reached, using 1000 to 2000 swap trials. The final snapshot of this simulation step was used as input for the GCMC simulation.

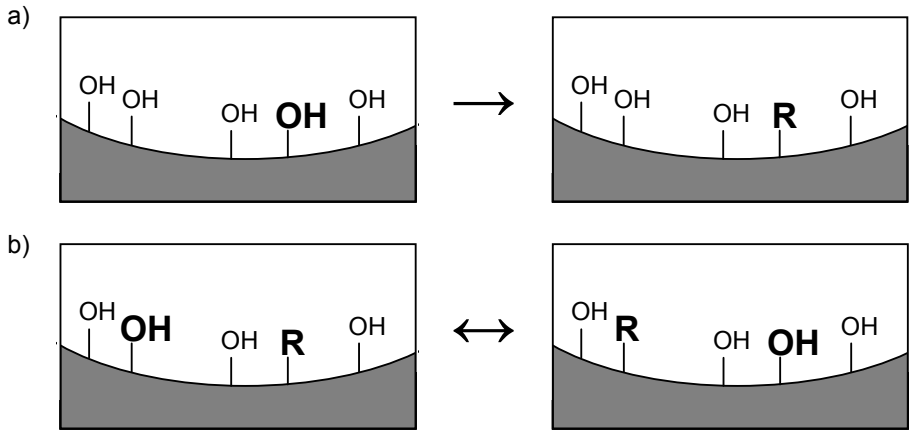

Figure 6-11 Schematic representation of a) the introduction of the surface group (R) by substitution of a hydroxyl group and b) the reversible swap move where the locations of a hydroxyl group and a surface group (R) are exchanged.

The adsorption was simulated in a GCMC run (Section 3.2). The GCMC program used was programmed by Christian Schumacher. Since the number of trials to equilibrate the system varies, the number of Monte Carlo trials was not fixed. The equilibration was determined by applying Spearman's rank-order correlation coefficient (Press *et al.* (1992)) to a sequence of block averages over 50000 trials each. The system was assumed to be equilibrated when the block averages were uncorrelated with a probability greater than 80 %. During the sampling phase of the run, the size of the 95 %-confidence interval for the number of molecules was tested after each block, and the sampling was terminated when it was less than 3 %. The insertion and deletion trial were restricted to the mesopore, the volume for these moves was defined as the largest cylinder fitting inside the unit cell. Accessible cavities in the wall

could be reached by the translation move. Throughout the run, the silicon and oxygen atoms of the pore wall were kept fixed whereas the surface groups were modelled as flexible structures fixed to the wall. The bending and torsion of the surface groups was handled using the dual-cutoff configurational-bias Monte Carlo method (Allen and Tildesley (1989), Frenkel and Smit (2002), Vlugt *et al.* (1998)). The van der Waals interactions were represented by the 12-6 Lennard-Jones potential. For the surface groups, CH_2 was represented by one pseudo atom, whereas the hydrogen atoms of the NH_2 and NH groups were modelled explicitly. The parameterization of the potentials for these surface group molecules was adopted from the optimized potentials for liquid simulations (OPLS) force field (Jorgensen *et al.* (1984), Rizzo and Jorgensen (1999), Jorgensen *et al.* (2004)). The interaction between the surface groups and the carbon dioxide molecules was assumed to be strictly physical. A cutoff radius of 5 σ_{ij} was applied. Tables with the interaction parameters for the surface groups can be found in Appendix E.

Electrostatic interactions are of importance for the adsorption of carbon dioxide and were taken into account by effective point charges. The Coulombic potential was calculated using the Ewald summation (Section 3.2.3.3). The Lennard-Jones parameters for the adsorptive fluids as well as their point charges are given in Table 6-2. The fugacity of the bulk phase was calculated using the Peng-Robinson equation of state.

Table 6-2 Lennard-Jones potential parameter, point charges and bond lengths of the silica framework and adsorptive fluids used.

Species	Site	σ (Å)	εk_B^{-1} (K)	q (e)	Length (Å)	Reference
Silica	Si			+1.2805		Brodka and Zerda (1996), Schumacher *et al.* (2006a)
	O	2.708	185.0	-0.64025	1.6[a]	Brodka and Zerda (1996), Schumacher *et al.* (2006a)
He	He	2.640	10.9			Talu and Myers (2001)
N_2	N	3.31	37.3		0.109[d]	Murthy *et al.* (1980)
CO_2[b]	C	2.785	29.999	+0.6645	1.161[c]	Harris and Yung (1995)
	O	3.064	82.997	-0.33225		Harris and Yung (1995)
CH_4[e]	CH_4	3.73	148.0			Martin and Siepmann (1998)
CO_2[e]	C	2.8	27.0	+0.7	1.16[c]	Potoff and Siepmann (2001)
	O	3.05	79.0	-0.35		Potoff and Siepmann (2001)

[a] Average separation between silicon and oxygen atoms. [b] For single component adsorption. [c] Separation of the carbon and oxygen atom. [d] Separation of the two LJ sites of the model.
[e] For multi-component adsorption.

6.2.2 Halo surface groups

Mesoporous silica materials with surface groups including amines for the adsorption of carbon dioxide have been studied widely as discussed in Chapter 2. Here the influence of other surface groups on the adsorption and selectivity of carbon dioxide is investigated. The

aromatic ring in the most promising surface group by Schumacher *et al.* (2006a), the diaminophenyl group, provides a rigid frame for the polar head groups. Due to the rigid structure, bending of the polar head groups towards the pore surface is not possible and thus interactions between the head groups and the hydroxyl groups are inhibited. Furthermore, the ring is an attractive adsorption site itself due to strong dispersive interactions with the fluid. The phenyl ring was therefore also the basis for the surface groups investigated here. The influence of halo atoms added to the phenyl ring as a different polar head group on the adsorption of carbon dioxide was studied. Halo atoms offer a range of polarities and dispersive interactions and are therefore interesting to study. Two halo surface groups were chosen: monofluorophenyl and monoiodophenyl surface groups. Fluorine is the lightest of the halo atoms with the highest point charge. The point charge of iodine is less than half that of fluorine but the van der Waals interaction with the adsorptive is increased (compare Table 6-3). The resulting surface groups are shown in Figure 6-12.

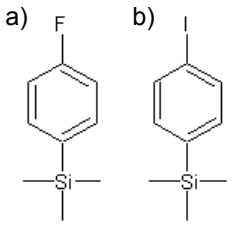

Figure 6-12 Halo surface groups:
a) monofluorophenyl and b) monoiodophenyl.

Table 6-3 Molecular weight and selected interaction parameters and partial charges for the halophenyl surface groups used.

surface group	molecular weight of uc (g/mol)	site [a)]	ε/k_B (K)	σ (nm)	q_i (e_0)
hydroxyl (no surface group)	18547	O	185.0	0.300	-0.533
		H			0.206
10 % monoiodophenyl	23941	I	302.08	0.375	-0.100
10 % monofluorophenyl	20734	F	30.71	0.285	-0.220
5 % monofluorophenyl	19641	F	30.71	0.285	-0.220
5 % difluorophenyl	19893	F	30.71	0.285	-0.200
5 % pentafluorophenyl	20648	F	30.71	0.285	-0.130

[a)] Lennard-Jones parameter and partial charges are given for the head groups of the phenyl based surface groups only. Parameters for all sites of the surface groups can be found in Appendix E.

The adsorption isotherms at 298 K for carbon dioxide on MCM-41 modified with 0.1 surface groups/silicon atom ratio (10 %) and the unmodified sample are shown in Figure 6-13. The material modified with monoiodophenyl takes up more carbon dioxide per unit cell compared to the unmodified material, as can be seen in Figure 6-13 a), due to the strong

dispersive interactions. The increase in adsorption is only observed on a volumetric basis (amount adsorbed per volume adsorbent); the effect is cancelled out when the adsorption is regarded on a gravimetric basis as in Figure 6-13 b), where the molecular weight of the adsorbent is taken into account (amount adsorbed per weight adsorbent). The additional weight due to the surface groups (Table 6-3) decreases the amount adsorbed compared to the unmodified material, especially at pressures higher than 7 bar. The material modified with monofluorophenyl does not take up more molecules but shows a similar uptake compared to the unmodified material. Although the fluorine is more polar than the iodine, it is less polar than the hydroxyl group that was replaced. The increased dispersive interactions due to the large surface group can compensate for that (Figure 6-13 a)) but the additional molecular weight leads to a decreased adsorption on a gravimetric basis for this material (Figure 6-13 b)).

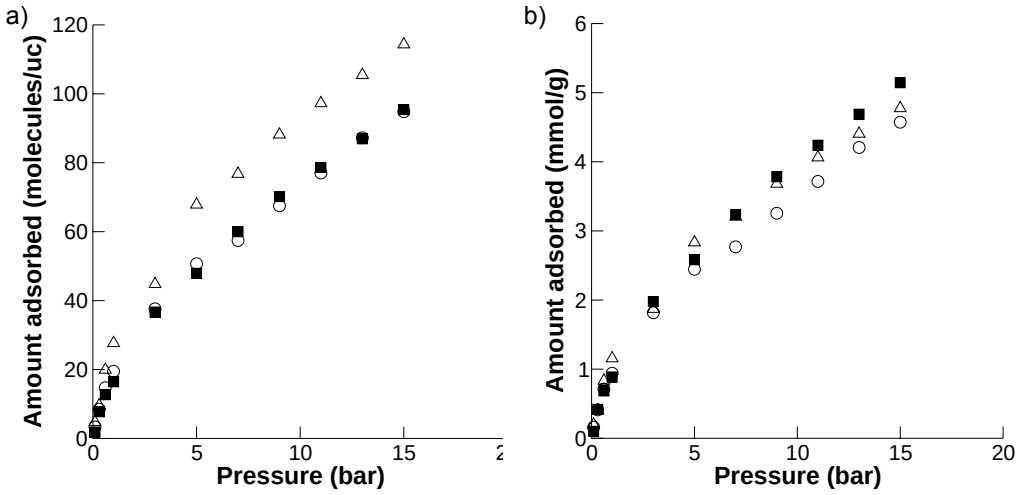

Figure 6-13 Adsorption isotherms (absolute amount adsorbed) for CO_2 at 298 K on MCM-41 (■), with 10 % monoiodophenyl surface groups (Δ) and with 10 % monofluorophenyl surface groups (○).

Figure 6-14 shows the adsorption at low pressures. For monofluorophenyl modified MCM-41, the influence on the adsorption on volumetric (Figure 6-14 a)) as well as on gravimetric basis (Figure 6-14 b)) is very low, the reduced polarity combined with the increased dispersive interactions lead to a similar uptake compared to the unmodified MCM-41. The influence of the monoiodophenyl surface group is also not pronounced, at low pressures up to 0.5 bar, the adsorption is not improved. With increasing pressure, the material with the surface groups exceed the amount adsorbed on the gravimetric basis due the strong dispersive interaction.

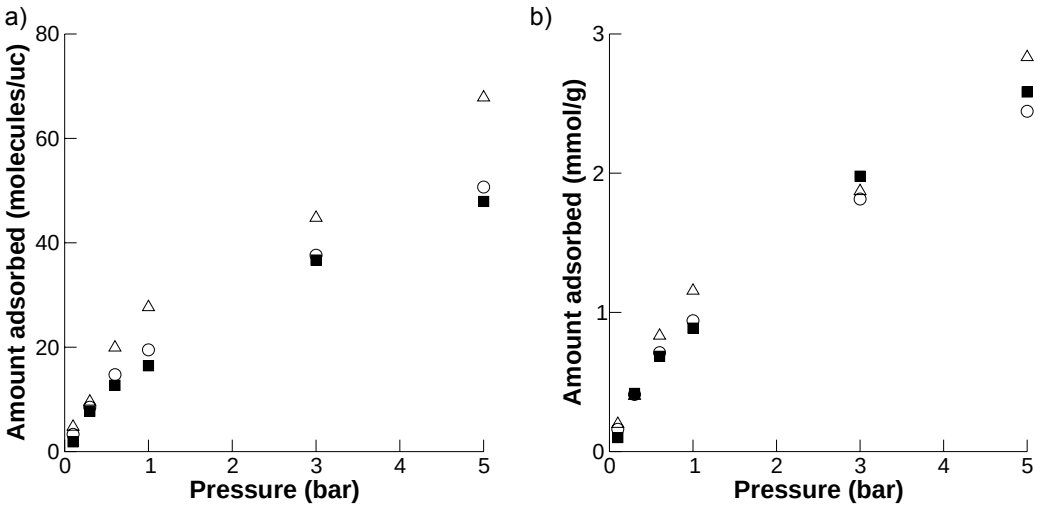

Figure 6-14 Adsorption isotherms (absolute amount adsorbed) for CO_2 at 298 K at low pressure on MCM-41 (■), with 10 % monoiodophenyl surface groups (Δ) and with 10 % monofluorophenyl surface groups (○).

In order to investigate if additional fluorine atoms increase the adsorption due to the higher number of polar adsorption sites, the amount of fluorine that substitutes the hydrogen atoms on the phenyl ring was varied. The influence of additional atoms for the more strongly adsorbing iodine was not investigated since not all parameters necessary for the simulation were available. One, two and five hydrogen atoms were substituted. The resulting monofluorophenyl, difluorophenyl and pentafluorophenyl surface groups are shown in Figure 6-15 and the material was loaded with 5 %.

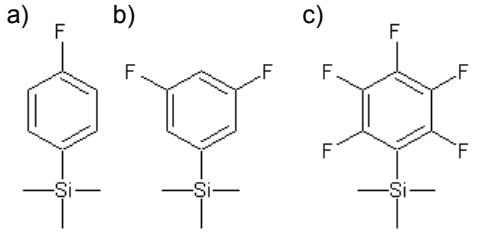

Figure 6-15 Fluorophenyl surface groups: a) monofluorophenyl, b) difluorophenyl and c) pentafluorophenyl

The adsorption isotherms for carbon dioxide at 298 K on these modified pore structures are shown in Figure 6-16 a) for pressures up to 15 bar; and in Figure 6-16 b) the low pressure range is given in more detail.

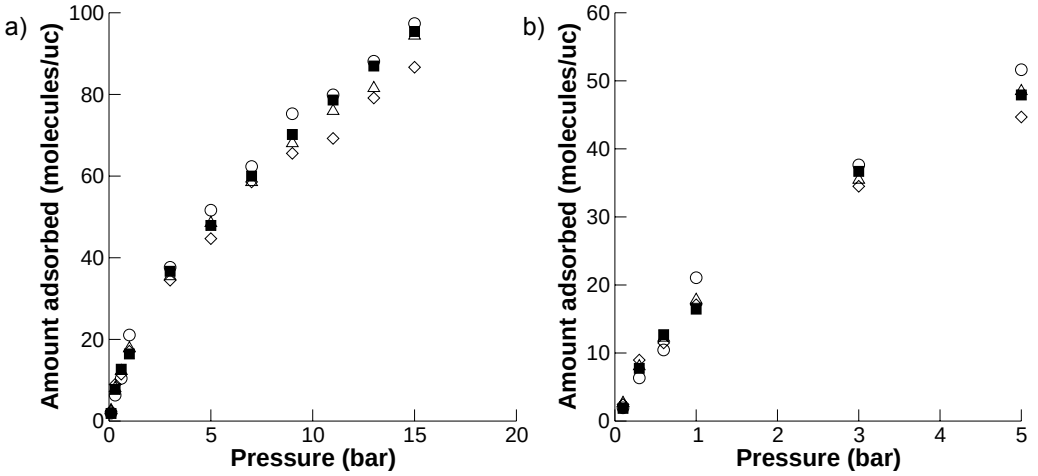

Figure 6-16 Simulated adsorption isotherms (amount adsorbed in molecules per unit cell) at 298 K for carbon dioxide on MCM-41 without surface groups (■), with 5 % monofluorophenyl (○), 5 % difluorophenyl (Δ) and 5 % pentafluorophenyl (◊) surface group modification. a) Whole pressure range and b) low pressure range.

None of the fluorophenyl-surface groups improves the adsorption of carbon dioxide. With an increasing amount of fluorine atoms, the amount adsorbed decreases. The more hydrogen atoms are replaced by fluorine atoms, the lower is the point charge on each fluorine atom (Table 6-3). Due to the weak van der Waals interaction of the fluorine atoms with the carbon dioxide, fluorine modifications are not advantageous. In the low pressure range, the influence of the surface group on the adsorption is very low. When investigating the adsorption on a gravimetric basis as in Figure 6-17, the amount adsorbed decreases further with an increasing number of fluorine atoms due to the additional molecular weight.

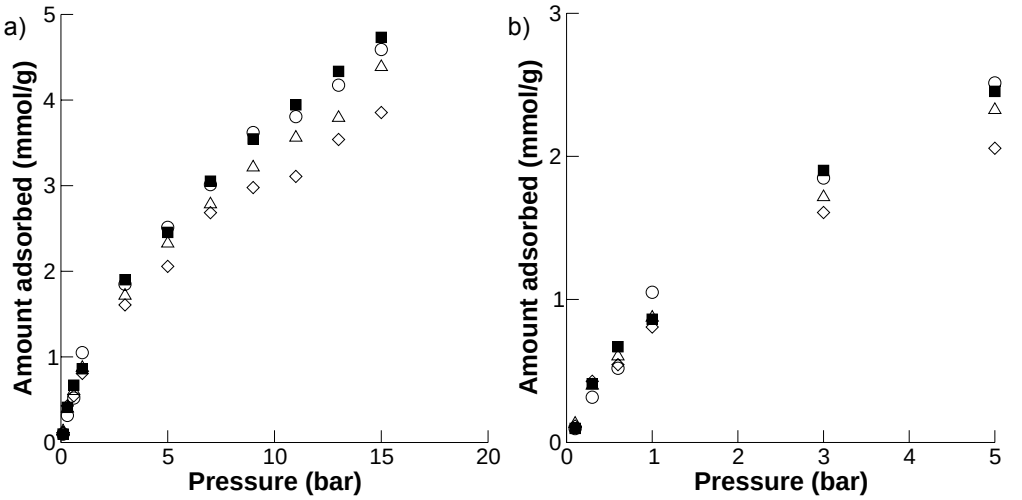

Figure 6-17 Simulated adsorption isotherms at 298 K for carbon dioxide on MCM-41 without surface groups (■), with 5 % monofluoro-phenyl (○), 5 % difluorophenyl (Δ) and 5 % pentafluorophenyl (◊) surface group modification. a) Whole pressure range and b) low pressure range.

Experimental isotherms for carbon dioxide were measured at 298 K on MCM-41 and pentafluorophenyl modified MCM-41. The samples were provided by Karen Wilson from the University of York. The surfactant used in the synthesis was cetyltrimethylammonium-bromide (CTAB, $(C_{16}H_{33})N(CH_3)_3Br$). The experimental unit cell parameter of 3.65 nm and the pore size of 2.50 nm are smaller than the ones used in the simulation of 4.50 nm and 3.78 nm respectively. Therefore, a comparison of the trends in the experimental and simulated isotherms is done instead of a direct comparison. The elemental analysis, done by Paul Wright's group in St. Andrews of the sample modified with pentafluorophenyl, gave a surface group to silicon concentration of 5.7 %. This will be compared to a model in the simulation with 5 % surface groups since it is expected that not all surface groups in the experimental sample are accessible. In Figure 6-18, the experimental and simulated carbon dioxide isotherms at 298 K for MCM-41 and pentafluorophenyl-MCM-41 are shown.

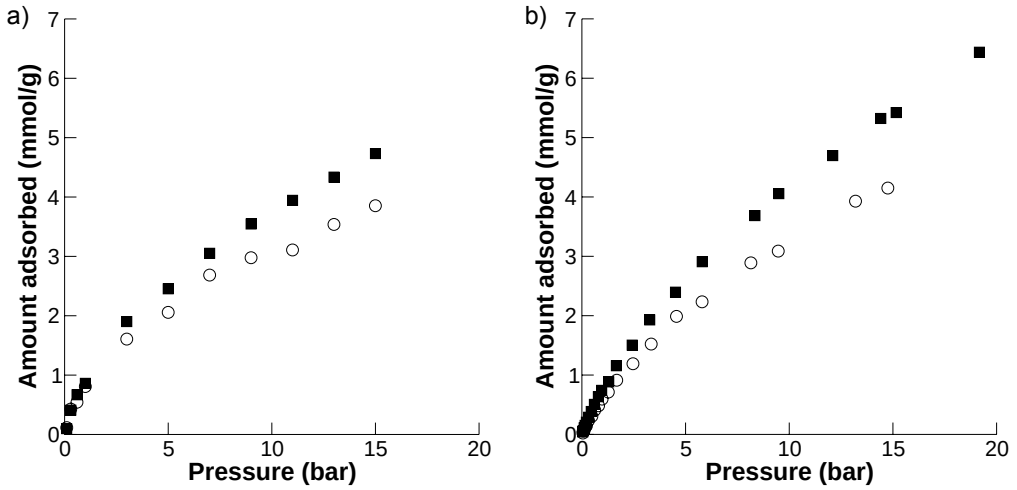

Figure 6-18 a) Simulated and b) experimental carbon dioxide isotherms at 298 K for MCM-41 (■) and pentafluorophenyl-MCM-41 (○).

The trends in the simulated and experimental isotherms are similar. The modified samples adsorb less than the unmodified MCM-41 over the whole pressure range investigated. With increasing pressure, the difference between the modified and unmodified samples increases. At 5 bar, the modified sample adsorbs 19.9 % less in the experiment and 16.2 % less in the simulation. At 15 bar, this is increased further to 22.6 % and 18.5 %, respectively. The experiments confirm the trend observed in the simulation, the differences observed are likely to be due to the different pore sizes.

6.2.3 Methane - carbon dioxide mixture

For the carbon dioxide adsorption from a gas mixture, not only the total amount adsorbed is important but also the selectivity of one component over another. To investigate the effect of different surface groups, the adsorption of an equimolar mixture of the unpolar methane and the quadrupolar carbon dioxide at 298 K was chosen. The gas mixture is also industrially interesting: land fill gas (45-65 % CH_4, 35-55 % CO_2) and biogas (50-75 % CH_4, 25-45 % CO_2) require a removal of carbon dioxide for the methane to be used as energy source (Cavenati *et al.* (2005), Cavenati *et al.* (2008)).

The unmodified MCM-41 is taken as a reference and three modified models with 10 % surface groups each are investigated. As an example for a halo-modified group the monoiodophenyl group was chosen. The diaminophenyl-group was taken as the surface group showing the highest selectivity for carbon dioxide from flue gas in the study by Schumacher *et al.* (2006a). Furthermore, another diamino surface group, the

aminoethylaminoproyl group was used, containing a primary and a secondary amine but no ring structure. The surface groups are depicted in Figure 6-19.

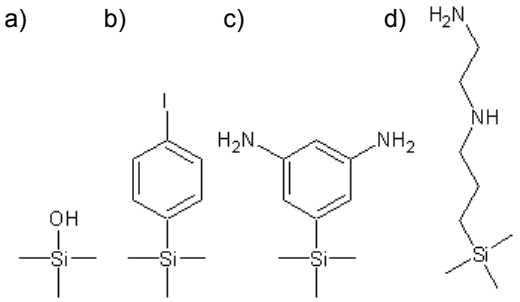

Figure 6-19 Surface groups used in the carbon dioxide-methane mixture adsorption: a) silanol, b) monoiodophenyl, c) diaminophenyl, and d) aminoethylaminopropyl.

The selectivities for carbon dioxide are shown in Figure 6-20. Oscillations in the curves occur due to statistical errors, which are larger than for the pure-silica pore due to the flexibility of the surface groups, which rearrange themselves on relatively long periods. At low pressure, the selectivity for carbon dioxide is increased due to carbon dioxide molecules being adsorbed at the most attractive sites. For monoiodophenyl this increase at low pressure is lower than for the other materials due to the reduced polarity of the surface group (Table 6-4). Comparing the selectivities over the whole pressure range, the aminoethylaminopropyl and monoiodophenyl groups only slightly increase the carbon dioxide selectivity over methane. The monoiodophenyl is less polar than the hydroxyl group that it replaces. The dispersive interactions with the fluid molecules are increased but this effect is not limited to the carbon dioxide molecules as the electrostatic interactions but also affect the interactions with the methane molecules. The two amino groups in the aminoethylaminopropyl surface groups provide very attractive adsorption sites for carbon dioxide but the molecule is flexible and can therefore bend back towards the pore surface making it less accessible for the adsorption of carbon dioxide and shielding polar hydroxyl groups on the pore surface. Although the diaminophenyl group contains the same number of amino groups as the aminoethylaminopropyl group, the rigid aromatic ring keeps the amine groups exposed to the pore centre. The more polar diaminophenyl outperforms the monoiodophenyl group that provides stronger dispersive interactions. The diaminophenyl group increases the selectivity by about 50 % and is the most effective surface group studied.

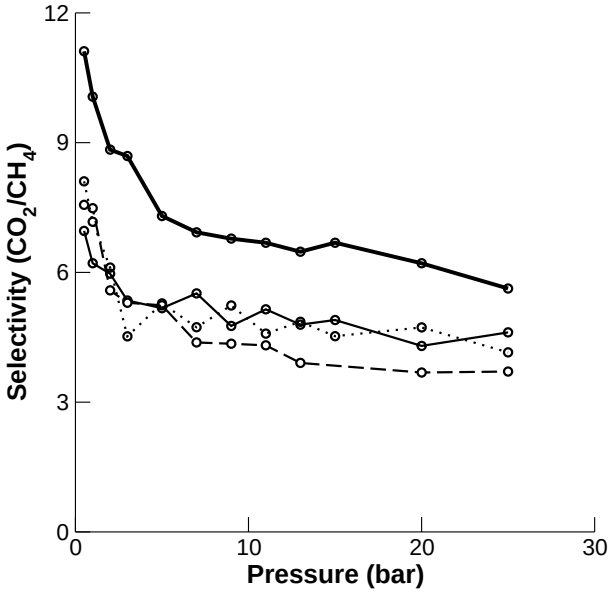

Figure 6-20 Selectivity for carbon dioxide from an equimolar carbon dioxide-methane mixture at 298 K for MCM-41 (dashed line), 10 % monoiodophenyl-MCM-41 (thin line), 10 % aminoethylaminopropyl-CM-41 (dotted line) and 10 % diaminophenyl-MCM-41 (thick line),

Table 6-4 Molecular weight and selected interaction parameters and partial charges for the surface groups used in the mixture study.

surface group	molecular weight of uc (g/mol)	site [a]	ε/k_B (K)	σ (nm)	q_i (e_0)
hydroxyl (no surface group)	18547	O	185.0	0.300	-0.533
		H			0.206
10 % monoiodophenyl	23941	I	302.08	0.375	-0.100
10 % diaminophenyl	21161	N [b]	85.589	0.33	-0.90
		H [b]			0.36
10 % aminoethyl-aminopropyl	20988	N [c]	85.589	0.33	-0.780
		H [c]			0.380
		N [b]	85.589	0.33	-0.9
		H [b]			0.36

[a] Lennard-Jones parameter and partial charges for the sites of the surface groups are given for the iodine and the amino groups ([b] primary amine, [c] secondary amine) only. Parameters for all sites of the surface groups can be found in Appendix E.

6.3 Conclusions

In this chapter, a methodology that combines two different simulation techniques to obtain atomistic models of periodic, ordered mesoporous materials is presented. Hexagonally ordered mesoporous phases were obtained from eMC simulations. The condensation reaction around a micelle obtained from the eMC simulation was modelled by performing off-lattice kMC simulations.

Using a linear surfactant with a hydrophobic and hydrophilic part of equal length resulted in a pore model that showed an increased shrinkage during the calcination step and connections between the pores. With a branched surfactant that had a longer hydrophobic tail the pore model obtained was similar to the model obtained with a rod-shaped micelle. At pressures below saturation, an increase in the amount adsorbed for nitrogen at 77 K was observed for a model pore that reached the same capacity.

This combined method has the potential to be extended to model a range of periodic mesoporous silicas from predicting the mesophases formed from a given initial synthesis mixture to an atomistic representation of a pore that can be used in adsorption studies, extending the kMC method to a wider range of micelle shapes. In the eMC simulation, the surfactant can be modified to represent different types of surfactants as shown here. Furthermore, the length of the surfactant can be adapted and by changing the concentration of the surfactant a cubic phase can be obtained. Whereas MCM-41 is synthesised using ionic surfactants, a range of mesoporous silica materials with a hexagonal arrangement of pores have been synthesised using other surfactants, e.g. SBA-15 with block-copolymers (Zhao *et al.* (1998)). SBA-15 is more difficult to model due to connections between the main channels and an increased heterogeneity of the pore wall. The increased shrinkage upon calcination and the connection between pores that was observed in the simulation with the H_4T_4 surfactant have been reported for this experimental synthesis (Zhao *et al.* (1998), Kleitz *et al.* (2003)). Therefore, with this combined method, models for these materials might be possible. For materials with connections between the channels a larger simulation cell might be necessary, including more than one micelle to prevent the formation of secondary channels from these connections due to the periodic boundary conditions. Also a longer simulation cell including a representative 3D-model of the micelle would increase the quality of the model.

Furthermore, the influence of different surface groups on the adsorption of carbon dioxide has been investigated. It was shown that halo-groups did not improve the adsorption on a gravimetric basis. However, monoiodo-modified MCM-41 showed a higher uptake of carbon dioxide molecules per unit cell and an increased selectivity for carbon dioxide for an equimolar carbon dioxide – methane mixture than the unmodified sample. The long aminoethyl-aminopropyl chain did only slightly increase the selectivity; the best surface group was diaminophenyl which is a promising structure for further studies.

7 Summary

Metal-organic frameworks and mesoporous silica materials are adsorbents with many tuneable properties. Due to the large number of possible materials and the resulting opportunities, simulations are an important way to explore their potential.

Many researchers have studied adsorption on metal organic frameworks by experiment or simulation. The discrepancies in the reported experimental adsorption data as discussed in Chapter 2, as well as the fact that the force fields available for the simulation of the adsorption are generic force fields, not specifically developed for metal-organic frameworks, lead to the need for large experimental data sets measured on good quality samples to assess the full potential of the materials and to provide sufficient data for the validation of the simulations. In this thesis, extensive experimental adsorption data for the metal-organic framework CuBTC are provided. The adsorption of methane, ethane, propane, nitrogen and carbon dioxide at 298 K up to 25 bar was measured and, furthermore, an isotherm for an equimolar methane – carbon dioxide mixture was recorded. This is the first time that such a comprehensive set of data is provided for CuBTC.

The adsorption data obtained from the simulations and the experiments are in good agreement at low and medium pressure, indicating a good representation of the fluid-framework interactions. At pore filling, the simulations predict a higher capacity. Although the experimental sample gives a higher uptake than previously reported, any sample has defects and deviates from the ideal infinite perfect crystal used in the simulations. Mixture adsorption was investigated further by simulation, studying the influence of the bulk composition as well as pressure on methane – ethane, methane – carbon dioxide and ethane – carbon dioxide mixtures. The mixture simulations gave a high selectivity for carbon dioxide and ethane over methane in the respective mixtures. In the ethane-carbon dioxide mixture, the selectivity is close to unity and a separation is not easily obtained. In the mixture simulations, the contribution of the electrostatic interactions due to the quadrupole of the carbon dioxide molecules were studied in detail, showing that at high carbon dioxide loading, the selectivity is increased due to the carbon dioxide-carbon dioxide electrostatic interactions.

Comprehensive sets of data such as the one presented are essential for the evaluation of the simulations and experiments. The results showed that the adsorption was predicted well in

the low and medium pressure range using the force fields available. A larger set of data, including measurements on different metal organic frameworks obtained by optimized syntheses methods, is required for a critical examination of the predictive powers of the simulations of adsorption on metal organic frameworks as well as their limitations.

Hydrogen storage is one of the areas of high interest since hydrogen is an important energy carrier. Metal-organic frameworks have drawn attention due to initial promising hydrogen adsorption data reported (Rosi *et al.* (2003)). Although some of the data could not be reproduced, hopes for improved hydrogen storage in metal-organic frameworks are high due to the large number of existing structures and countless more possible structures. In this thesis, hydrogen adsorption and thermal desorption on a range of metal-organic frameworks were investigated. Desorption spectra were simulated and compared to experimental desorption spectra by Panella *et al.* (2008). In the simulation, the desorption takes place at lower temperatures but similar peaks were observed. To investigate the thermal desorption on metal-organic frameworks further, spectra for more materials were simulated studying the effect of the metal, the linker, and catenation. The desorption spectra were related to adsorption data obtained at 20 K, the starting temperature for the thermal desorption. At this low temperature, the adsorption sites are revealed as movements of the molecules at this temperature are restricted. The peaks in the spectra could be correlated to features in the low temperature isotherm. Furthermore, the simulations provided insight into the system, allowing for a better understanding where the adsorption is taking place.

The substitution of the metal in MIL-53 was shown to have two effects on the adsorption: (1) the stronger interaction between the aluminium and the hydrogen increased the adsorption at lower pressures compared to chromium. At the saturation loading, nearly the same number of molecules can be found in MIL-53-Al and MIL-53-Cr but due to the lower molecular weight of the aluminium, the adsorption on a gravimetric basis is increased. These effects of the metal have been reported before for other materials (Han *et al.* (2007)), in this study it was furthermore shown that the energy of the adsorbed molecules shows a wider energy distribution in the chromium material than in the aluminium version. The linker length has a strong influence on the capacity due to the change in the pore volume as shown for IRMOF-1, IRMOF-8 and IRMOF-10. At very low loadings, the difference is negligible since the most attractive sites in the corners are very similar in all frameworks. The adsorption in this pressure range was increased by the additional ring in IRMOF-7. Catenation reduces the capacity of the material considerably, but due to the additional adsorption sites, the

adsorption is strongly increased in the low pressure range. Furthermore, the energy distribution of the adsorbed molecules is much wider.

For the mesoporous silica materials, modelling the structure is one of the challenges due to the amorphous structure on the molecular level. In this thesis, a new method is introduced. The approach combines two simulations on different levels of detail. The phase formation has previously been successfully modelled using an equilibrium Monte Carlo simulation with coarse grained models (Patti *et al.* (2007)). In the methodology developed in this thesis, micelles were extracted from the ordered phase obtained by such an equilibrium Monte Carlo simulation and an atomistic model created around it using a kinetic Monte Carlo simulation. The shape and properties of the surfactant in the equilibrium Monte Carlo simulation can be varied, as it is shown in the results presented. Therefore, models representing different types of surfactants can be employed. This method has the potential to create atomistic models for a wide range of mesoporous silica materials.

The chemistry of the pore surface can be changed by including organic surface groups which influence the adsorption properties. For the mesoporous silica material MCM-41, the effect of organic surface groups on the adsorption of carbon dioxide was studied by simulation. New surface groups including halo atoms were tested. These halo-phenyl surface groups did not improve the adsorption on the gravimetric basis. However, the material modified with the mono-iodophenyl surface group did increase the adsorption on a volumetric basis compared to the unmodified material and led to a slight increase of the selectivity for carbon dioxide in the adsorption of an equimolar methane-carbon dioxide mixture. Diaminophenyl modified MCM-41 showed the highest selectivity out of the materials studied.

Appendices

A References

Acosta, E. J., C. S. Carr, E. E. Simanek and D. F. Shantz (2004). Engineering nanospaces: Iterative synthesis of melamine-based dendrimers on amine-functionalized SBA-15 leading to complex hybrids with controllable chemistry and porosity. *Advanced Materials* 16 (12): 985-+.

Adamson, A. W. and A. P. Gast (1997). *Physical Chemistry of Surfaces*. 6th Edition, New York, Wiley & Sons.

Allen, M. P. and D. J. Tildesley (1989). *Computer Simulation of Liquids*, Oxford, UK, Clarendon Press.

Attard, G. S., J. C. Glyde and C. G. Goltner (1995). Liquid-Crystalline Phases as Templates for the Synthesis of Mesoporous Silica. *Nature* 378 (6555): 366-368.

Babarao, R. and J. Jiang (2008). Molecular Screening of Metal-Organic Frameworks for CO_2 Storage. *Langmuir* 24 (12): 6270-6278.

Bae, Y. S., K. L. Mulfort, H. Frost, P. Ryan, S. Punnathanam, L. J. Broadbelt, J. T. Hupp and R. Q. Snurr (2008). Separation of CO_2 from CH_4 using mixed-ligand metal-organic frameworks. *Langmuir* 24 (16): 8592-8598.

Bagshaw, S. A., E. Prouzet and T. J. Pinnavaia (1995). Templating Of Mesoporous Molecular-Sieves By Nonionic Polyethylene Oxide Surfactants. *Science* 269 (5228): 1242-1244.

Barthelet, K., J. Marrot, D. Riou and G. Férey (2001). A breathing hybrid organic-inorganic solid with very large pores and high magnetic characteristics. *Angewandte Chemie-International Edition* 41 (2): 281-+.

Beck, J. S., J. C. Vartuli, W. J. Roth, M. E. Leonowicz, C. T. Kresge, K. D. Schmitt, C. T. W. Chu, D. H. Olson, E. W. Sheppard, S. B. McCullen, J. B. Higgins and J. L. Schlenker (1992). A New Family of Mesoporous Molecular-Sieves Prepared with Liquid-Crystal Templates. *Journal of the American Chemical Society* 114 (27): 10834-10843.

Bordiga, S., L. Regli, F. Bonino, E. Groppo, C. Lamberti, B. Xiao, P. S. Wheatley, R. E. Morris and A. Zecchina (2007). Adsorption properties of HKUST-1 toward hydrogen and other small molecules monitored by IR. *Physical Chemistry Chemical Physics* 9 (21): 2676-2685.

Breneman, C. M.; Wiberg, K. B. (1990), Determining atom-centered monopoles from molecular electrostatic potentials – The need for high sampling density in formamide conformational analysis. Journal of Computational Chemistry, 11: 361.

Brodka, A. and T. W. Zerda (1996). Properties of liquid acetone in silica pores: Molecular dynamics simulation. *Journal of Chemical Physics* 104 (16): 6319-6326.

Brunauer, S., P. H. Emmett and E. Teller (1938). Adsorption of gases in multimolecular layers. *Journal of the American Chemical Society* 60: 309-319.

Buch, V. (1994). Path-Integral Simulations of Mixed Para-D-2 and Ortho-D-2 Clusters - the Orientational Effects. *Journal of Chemical Physics* 100 (10): 7610-7629.

Burde, J. T. and M. M. Calbi (2007). Physisorption kinetics in carbon nanotube bundles. *Journal of Physical Chemistry C* 111 (13): 5057-5063.

Catlow, C. R. A., L. Ackermann, R. G. Bell, F. Cora, D. H. Gay, M. A. Nygren, J. C. Pereira, G. Sastre, B. Slater and P. E. Sinclair (1997). Computer modelling as a technique in solid state chemistry - Introductory lecture. *Faraday Discussions* 106: 1-40.

Cavenati, S., C. A. Grande, A. Rodrigues, x, E. rio, C. Kiener, Mu, x and U. ller (2008). Metal Organic Framework Adsorbent for Biogas Upgrading. *Ind. Eng. Chem. Res.* 47 (16): 6333-6335.

Cavenati, S., C. A. Grande and A. E. Rodrigues (2005). Upgrade of methane from landfill gas by pressure swing adsorption. *Energy & Fuels* 19 (6): 2545-2555.

Chae, H. K., D. Y. Siberio-Perez, J. Kim, Y. Go, M. Eddaoudi, A. J. Matzger, M. O'Keeffe and O. M. Yaghi (2004). A route to high surface area, porosity and inclusion of large molecules in crystals. *Nature* 427 (6974): 523-527.

Chowdhury, P., C. Bikkina, D. Meister, F. Dreisbach and S. Gumma (2009). Comparison of adsorption isotherms on Cu-BTC metal organic frameworks synthesized from different routes. *Microporous and Mesoporous Materials* 117 (1-2): 406-413.

Chui, S. S. Y., S. M. F. Lo, J. P. H. Charmant, A. G. Orpen and I. D. Williams (1999). A chemically functionalizable nanoporous material $[Cu_3(TMA)_2(H_2O)_3]_n$. *Science* 283 (5405): 1148-1150.

Coasne, B., F. R. Hung, R. J. M. Pellenq, F. R. Siperstein and K. E. Gubbins (2006). Adsorption of sample gases in MCM-41 materials: The role of surface roughness. *Langmuir* 22 (1): 194-202.

Darkrim, F.; Levesque, D. (1998) Monte Carlo simulations of hydrogen adsorption in single-walled carbon nanotubes. *J. Chem. Phys*. 109: 4981

Department of Energy, U. S. (2005). Hydrogen Fuel Cells & Infrastructure Technologies Program. Multi-Year Research, Development and Demonstration Plan. Retrieved 30 July 2008, from http://www.eere.energy.gov/hydrogenandfuelcells/mypp.

Dincă, M. and Jeffrey R. Long (2008). Hydrogen Storage in Microporous Metal-Organic Frameworks with Exposed Metal Sites. *Angewandte Chemie International Edition* 47 (36): 6766-6779.

Düren, T., F. Millange, G. Férey, K. S. Walton and R. Q. Snurr (2007). Calculating geometric surface areas as a characterization tool for metal-organic frameworks. *Journal of Physical Chemistry A* 111 (42): 15350-15356.

Düren, T., L. Sarkisov, O. M. Yaghi and R. Q. Snurr (2004). Design of new materials for methane storage. *Langmuir* 20 (7): 2683-2689.

Eddaoudi, M., J. Kim, N. Rosi, D. Vodak, J. Wachter, M. O'Keefe and O. M. Yaghi (2002). Systematic design of pore size and functionality in isoreticular MOFs and their application in methane storage. *Science* 295 (5554): 469-472.

Ewald, P. P. (1921). The calculation of optical and electrostatic grid potential *Annalen der Physik* 64 (3): 253-287.

Fairen-Jimenez, D.; Lozano-Casal, P.; Düren, T. (2009) Assessing Generic Force Fields to describe Adsorption on Metal-Organic Frameworks. *Characterisation of Porous Solids VIII*, 318: 80

Férey, G. (2008). Hybrid porous solids: past, present, future. *Chemical Society Reviews* 37 (1): 191-214.

Férey, G., M. Latroche, C. Serre, F. Millange, T. Loiseau and A. Percheron-Guégan (2003). Hydrogen adsorption in the nanoporous metal-benzenedicarboxylate $M(OH)(O_2C\text{-}C_6H_4\text{-}CO_2)$ ($M = Al^{3+}$, Cr^{3+}), MIL-53. *Chemical Communications* (24): 2976-2977.

Feuston, B. P. and J. B. Higgins (1994). Model Structures for MCM-41 Materials - a Molecular-Dynamics Simulation. *Journal of Physical Chemistry* 98 (16): 4459-4462.

Feynman, R. P. and A. R. Hibbs (1965). *Quantum Mechanics and Path Intergrals*, New York, McGraw-Hill.

Fodi, B. and R. Hentschke (2000). Simulated phase behavior of model surfactant solutions. *Langmuir* 16 (4): 1626-1633.

Forster, P. M., P. M. Thomas and A. K. Cheetham (2002). Biphasic solvothermal synthesis: A new approach for hybrid inorganic-organic materials. *Chemistry of Materials* 14 (1): 17-+.

Fox, J. P. and S. P. Bates (2005). Adsorption and structure of hydrocarbons in MCM-41: a computational study. *Langmuir* 21 (10): 4746-4754.

Frenkel, D. and B. Smit (2002). *Understanding Molecular Simulation*. 2nd edition, Academic Press.

Frierson, M. R., M. R. Imam, V. B. Zalkow and N. L. Allinger (1988). The MM2 Force-Field for Silanes and Polysilanes. *Journal of Organic Chemistry* 53 (22): 5248-5258.

Garberoglio, G., A. I. Skoulidas and J. K. Johnson (2005). Adsorption of gases in metal organic materials: Comparison of simulations and experiments. *Journal of Physical Chemistry B* 109 (27): 13094-13103.

Gaussian 03 (2004), R. D.; Frisch, M. J.; Trucks, G. W.; Schlegel, H. B.; Scuseria, G. E.; Robb, M. A.; Cheeseman, J. R.; Montgomery, J., J. A.; Vreven, T.; Kudin, K. N.; Burant, J. C.; Millam, J. M.; Iyengar, S. S.; Tomasi, J.; Barone, V.; Mennucci, B.; Cossi, M.; Scalmani, G.; Rega, N.; Petersson, G. A.; Nakatsuji, H.; Hada, M.; Ehara, M.; Toyota, K.; Fukuda, R.; Hasegawa, J.; Ishida, M.; Nakajima, T.; Honda, Y.; Kitao, O.; Nakai, H.; Klene, M.; Li, X.; Knox, J. E.; Hratchian, H. P.; Cross, J. B.; Bakken, V.; Adamo, C.; Jaramillo, J.; Gomperts, R.; Stratmann, R. E.; Yazyev, O.; Austin, A. J.; Cammi, R.; Pomelli, C.; Ochterski, J. W.; Ayala, P. Y.; Morokuma, K.; Voth, G. A.; Salvador, P.; Dannenberg, J. J.; Zakrzewski, V. G.; Dapprich, S.; Daniels, A. D.; Strain, M. C.; Farkas, O.; Malick, D. K.; Rabuck, A. D.; Raghavachari, K.; Foresman, J. B.; Ortiz, J. V.; Cui, Q.; Baboul, A. G.; Clifford, S.; Cioslowski, J.; Stefanov, B. B.; Liu, G.; Liashenko, A.; Piskorz, P.; Komaromi, I.; Martin, R. L.; Fox, D. J.; Keith, T.; Al-Laham, M. A.; Peng, C. Y.; Nanayakkara, A.; Challacombe, M.; Gill, P. M. W.; Johnson, B.; Chen, W.; Wong, M. W.; Gonzalez, C.; Pople, J. A. Gaussian, Inc. Wallingford CT, 2004.

Gelb, L. D. and K. E. Gubbins (1999). Pore size distributions in porous glasses: A computer simulation study. *Langmuir* 15 (2): 305-308.

Gupta, A., S. Chempath, M. J. Sanborn, L. A. Clark and R. Q. Snurr (2003). Object-oriented programming paradigms for molecular modeling. *Molecular Simulation* 29 (1): 29-46.

Hafizovic, J., M. Bjorgen, U. Olsbye, P. D. C. Dietzel, S. Bordiga, C. Prestipino, C. Lamberti and K. P. Lillerud (2007). The inconsistency in adsorption properties and powder XRD data of MOF-5 is rationalized by framework interpenetration and the presence of organic and inorganic species in the nanocavities. *Journal of the American Chemical Society* 129 (12): 3612-3620.

Han, S. S., W. Q. Deng and W. A. Goddard (2007). Improved designs of metal-organic frameworks for hydrogen storage. *Angewandte Chemie-International Edition* 46 (33): 6289-6292.

Harlick, P. J. E. and A. Sayari (2006). Applications of pore-expanded mesoporous silicas. 3. Triamine silane grafting for enhanced CO_2 adsorption. *Industrial & Engineering Chemistry Research* 45 (9): 3248-3255.

Harlick, P. J. E. and A. Sayari (2007). Applications of pore-expanded mesoporous silica. 5. Triamine grafted material with exceptional CO_2 dynamic and equilibrium adsorption performance. *Industrial & Engineering Chemistry Research* 46 (2): 446-458.

Harris, J. G. and K. H. Yung (1995). Carbon Dioxides Liquid-Vapor Coexistence Curve and Critical Properties as Predicted by a Simple Molecular-Model. *Journal of Physical Chemistry* 99 (31): 12021-12024.

He, Y. F. and N. A. Seaton (2003). Experimental and computer simulation studies of the adsorption of ethane, carbon dioxide, and their binary mixtures in MCM-41. *Langmuir* 19 (24): 10132-10138.

Hicks, J. C., J. H. Drese, D. J. Fauth, M. L. Gray, G. Qi and C. W. Jones (2008). Designing Adsorbents for CO_2 Capture from Flue Gas-Hyperbranched Aminosilicas Capable of Capturing CO_2 Reversibly. *J. Am. Chem. Soc.* 130 (10): 2902-2903.

Hill, T. L. (1960). *An Introduction to Statistical Thermodynamics*, Reading, Addison-Wesley.

Hiyoshi, N., K. Yogo and T. Yashima (2004). Adsorption of carbon dioxide on amine modified SBA-15 in the presence of water vapor. *Chemistry Letters* 33 (5): 510-511.

Hoffmann, F., M. Cornelius, J. Morell and M. Fröba (2006). Silica-based mesoporous organic-inorganic hybrid materials. *Angewandte Chemie-International Edition* 45 (20): 3216-3251.

Huang, H. P., Y. Shi, W. Li and S. G. Chang (2001). Dual alkali approaches for the capture and separation of CO_2. *Energy & Fuels* 15 (2): 263-268.

Jorge, M., J. R. B. Gomes, M. Cordeiro and N. A. Seaton (2009). Molecular Dynamics Simulation of the Early Stages of the Synthesis of Periodic Mesoporous Silica. *Journal of Physical Chemistry B* 113 (3): 708-718.

Jorgensen, W. L. (2007). personal communication.

Jorgensen, W. L., J. D. Madura and C. J. Swenson (1984). Optimized Intermolecular Potential Functions for Liquid Hydrocarbons. *Journal of the American Chemical Society* 106 (22): 6638-6646.

Jorgensen, W.L.; Maxwell, D.S.; Tirado-Rives, J. (1996) Development and testing of the OPLS all-atom force field on conformational energetics and properties of organic liquids. *Journal of the American Chemical Society*, 118:11225

Jorgensen, W. L., J. P. Ulmschneider and J. Tirado-Rives (2004). Free energies of hydration from a generalized Born model and an ALL-atom force field. *Journal of Physical Chemistry B* 108 (41): 16264-16270.

Karra, J. R. and K. S. Walton (2008). Effect of Open Metal Sites on Adsorption of Polar and Nonpolar Molecules in Metal-Organic Framework Cu-BTC. *Langmuir* 24 (16): 8620-8626.

Kesanli, B., Y. Cui, M. R. Smith, E. W. Bittner, B. C. Bockrath and W. B. Lin (2005). Highly interpenetrated metal-organic frameworks for hydrogen storage. *Angewandte Chemie-International Edition* 44 (1): 72-75.

Kim, S., J. Ida, V. V. Guliants and J. Y. S. Lin (2005). Tailoring pore properties of MCM-48 silica for selective adsorption of CO_2. *Journal of Physical Chemistry B* 109 (13): 6287-6293.

Kitagawa, S., R. Kitaura and S. Noro (2004). Functional porous coordination polymers. *Angewandte Chemie-International Edition* 43 (18): 2334-2375.

Kitagawa, S., T. Okubo, S. Kawata, M. Kondo, M. Katada and H. Kobayashi (1995). An Oxalate-Linked Copper(II) Coordination Polymer, $[Cu_2(Oxalate)_2(Pyrazine)_3]_n$, Constructed with 2 Different Copper Units - X-Ray Crystallographic and Electronic-Structures. *Inorganic Chemistry* 34 (19): 4790-4796.

Kleitz, F., W. Schmidt and F. Schuth (2003). Calcination behavior of different surfactant-templated mesostructured silica materials. *Microporous and Mesoporous Materials* 65 (1): 1-29.

Knöfel, C., J. Descarpentries, A. Benzaouia, V. Zeleňák, S. Mornet, P. L. Llewellyn and V. Hornebecq (2007). Functionalised micro-/mesoporous silica for the adsorption of carbon dioxide. *Microporous and Mesoporous Materials* 99 (1-2): 79-85.

Knowles, G. P., J. V. Graham, S. W. Delaney and A. L. Chaffee (2005). Aminopropyl-functionalized mesoporous silicas as CO_2 adsorbents. *Fuel Processing Technology* 86 (14-15): 1435-1448.

Kresge, C. T., M. E. Leonowicz, W. J. Roth, J. C. Vartuli and J. S. Beck (1992). Ordered Mesoporous Molecular-Sieves Synthesized by a Liquid- Crystal Template Mechanism. *Nature* 359 (6397): 710-712.

Krungleviciute, V., K. Lask, L. Heroux, A. D. Migone, J. Y. Lee, J. Li and A. Skoulidas (2007). Argon adsorption on Cu_3(Benzene-1,3,5-tricarboxylate)$_2$(H_2O)$_3$ metal-organic framework. *Langmuir* 23 (6): 3106-3109.

Langmuir, I. (1916). The constitution and fundamental properties of solids and liquids. Part I. Solids. *Journal of the American Chemical Society* 38: 2221-2295.

Larson, R. G., L. E. Scriven and H. T. Davis (1985). Monte-Carlo Simulation of Model Amphiphilic Oil-Water Systems. *Journal of Chemical Physics* 83 (5): 2411-2420.

Lee, J., J. Li and J. Jagiello (2005). Gas sorption properties of microporous metal organic frameworks. *Journal Of Solid State Chemistry* 178 (8): 2527-2532.

Li, H., M. Eddaoudi, M. O'Keeffe and O. M. Yaghi (1999). Design and synthesis of an exceptionally stable and highly porous metal-organic framework. *Nature* 402 (6759): 276-279.

Liang, Z., B. Fadhel, C. J. Schneider and A. L. Chaffee (2008). Stepwise growth of melamine-based dendrimers into mesopores and their CO_2 adsorption properties. *Microporous and Mesoporous Materials* 111 (1-3): 536-543.

Liu, J. C., J. T. Culp, S. Natesakhawat, B. C. Bockrath, B. Zande, S. G. Sankar, G. Garberoglio and J. K. Johnson (2007a). Experimental and theoretical studies of gas adsorption in Cu_3(BTC)$_2$: An effective activation procedure. *Journal of Physical Chemistry C* 111 (26): 9305-9313.

Liu, Y., C. M. Brown, D. A. Neumann, V. K. Peterson and C. J. Kepert (2007b). Inelastic neutron scattering of H_2 adsorbed in HKUST-1. *Journal of Alloys and Compounds* 446: 385-388.

Loiseau, T., C. Serre, C. Huguenard, G. Fink, F. Taulelle, M. Henry, T. Bataille and G. Férey (2004). A rationale for the large breathing of the porous aluminum terephthalate (MIL-53) upon hydration. *Chemistry-a European Journal* 10 (6): 1373-1382.

Mackie, A. D., A. Z. Panagiotopoulos and I. Szleifer (1997). Aggregation behavior of a lattice model for amphiphiles. *Langmuir* 13 (19): 5022-5031.

Martín-Calvo, A., E. García-Pérez, J. M. Castillo and S. Calero (2008). Molecular simulations for adsorption and separation of natural gas in IRMOF-1 and Cu-BTC metal-organic frameworks. *Physical Chemistry Chemical Physics* 10 (47): 7085-7091.

Martin, M. G. and J. I. Siepmann (1998). Transferable potentials for phase equilibria. 1. United-atom description of n-alkanes. *Journal of Physical Chemistry B* 102 (14): 2569-2577.

Mayo, S.L.; Olafson, B.D.; Goddard, W.A. (1990) Dreiding - A Generic Force-Field for Molecular Simulations. *Journal of Physical Chemistry*, 94, 8897

Metropolis, N., A. W. Rosenbluth, M. N. Rosenbluth, A. H. Teller and E. Teller (1953). Equation of State Calculations by Fast Computing Machines. *Journal of Chemical Physics* 21 (6): 1087-1092.

Millward, A. R. and O. M. Yaghi (2005). Metal-organic frameworks with exceptionally high capacity for storage of carbon dioxide at room temperature. *Journal Of The American Chemical Society* 127 (51): 17998-17999.

Müller, U., M. Schubert, F. Teich, H. Pütter, K. Schierle-Arndt and J. Pastre (2006). Metal-organic frameworks - prospective industrial applications. *Journal of Materials Chemistry* 16 (7): 626-636.

Murthy, C. S., K. Singer, M. L. Klein and I. R. McDonald (1980). Pairwise Additive Effective Potentials for Nitrogen. *Molecular Physics* 41 (6): 1387-1399.

Myers, A. L. and P. A. Monson (2002). Adsorption in porous materials at high pressure: Theory and experiment. *Langmuir* 18 (26): 10261-10273.

Ni, Z. and R. I. Masel (2006). Rapid production of metal-organic frameworks via microwave-assisted solvothermal synthesis. *Journal of the American Chemical Society* 128 (38): 12394-12395.

Nicholson, D. and N. G. Parsonage (1982). *Computer Simulation and the Statistical Mechanics of Adsorption*, London, Academic Press.

Nicholson, T. M. and S. K. Bhatia (2007). Role of electrostatic effects in the pure component and binary adsorption of ethylene and ethane in Cu-tricarboxylate metal-organic frameworks. *Adsorption Science & Technology* 25 (8): 607-619.

NIST Chemistry Webbook (2005), Thermodynamik properties of fluid systems, NIST standard reference database 69, National Institute of Standards and Technology, Gaitersburg MD, 20899 (http://webbook.nist.gov).

Pan, L., M. B. Sander, X. Y. Huang, J. Li, M. Smith, E. Bittner, B. Bockrath and J. K. Johnson (2004). Microporous metal organic materials: Promising candidates as

sorbents for hydrogen storage. *Journal Of The American Chemical Society* 126 (5): 1308-1309.

Panella, B. and M. Hirscher (2005). Hydrogen physisorption in metal-organic porous crystals. *Advanced Materials* 17 (5): 538-541.

Panella, B., M. Hirscher, H. Pütter and U. Müller (2006). Hydrogen adsorption in metal-organic frameworks: Cu-MOFs and Zn-MOFs compared. *Advanced Functional Materials* 16 (4): 520-524.

Panella, B., K. Hones, U. Müller, N. Trukhan, M. Schubert, H. Pütter and M. Hirscher (2008). Desorption studies of hydrogen in metal-organic frameworks. *Angewandte Chemie-International Edition* 47 (11): 2138-2142.

Patti, A., A. D. Mackie and F. R. Siperstein (2006). *Studies in Surface Science and Catalysis* 160: 495.

Patti, A., A. D. Mackie and F. R. Siperstein (2007). Monte Carlo simulation of self-assembled ordered hybrid materials. *Langmuir* 23 (12): 6771-6780.

Potoff, J. J. and J. I. Siepmann (2001). Vapor-liquid equilibria of mixtures containing alkanes, carbon dioxide, and nitrogen. *Aiche Journal* 47 (7): 1676-1682.

Press, W. H., S. A. Teukolsky, W. T. Vetterling and B. P. Flannery (1992). *Numerical Recipes*, New York, Cambridge University Press.

Prosenjak, C., A. Patti, F. R. Siperstein and N. A. Seaton (2007). Modelling the synthesis of periodic mesoporous silicas. *Studies in Surface Science and Catalysis* 170B: 1652-1659.

Rao, N. Z. and L. D. Gelb (2004). Molecular dynamics simulations of the polymerization of aqueous silicic acid and analysis of the effects of concentration on silica polymorph distributions, growth mechanisms, and reaction kinetics. *Journal of Physical Chemistry B* 108 (33): 12418-12428.

Rappe, A.K., Casewit, C.J., Colwell, K.S., Goddard, W.A., Skiff, W.M. (1992) UFF, a Full Periodic Table Force Field for Molecular mechanics and Molecular Dynamics Simulations. *Journal of the American Chemical Society*, 1992, 114, 10024

Reynhardt, J. P. K., Y. Yang, A. Sayari and H. Alper (2004). Periodic mesoporous silica-supported recyclable rhodium-complexed dendrimer catalysts. *Chemistry of Materials* 16 (21): 4095-4102.

Reynhardt, J. P. K., Y. Yang, A. Sayari and H. Alper (2005). Polyamidoamine dendrimers prepared inside the channels of pore-expanded periodic mesoporous silica. *Advanced Functional Materials* 15 (10): 1641-1646.

Rizzo, R. C. and W. L. Jorgensen (1999). OPLS all-atom model for amines: Resolution of the amine hydration problem. *Journal of the American Chemical Society* 121 (20): 4827-4836.

Rosi, N. L., J. Eckert, M. Eddaoudi, D. T. Vodak, J. Kim, M. O'Keeffe and O. M. Yaghi (2003). Hydrogen storage in microporous metal-organic frameworks. *Science* 300 (5622): 1127-1129.

Rouquerol, J., P. Llewellyn and F. Rouquerol (2007). *Studies in Surface Science and Catalysis* 160: 49-56.

Rowsell, J. L. C., A. R. Millward, K. S. Park and O. M. Yaghi (2004). Hydrogen sorption in functionalized metal-organic frameworks. *Journal Of The American Chemical Society* 126 (18): 5666-5667.

Rowsell, J. L. C. and O. M. Yaghi (2004). Metal-organic frameworks: a new class of porous materials. *Microporous and Mesoporous Materials* 73 (1-2): 3-14.

Rowsell, J. L. C. and O. M. Yaghi (2005). Strategies for hydrogen storage in metal-organic frameworks. *Angewandte Chemie-International Edition* 44 (30): 4670-4679.

Sandler, S. I. (1999). *Chemical and Engineering Thermodynamics*, Third Edition, John Wiley & Sons, New York.

Schumacher, C. (2006). Design of Hybrid Organic/Inorganic Adsorbents for Gas Separation, The University of Edinburgh. PhD Thesis.

Schumacher, C., J. Gonzalez, M. Perez-Mendoza, P. A. Wright and N. A. Seaton (2006a). Design of hybrid organic/inorganic adsorbents based on periodic mesoporous silica. *Industrial & Engineering Chemistry Research* 45 (16): 5586-5597.

Schumacher, C., J. Gonzalez, P. A. Wright and N. A. Seaton (2006b). Generation of atomistic models of periodic mesoporous silica by kinetic Monte Carlo simulation of the synthesis of the material. *Journal Of Physical Chemistry B* 110 (1): 319-333.

Schumacher, C. and N. A. Seaton (2005). Modeling of organically functionalized mesoporous silicas for the design of adsorbents. *Adsorption-Journal Of The International Adsorption Society* 11: 643-648.

Selvam, P., S. K. Bhatia and C. G. Sonwane (2001). Recent advances in processing and characterization of periodic mesoporous MCM-41 silicate molecular sieves. *Industrial & Engineering Chemistry Research* 40 (15): 3237-3261.

Senkovska, I. and S. Kaskel (2008). High pressure methane adsorption in the metal-organic frameworks $Cu_3(btc)_2$, $Zn_2(bdc)_2dabco$, and $Cr_3F(H_2O)_2O(bdc)_3$. *Microporous and Mesoporous Materials* 112 (1-3): 108-115.

Serna-Guerrero, R., E. Da'na and A. Sayari (2008). New Insights into the Interactions of CO_2 with Amine-Functionalized Silica. *Industrial & Engineering Chemistry Research* 47 (23): 9406-9412.

Serre, C., F. Millange, C. Thouvenot, M. Nogues, G. Marsolier, D. Louer and G. Férey (2002). Very large breathing effect in the first nanoporous chromium(III)-based solids: MIL-53 or Cr-III(OH)·$\{O_2C\text{-}C_6H_4\text{-}CO_2\}$·$\{HO_2C\text{-}C_6H_4\text{-}CO_2H\}_x$·$H_2O_y$. *Journal of the American Chemical Society* 124 (45): 13519-13526.

Sese, L. M. (1995). Feynman-Hibbs Potentials and Path-Integrals for Quantum Lennard-Jones Systems - Theory and Monte-Carlo Simulations. *Molecular Physics* 85 (5): 931-947.

Shen, D. M., M. Bulow, F. Siperstein, M. Engelhard and A. L. Myers (2000). Comparison of experimental techniques for measuring isosteric heat of adsorption. *Adsorption-Journal of the International Adsorption Society* 6 (4): 275-286.

Siperstein, F. R. and K. E. Gubbins (2003). Phase separation and liquid crystal self-assembly in surfactant-inorganic-solvent systems. *Langmuir* 19 (6): 2049-2057.

Skoulidas, A. I. (2004). Molecular dynamics simulations of gas diffusion in metal-organic frameworks: Argon in CuBTC. *Journal of the American Chemical Society* 126 (5): 1356-1357.

Sonwane, C. G., C. W. Jones and P. J. Ludovice (2005). A model for the structure of MCM-41 incorporating surface roughness. *Journal of Physical Chemistry B* 109 (49): 23395-23404.

Stubbs, J. M., B. Chen, J. J. Potoff and J. J. Siepmann (2001). Monte Carlo calculations for the phase equilibria of alkanes, alcohols, water, and their mixtures. *Fluid Phase Equilibria* 183: 301-309.

Talu, O. and A. L. Myers (2001). Molecular simulation of adsorption: Gibbs dividing surface and comparison with experiment. *Aiche Journal* 47 (5): 1160-1168.

Tao, J. M.; Perdew, J. P.; Staroverov, V. N.; Scuseria, G. E. (2003) Climbing the density functional ladder: nonempirical meta-generalized gradient approximation designed for molecules and solids. *Physical Review Letters* 91, (14) 146401.

Tu, Y. and J. Tersoff (2000). Structure and energetics of the Si-SiO_2 interface. *Physical Review Letters* 84 (19): 4393-4396.

Vajo, J. J., S. L. Skeith and F. Mertens (2005). Reversible storage of hydrogen in destabilized LiBH4. *Journal of Physical Chemistry B* 109 (9): 3719-3722.

Vishnyakov, A., P. I. Ravikovitch, A. V. Neimark, M. Bulow and Q. M. Wang (2003). Nanopore structure and sorption properties of Cu-BTC metal- organic framework. *Nano Letters* 3 (6): 713-718.

Vitillo, J. G., L. Regli, S. Chavan, G. Ricchiardi, G. Spoto, P. D. C. Dietzel, S. Bordiga and A. Zecchina (2008). Role of exposed metal sites in hydrogen storage in MOFs. *J Am Chem Soc* 130 (26): 8386-96.

Vitillo, J. G., G. Ricchiardi, G. Spoto and A. Zecchina (2005). Theoretical maximal storage of hydrogen in zeolitic frameworks. *Physical Chemistry Chemical Physics* 7 (23): 3948-3954.

Vlugt, T. J. H., M. G. Martin, B. Smit, J. I. Siepmann and R. Krishna (1998). Improving the efficiency of the configurational-bias Monte Carlo algorithm. *Molecular Physics* 94 (4): 727-733.

Vuong, T. and P. A. Monson (1996). Monte Carlo simulation studies of heats of adsorption in heterogeneous solids. *Langmuir* 12 (22): 5425-5432.

Wang, Q. M., D. M. Shen, M. Bulow, M. L. Lau, S. G. Deng, F. R. Fitch, N. O. Lemcoff and J. Semanscin (2002). Metallo-organic molecular sieve for gas separation and purification. *Microporous and Mesoporous Materials* 55 (2): 217-230.

Wang, S. Y., Q. Y. Yang and C. L. Zhong (2008). Adsorption and separation of binary mixtures in a metal-organic framework Cu-BTC: A computational study. *Separation and Purification Technology* 60 (1): 30-35.

Wong-Foy, A. G., A. J. Matzger and O. M. Yaghi (2006). Exceptional H_2 saturation uptake in microporous metal-organic frameworks. *Journal of the American Chemical Society* 128 (11): 3494-3495.

Wu, C. G. and T. Bein (1996). Microwave synthesis of molecular sieve MCM-41. *Chemical Communications* (8): 925-926.

Xiao, B., P. S. Wheatley, X. B. Zhao, A. J. Fletcher, S. Fox, A. G. Rossi, I. L. Megson, S. Bordiga, L. Regli, K. M. Thomas and R. E. Morris (2007). High-capacity hydrogen and nitric oxide adsorption and storage in a metal-organic framework. *Journal of the American Chemical Society* 129 (5): 1203-1209.

Xu, X. C., C. S. Song, J. M. Andresen, B. G. Miller and A. W. Scaroni (2002). Novel polyethylenimine-modified mesoporous molecular sieve of MCM-41 type as high-capacity adsorbent for CO_2 capture. *Energy & Fuels* 16 (6): 1463-1469.

Xu, X. C., C. S. Song, J. M. Andresen, B. G. Miller and A. W. Scaroni (2003). Preparation and characterization of novel CO_2 "molecular basket" adsorbents based on polymer-modified mesoporous molecular sieve MCM-41. *Microporous and Mesoporous Materials* 62 (1-2): 29-45.

Xu, X. C., C. S. Song, B. G. Miller and A. W. Scaroni (2005). Influence of moisture on CO_2 separation from gas mixture by a nanoporous adsorbent based on polyethylenimine-modified molecular sieve MCM-41. *Industrial & Engineering Chemistry Research* 44 (21): 8113-8119.

Yanagisawa, T., T. Shimizu, K. Kuroda and C. Kato (1990). The Preparation of Alkyltrimethylammonium-Kanemite Complexes and Their Conversion to Microporous Materials. *Bulletin of the Chemical Society of Japan* 63 (4): 988-992.

Yang, Q. Y., C. Y. Xue, C. L. Zhong and J. F. Chen (2007). Molecular simulation of separation of CO2 from flue gases in Cu-BTC metal-organic framework. *Aiche Journal* 53 (11): 2832-2840.

Yang, Q. Y. and C. L. Zhong (2006a). Electrostatic-field-induced enhancement of gas mixture separation in metal-organic frameworks: A computational study. *Chemphyschem* 7 (7): 1417-1421.

Yang, Q. Y. and C. L. Zhong (2006b). Molecular simulation of carbon dioxide/methane/hydrogen mixture adsorption in metal-organic frameworks. *Journal of Physical Chemistry B* 110 (36): 17776-17783.

Yang, Q. Y. and C. L. Zhong (2006c). Understanding hydrogen adsorption in metal-organic frameworks with open metal sites: A computational study. *Journal of Physical Chemistry B* 110 (2): 655-658.

Yun, J. H., T. Düren, F. J. Keil and N. A. Seaton (2002). Adsorption of methane, ethane, and their binary mixtures on MCM-41: Experimental evaluation of methods for the prediction of adsorption equilibrium. *Langmuir* 18 (7): 2693-2701.

Zhao, D. Y., J. L. Feng, Q. S. Huo, N. Melosh, G. H. Fredrickson, B. F. Chmelka and G. D. Stucky (1998). Triblock copolymer syntheses of mesoporous silica with periodic 50 to 300 angstrom pores. *Science* 279 (5350): 548-552.

Zheng, F., D. N. Tran, B. J. Busche, G. E. Fryxell, R. S. Addleman, T. S. Zemanian and C. L. Aardahl (2005). Ethylenediamine-modified SBA-15 as regenerable CO_2 sorbent. *Industrial & Engineering Chemistry Research* 44 (9): 3099-3105.

B Acronyms

BET	Brunnauer-Emmet-Teller
CBMC	Computational biased Monte Carlo
CSD	Cambridge Structural Database
CuBTC	Copper Benzene TriCarboxylate
DEA	Diethanol amine
DOE	Department of Energy (United States)
eMC	equilibrium Monte Carlo
FH	Feynman-Hibbs
GCMC	Grand Canonical Monte Carlo
HKUST-1	Hong Kong University of Science and Technology - 1
IRMOF	Isoreticular metal organic framework
IUPAC	International Union of Pure and Applied Chemistry
LJ	Lennard-Jones
kMC	kinetic Monte Carlo
MC	Monte Carlo
MCM-41	Mobil Composition of Matter 41
MD	Molecular dynamics
MDEA	Methyl diethanol amine
MEA	Monoethanol amine
MIL	Material Institute Lavoisier
MOF	Metal-organic framework
MSU	Michigan State University
MUSIC	Multipurpose Simulation Code
OPLS	Optimized potential for Liquid Simulations
PEI	Polyethyleneimine
PFP-MCM-41	pentafluorophenyl MCM-41
PR-EOS	Peng-Robinson equation of state
SBA	Santa Barbara
STP	Standard Temperature and Pressure
TEOS	Tetraethyl orthosilicate
TraPPE	Transferable Potential for Phase Equilibria
uc	unit cell
UFF	Universal Force Field
WAXS	wide angle X-ray scattering
XRD	X-ray diffraction

C Nomenclature

Roman letters

c	BET constant
D	desorption rate
E	energy
E_k	energy of microstate k
f	fugacity
h	Planck's constant
$\hbar$	reduced Planck's constant, h/(2π)
$h^{b,r}$	residual enthalpy of the bulk phase
k	lattice vector denoting image boxes in Fourier space
K	force constants (bond stretching, bending and torsion)
k_B	Boltzmann's constant
l	lattice vector denoting image boxes in real space
l_x, l_y, l_z	elements of vector **l**
L	unit cell length
m	mass of a molecule
M	macroscopic property
M_k	property M in microstate k
$\langle M \rangle_{\text{ensemble}}$	ensemble average for macroscopic property M
n	new configuration
N	number of molecules
N_{abs}	absolute number of molecules adsorbed
N_{Av}	Avogadro's number
N_{ex}	excess number of molecules adsorbed
N_i	number of molecules of species i
N_T	number of molecules adsorbed at temperature T
o	old configuration
P	pressure
P	probability
P_k	probability of microstate k
P_{acc}	acceptance probability
P_{gen}	a priori probability
P_0	saturation pressure
q	point charge
q_d	differential heat of adsorption
r	position
r	position (vector)
r_{ij}	distance between interaction sites i and j
$r_{ij,0}$	equilibrium distance between the sites i and j
$r_{i,0}$	equilibrium bond length for bond i
r_{min}	radius for the minimum energy well
R	universal gas constant
r_c	cut-off radius
s	generalised coordinate (vector)
S	selectivity
T	temperature
T*	dimensionless temperature
u_{ij}	potential between two interaction sites i and j

U	potential energy (indices indicate a specific interaction)
V	volume
V_{ads}	volume adsorbed
V_{dead}	dead volume in the experiment
V_m	monolayer capacity
V_{res}	volume of the reservoir in the experiment
x_i	mole fraction of component *i* in the adsorbed phase
y_i	mole fraction of component *i* in the bulk phase
Z	quantum partition function

Greek letters

Λ	de Broglie wave length
Ξ	partition function of the grand canonical ensemble
α	convergence parameter in Ewald summation
β	$(k_B T)^{-1}$
ε	potential well depth
ε_{ij}	potential well depth for sites *i* and *j*
θ	angle (bending)
$\theta_{ijk,0}$	equilibrium angle for the sites *i*, *j* and *k*
$\theta_{a,0}$	equilibrium angle for the atom a
μ	chemical potential
μ	reduced mass
ρ	probability distribution in the classical description
ρ_g	gas density
σ	Lennard-Jones diameter
ϕ	angle (torsion)
ω_{ij}	global interchange energy between sites *i* and *j*

D The Peng - Robinson equation of state

The Peng-Robinson equation of state (Sandler (1999)) was used:

$$P = \frac{RT}{v-b} - \frac{a(T)}{v^2 + 2bv - b^2} \tag{D.1}$$

with the mixing rules

$$a = \sum_i^n \sum_j^n y_i y_j a_{ij} \tag{D.2}$$

and

$$b = \sum_i^n y_i b_i \tag{D.3}$$

and the combining rule

$$a_{ij} = \sqrt{a_{ii} a_{jj}}(1 - k_{ij}) \tag{D.4}$$

The parameters a and b for the pure components are calculated as

$$a_{ii} = \frac{0.45724 R^2 T_{c,i}^2}{P_{c,i}} \left(1 + \left(0.37464 + 1.54226\omega_i - 0.26992\omega_i^2\right)\left(1 - \sqrt{\frac{T}{T_{c,i}}}\right)\right)^2 \tag{D.5}$$

and

$$b_i = \frac{0.0778 R T_{c,i}}{P_{c,i}}. \tag{D.6}$$

The critical data is given in Table D-1 and the binary interaction parameters in Table D-2.

Table D-1 Critical temperature, critical pressure and accentric factor used in the Peng-Robinson equation of state. Data taken from NIST Chemistry Webbook (2005).

Fluid	T_c (K)	P_c (bar)	ω (-)
He	5.1953	2.2746	-0.382
CH_4	190.564	45.992	0.01142
C_2H_6	305.33	48.718	0.0993
C_3H_8	369.825	42.4766	0.1524
CO_2	304.1282	73.773	0.22394
N_2	126.192	33.958	0.0372

Table D-2 Binary interaction parameters used in the Peng-Robinson equation of state. Data taken from Sandler (1999).

	CH_4	C_2H_6	CO_2
CH_4		-0.003	0.09
C_2H_6	-0.003		0.13
CO_2	0.09	0.13	

As for all cubic equations of state, the Peng-Robinson EOS gives only an approximation of the real behaviour. Generally, they provide a reasonable description for hydrocarbons. For many other fluids it only works well for the vapour region. In the simulations, where the PREOS is used to calculate the fugacity, care must be taken that the pressure does not exceed the vapour pressure of the fluid.

E Parameters for organic surface groups

Table E-1 Lennard-Jones interaction parameters and point charges for surface groups

group	site	ε/k_B (K)	σ (nm)	q_i (e_0)	ref.
silanol	O	185.0	0.3000	-0.533	Brodka and Zerda (1996)
	H			0.206	Brodka and Zerda (1996)
					Yun *et al.* (2002)
monofluorophenyl	C	55.86	0.3750	-0.120	Schumacher *et al.* (2006a)
	CH	55.38	0.3750	-0.100	Jorgensen *et al.* (1984)
	CH	55.38	0.3750	0	Jorgensen *et al.* (1984)
	C	35.24	0.3550	0.220	Jorgensen *et al.* (2004)
	CH	55.38	0.3750	0	Jorgensen *et al.* (1984)
	CH	55.38	0.3750	-0.100	Jorgensen *et al.* (1984)
	F	30.71	0.285	-0.220	Jorgensen *et al.* (2004)
monoiodophenyl	C	55.86	0.3750	-0.120	Schumacher *et al.* (2006a)
	CH	55.38	0.3750	-0.100	Jorgensen *et al.* (1984)
	CH	55.38	0.3750	0	Jorgensen *et al.* (1984)
	C	35.24	0.3550	0.100	Jorgensen *et al.* (2004)
	CH	55.38	0.3750	0	Jorgensen *et al.* (1984)
	CH	55.38	0.3750	-0.100	Jorgensen *et al.* (1984)
	I	302.08	0.3750	-0.100	Jorgensen *et al.* (2004)
difluorophenyl	C	55.86	0.3750	-0.120	Schumacher *et al.* (2006a)
	CH	55.38	0.3750	-0.100	Jorgensen *et al.* (1984)
	C	35.24	0.3550	0.200	Jorgensen *et al.* (2004)
	CH	55.38	0.3750	0	Jorgensen *et al.* (1984)
	C	35.24	0.3550	0.200	Jorgensen *et al.* (2004)
	CH	55.38	0.3750	-0.100	Jorgensen *et al.* (1984)
	F	30.71	0.285	-0.200	Jorgensen *et al.* (2004)
pentafluorophenyl	C	55.86	0.3750	-0.120	Schumacher *et al.* (2006a)
	C	35.24	0.3550	0.03	Jorgensen *et al.* (2004)
	C	35.24	0.3550	0.13	Jorgensen *et al.* (2004)
	C	35.24	0.3550	0.13	Jorgensen *et al.* (2004)
	C	35.24	0.3550	0.13	Jorgensen *et al.* (2004)
	C	35.24	0.3550	0.03	Jorgensen *et al.* (2004)
	F	30.71	0.2850	-0.130	Jorgensen *et al.* (2004)
aminoethyl-aminopropyl	CH_2	59.409	0.3905	-0.32	Schumacher *et al.* (2006a)
	CH_2	59.409	0.3905	0	Schumacher *et al.* (2006a)
	CH_2	59.409	0.3905	0.2	Schumacher *et al.* (2006a)
	N	85.589	0.33	-0.780	Rizzo and Jorgensen (1999)
	H			0.380	Rizzo and Jorgensen (1999)
	CH_2	59.409	0.3905	0.2	Schumacher *et al.* (2006a)
	CH_2	59.409	0.3905	0.18	Schumacher *et al.* (2006a)
	N	85.589	0.33	-0.9	Rizzo and Jorgensen (1999)
	H			0.36	Rizzo and Jorgensen (1999)
diaminophenyl	C	55.86	0.3750	-0.120	Schumacher *et al.* (2006a)
	CH	55.38	0.3750	-0.100	Jorgensen *et al.* (1984)
	C	35.24	0.3550	0.180	Rizzo and Jorgensen (1999)
	CH	55.38	0.3750	0	Jorgensen *et al.* (1984)
	C	35.24	0.3550	0.180	Rizzo and Jorgensen (1999)
	CH	55.38	0.3750	-0.100	Jorgensen *et al.* (1984)
	N	85.589	0.33	-0.90	Rizzo and Jorgensen (1999)
	H			0.36	Rizzo and Jorgensen (1999)

Table E-2 Bond length for covalent bonds in surface groups.

group	bond	l (nm)	K/k_B (K/pm^2) [a]	ref.
silanol	Si-O	0.16		Tu and Tersoff (2000)
	O-H	0.0945		Stubbs *et al.* (2001)
modified phenyl surface groups	Si-C	0.1865		Frierson *et al.* (1988)
	C-C	0.14		Jorgensen *et al.* (1984)
	C-N	0.134		Rizzo and Jorgensen (1999)
	N-H	0.1010		Rizzo and Jorgensen (1999)
	C-F	0.1354		Jorgensen (2007)
	C-Cl	0.1725		Jorgensen (2007)
	C-Br	0.187		Jorgensen (2007)
	C-I	0.208		Jorgensen (2007)
aminoethyl-aminopropyl	Si-CH_2	0.188		Frierson *et al.* (1988)
	CH_2-CH_2	0.153	15.607	Jorgensen *et al.* (1984)
	CH_2-N	0.1448	19.283	Rizzo and Jorgensen (1999)
	N-H	0.1010		Rizzo and Jorgensen (1999)

[a] Bond lengths with no *K* value are fixed.

Table E-3 Bond angles and bending constants for bonds in surface groups.

group	bonds	angle (deg)	K/k_B (K/deg^2) [a]	ref.
silanol	Si-O-H	108.5		Stubbs *et al.* (2001)
modified phenyl surface groups	O-Si-C	0.0		Schumacher *et al.* (2006a)
	Si-C-C	120		Schumacher *et al.* (2006a)
	C-C-C	120		Jorgensen *et al.* (1984)
	C-C-F	120		
	C-C-I	120		
	C-C-N	120		Schumacher *et al.* (2006a)
	C-N-H	109.5		Rizzo and Jorgensen (1999)
	H-N-H	106.4		Rizzo and Jorgensen (1999)
aminoethyl-aminopropyl	O-Si-CH_2	0.0		Schumacher *et al.* (2006a)
	Si-CH_2-CH_2	112	9.519	Stubbs *et al.* (2001)
	CH_2-CH_2-CH_2	112	9.519	Stubbs *et al.* (2001)
	CH_2-CH_2-N	109.47	8.619	Rizzo and Jorgensen (1999)
	CH_2-N-CH_2	107.2	7.944	Rizzo and Jorgensen (1999)
	N-CH_2-CH_2	109.47	8.619	Rizzo and Jorgensen (1999)
	CH_2-CH_2-N	109.47	8.619	Rizzo and Jorgensen (1999)
	CH_2-N-H	109.5		Rizzo and Jorgensen (1999)
	H-N-H	106.4		Rizzo and Jorgensen (1999)

[a] Bond angles with no K value are fixed.

Table E-4 Torsional parameters for surface groups

group	dihedral angle	V_0 (K)	V_1 (K)	V_2 (K)	V_3 (K)	ref.
silanol	O-Si-O-H	0	0	0	0	*a)*
phenylbased surface groups	O-Si-CH-CH	0	0	0	0	*a)*
	C_2C-NH_2	1963.4	0	-1963.4	0	*a)*
aminoethyl-aminopropyl	O_3Si-CH_2-CH_2	0	0	0	0	*a)*
	Si-CH_2-CH_2-CH_2	0	710.4	-136.4	1583.4	*b)*
	CH_2-CH_2-CH_2-NH	0	1204.3	-339.3	276.9	*c)*
	CH_2-CH_2-NH-CH_2	0	209.4	-64.4	349.9	*c)*
	CH_2-NH-CH_2-CH_2	0	209.4	-64.4	349.9	*c)*
	NH-CH_2-CH_2-NH_2	0	0	0	0	

a) Schumacher *et al.* (2006a), *b)* Jorgensen *et al.* (1984), *c)* Rizzo and Jorgensen (1999)